AIR BREAKDOWN IN CONTACT ELECTRIFICATION

by

Hongcheng Tao

A Dissertation

Submitted to the Faculty of Purdue University

In Partial Fulfillment of the Requirements for the Degree of

Doctor of Philosophy

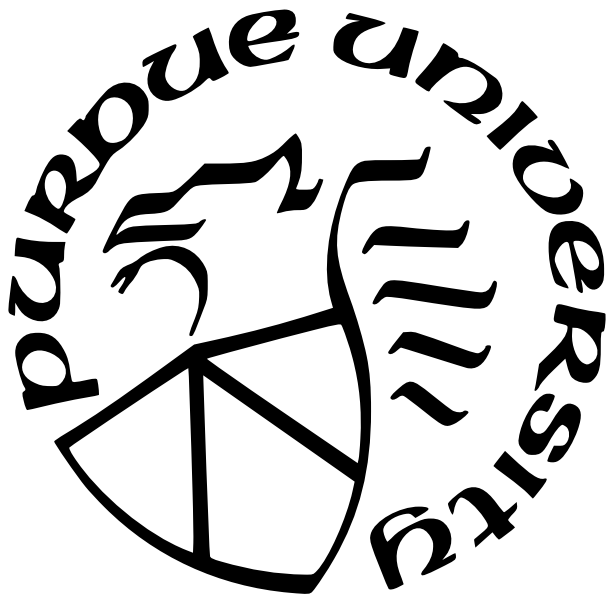

School of Mechanical Engineering

West Lafayette, Indiana

May 2022

THE PURDUE UNIVERSITY GRADUATE SCHOOL
STATEMENT OF COMMITTEE APPROVAL

Dr. James Gibert, Chair

School of Mechanical Engineering

Dr. Chelsea Davis

School of Materials Engineering

Dr. Arvind Raman

School of Mechanical Engineering

Dr. Jeffrey Rhoads

School of Mechanical Engineering

Approved by:

Dr. Nicole Key

TABLE OF CONTENTS

LIST OF FIGURES

ABBREVIATIONS

PDMS	polydimethylsiloxane
PTFE	polytetrafluoroethylene
PMMA	polymethyl methacrylate
PLA	polylactic acid
TPU	thermoplastic polyurethane
ABS	acrylonitrile butadiene styrene
SEM	scanning electron microscope
EDS	energy-dispersive X-ray spectroscopy

ABSTRACT

Contact electrification of solids in a gas medium involves two stages, i.e., surface charge deposition immediately at separation, and dissipation due to dielectric breakdown of the medium as the gap increases. The presumption that such gas breakdown obeys Paschen's law, which is conventionally determined for gas between electrodes with constant charge supply, is widely accepted yet unverified. The present work experimentally validates such dependence of the breakdown voltage of air between charged dielectric surfaces on both its pressure and the gap distance. Sample surfaces are brought to cycles of contact electrification in a vacuum chamber and charge relaxation due to air breakdown is monitored with measurements of the Coulomb attraction by fixing either the air pressure or gap distance and varying the other. The results indicate thresholds of pressure and distance to facilitate investigations of the raw amount of charge transfer prior to any breakdown discharge, which is adopted to examine the saturation trend of surface charge density in the contact electrification of multiple material combinations using the same test apparatus. Comparatively consistent results are obtained in repeated tests for a variety of contact pairs, while a reduction of saturated surface charge density is observed for PTFE against PDMS after breakdown discharge in low-pressure air, which is preliminarily attributed to alternations of PTFE surfaces caused by accelerated cation strikes during air breakdown, based on SEM images and estimations of particle energy in Townsend avalanches. Conclusions on both the general raw level of surface charge density and the air breakdown during separation in contact electrification are applied to complement models of vibro-impact triboelectric energy harvesters for predicting their performance under various air pressures and physical dimensions in order to either prevent or exploit air breakdown to enhance the power output.

1. INTRODUCTION

Contact electrification (triboelectricity), the phenomenon where electric charge is transferred between two dissimilar surfaces in mechanical contact, is known to exhibit highly unpredictable behaviors [1], [2]. The amount of post-contact surface charge is not only dependent on the material combination but also on conditions of the surface, the contact and the medium in between, as a result of which sophisticated efforts are needed to unify test standards for the characterization of triboelectric materials. These factors affect different phases, i.e., contact and separation, of a complete contact electrification cycle. In the contact stage a raw amount of surface charge is deposited which is influenced by factors such as surface topography and contact pressure which act either directly on the charging mechanism or on the effective contact area. Meanwhile, it is generally accepted that normal contact is sufficient for the initialization of electrification while friction/rubbing mainly serves to enhance the effective contact area as well and is thus not required. In the separation stage of a contact electrification cycle, the electric field generated by the raw charge density is often strong enough to trigger the dielectric breakdown of the gas or fluid medium that fills in the clearance. This partially neutralizes the accumulated surface charge to a breakdown limit dependent on the final gap distance as well as properties of the medium [3]–[5]. Knowledge of the medium breakdown process is therefore required if the original surface charge density before the breakdown loss is to be revealed for analysis of more fundamental contact electrification mechanisms. While gas breakdown between electrodes with an applied potential is known to be governed by Paschen's Law [6], [7], an experimental generalization to that between electrified dielectric surfaces is to be verified. This is approached in Chapter 2 which discusses potential distinctions between the breakdown discharge of surfaces with finite charge and that of electrodes with constant charge supply, as well as illustrating and justifying a test strategy that captures the voltage, using measurements of Coulomb force, across the gap between charged dielectric surfaces at incidents of air breakdown to reconstruct the Paschen curve. Instead of pursuing an extraordinarily high vacuum level, the test results provide the estimation of an adequate combination of air pressure and gap distance that guarantees the elimination of air breakdown, which is typically the priority

for a standardized examination of the charging process in the contact stage. This is applied in Chapter 3 to reveal the raw amount of post-contact charge transfer for several material combinations and to further extract observations on other aspects of contact electrification, both toward the goal of establishing a quantitative triboelectric series which not only ranks the relative polarity of materials (Figure 1.1), but also predicts the amount of charge transfer for any pair of materials under fixed conditions.

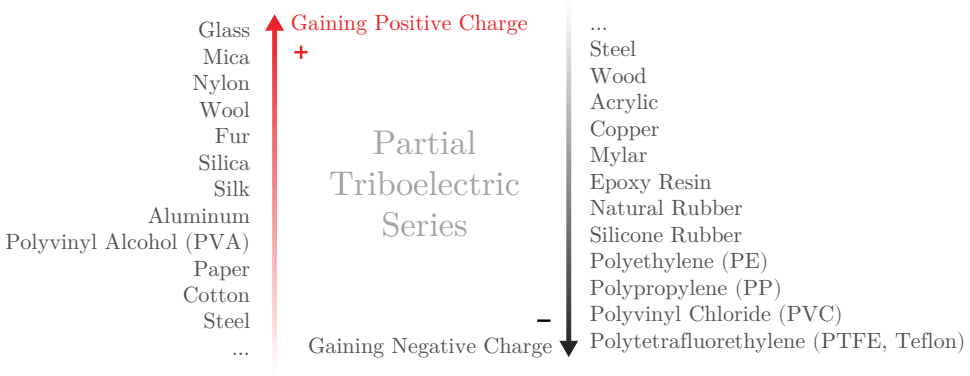

Figure 1.1. A partial qualitative triboelectric series.

The investigations on the Paschen's law in contact electrification of general materials as well as the quantification of surface charge saturation introduced in Chapters 2 and 3, respectively, can benefit research on the charge accumulation in spacecrafts [8], [9] which is known as a nontrivial hazard. Moreover, observations of breakdown-induced surface degradation, as will be discussed in Chapter 3, may help with predicting and preventing similar surface damage of any device or structure in space. In addition, the results see direct application in the recent development of vibro-impact triboelectric energy harvesters, which is discussed in Chapter 4 with an introduction of theories on vibro-impact energy harvesting and the advantages of employing triboelectricity as the electromechanical coupling mechanism, where the inclusion of air breakdown models is shown to improve the prediction of their performance as well as revealing potential exploitation of breakdown-induced voltage impulses for enhanced power output.

2. PASCHEN'S LAW IN CONTACT ELECTRIFICATION

Air breakdown during dielectric contact electrification is investigated. The conventional Paschen's law and its interpretations are introduced in Section 2.1, which is applied in Section 2.2 to predict behaviors of surface charge loss during the separation stage of a contact electrification cycle. The theory is preliminarily examined in atmospheric air in Section 2.3 and then verified in Section 2.4.

2.1 Conventional Determination of Paschen's Law

Gas breakdown is conventionally examined using parallel plate electrodes within, as shown in Figure 2.1a. An increasing voltage is applied across the electrodes until a significant continuous current is monitored, at which the voltage is recorded as the breakdown threshold V_b. Paschen's law summarizes the relation between V_b and the product of gap distance d and gas pressure p as

$$V_\mathrm{b} = \frac{B_\mathrm{g} pd}{\ln\left(A_\mathrm{g} pd\right) - \ln\left[\ln\left(1+\gamma_\mathrm{se}^{-1}\right)\right]} \tag{2.1}$$

where coefficients A_g and B_g depend only on the type of gas while γ_se, the secondary-electron-emission coefficient, is also related to the surface material and explained as follows. A common interpretation of Paschen's law assumes a breakdown mechanism initialized by free electrons in the gas medium, typically those freed from the electrodes by background radiation (cosmic rays). The electric field generated by the external voltage accelerates electrons that escape from the cathode toward the anode, where a saturation current (Figure 2.1b) can be measured when the voltage is increased to a level such that all electrons released from the cathode by background radiation are collected at the anode. As the voltage continues to increase, it may accelerate an electron to such kinetic energy that it has a chance to ionize a gas molecule when they collide, releasing another electron along with a cation. The cation is accelerated toward the cathode while the two electrons are accelerated toward the anode, therefore ionizing further gas molecules. This process repeats to produce a cascade of doubling in the number of free electrons, forming a Townsend avalanche [10],

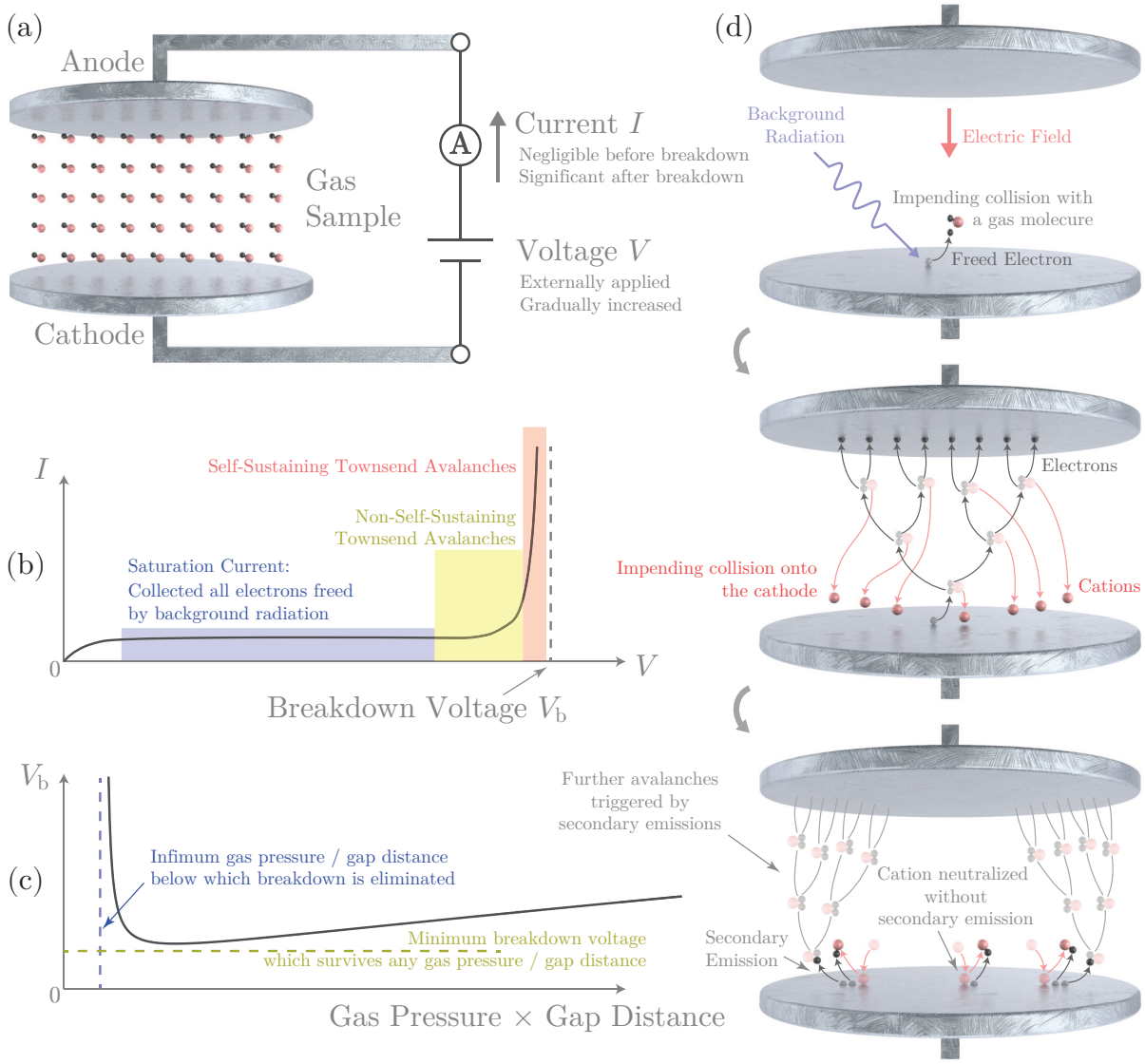

Figure 2.1. Conventional determination and interpretation of Paschen's law: a) Test setup with electrodes submerged in the examined gas. b) General relation between cross-gap current and voltage applied for a fixed combination of gap distance and gas pressure, with indication of the corresponding breakdown voltage. c) General form of Paschen's law for a fixed combination of type of gas and electrode materials: the relation between breakdown voltage and the product of gap distance and gas pressure. d) Interpretation of the breakdown voltage as what sustains cascades of Townsend avalanches from secondary emissions following the initialization by background radiation.

[11] and amplifying the saturation current. A higher voltage raises the chance of impact ionizations and thus the current, which yet is still limited by the initial amount of photoelectric current. It is further assumed that when a cation reaches the cathode and becomes neutralized, it has a chance to free another electron and form another Townsend avalanche. The probability of such secondary electron emission is represented by γ_{se} in Paschen's law 2.1. Breakdown of the gas medium is defined as when a surge of current is observed when the voltage is so high that the number of cations formed by the avalanche of a single free electron is large enough to guarantee the generation of at least one further avalanche, known as a self-sustaining discharge. This mechanism explains the dependence of such breakdown voltage V_{b} on the gas pressure and gap distance in that a higher pressure supplies more molecules for impact ionization (and thus cations for secondary emissions) but less distance (mean free path) between adjacent molecules for electrons to accelerate, while a wider gap also provides more molecules but results in a weaker electric field for the same voltage. The Paschen curve therefore exhibits both a minimum breakdown voltage $V_{\mathrm{inf}} = \dfrac{\mathrm{e}B_{\mathrm{g}}}{A_{\mathrm{g}}} \ln\left(1 + \gamma_{\mathrm{se}}^{-1}\right)$ (e being Euler's number) reachable at a certain pressure-distance combination $pd = \dfrac{\mathrm{e}}{A_{\mathrm{g}}} \ln\left(1 + \gamma_{\mathrm{se}}^{-1}\right)$ and a minimum pressure-distance product $(pd)_{\mathrm{inf}} = \dfrac{1}{A_{\mathrm{g}}} \ln\left(1 + \gamma_{\mathrm{se}}^{-1}\right)$, below which breakdown of the gas is theoretically prohibited (Figure 2.1c).

2.2 Gas Breakdown in Contact Electrification

Direct application of the conventional Paschen's law in the general process of contact electrification conveys a surface charge dissipation mechanism driven by gas medium breakdown during the surface separation stage, as shown in Figure 2.2. Consider the intimate contact between two dissimilar ideally smooth planar dielectric surfaces originally neutral in charge. Immediately after they separate and before any gas molecule flows in between, a high amount of charge is transferred between the surfaces to form a raw surface charge density σ_{r}, assuming uniform charge distribution. Without loss of generality let the charge carriers be electrons and denote the surface gaining negative charge (electrons) as the cathode and that gaining positive charge (vacancies) as the anode. As the gap increases, gas molecules fill in while the voltage V_σ across the gap is proportional to the distance d as

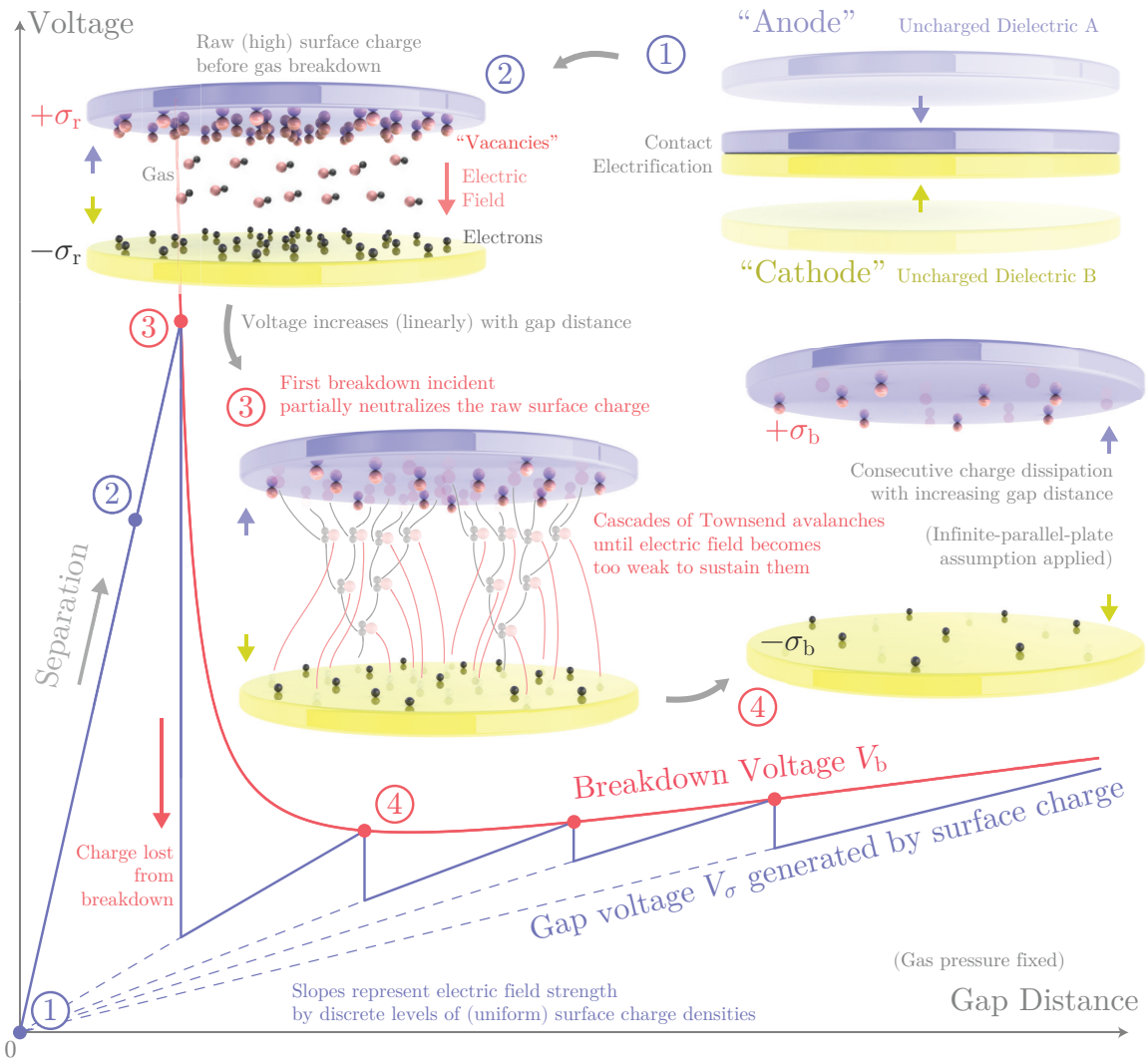

Figure 2.2. Dielectric contact electrification in a gas with constant pressure assuming validity of conventional Paschen's law: intimate contact (state 1) between perfectly flat and smooth dissimilar dielectric surfaces deposits dense (uniform) raw surface charge that generates a voltage across the gap as the surfaces separate (state 2) quasi-statically, which increases linearly with the gap distance under the infinite-parallel-plate assumption and triggers gas breakdown incidents that consecutively dissipate the surface charge and reduce the average gap voltage (states 3, 4 and so on, represented by intersections between the Paschen curve and the linear gap voltages corresponding to discrete levels of surface charge densities).

$V_\sigma = \frac{\sigma d}{\varepsilon}$, where ε is the permittivity of the gas medium and $\sigma = \sigma_\mathrm{r}$ at the beginning of separation, under the infinite-parallel-plate assumption. Similar to discussions in Section 2.1, background radiation constantly frees electrons from both surfaces (not necessarily those deposited during contact) and those escaping from the cathode are accelerated toward the anode by the electric field formed by surface charge. These electrons and occasional non-self-sustaining Townsend avalanches gradually neutralize minimal amounts of the accumulated surface charge, until the gap reaches a distance where the voltage V_σ exceeds the corresponding breakdown voltage V_b predicted by the Paschen's law. At this point (state 3 in Figure 2.2) the surface charge is dissipated by local cascades of Townsend avalanches and in the ideal case weakens the electric field to enforce $V_\sigma = V_\mathrm{b}$ for further separation. In reality the amount of charge loss at such breakdown incidents is typically quantized given the random nature of impact ionizations and secondary electron emissions, as will be verified in Section 2.4 and shown here in Figure 2.2, so that instead of overlapping the Paschen curve the gap voltage V_σ sees a sudden drop, which repeats as the voltage due to the remaining charge continues to increase when the surfaces separate further until V_σ exceeds V_b again. The final residual charge density σ_b is therefore dependent on the final gap distance (under infinite-parallel-plate assumptions) since tangent lines of the Paschen curve never cross the origin. A similar theory can be proposed if one or both of the surface materials are replaced with a conductor, which should not deviate from the above illustration if the surface charge distribution is assumed uniform.

The application of Paschen's law in contact electrification as presented has been presumed in related studies [12]–[21] but awaiting verification, especially for cases where both surfaces are insulators. The potential uncertainties of the theory exist in the aforementioned coefficient of secondary electron emission γ_se which is partially dependent on the surface material and its definition for dielectric surfaces may exhibit significant deviations from that for conductive electrodes [21]. Meanwhile, challenges for quantifying charge relaxation in dielectric contact electrification lie in the test strategies as the conventional method described in Figure 2.1 is no longer applicable. With an increasing interest in electrostatic devices exploiting post-contact surface charge as will be discussed in Chapter 4, the rest of this chapter

presents experimental approaches toward such goal of revealing behaviors of air breakdown in contact electrification to support practical analysis in applications where gas breakdown is either utilized or undesired.

2.3 Breakdown Limit of Charge Transfer in Air

Preliminary tests are done for dielectric contact electrification in room air to examine the residual charge density which is presumably limited by air breakdown. The results provide necessary information for tests with controlled air pressure in a vacuum chamber to be presented in Section 2.4, including aspects such as behaviors of contact electrification cycles, validity of charge measurement methods and estimated magnitudes of surface charge accumulation.

2.3.1 Test Strategies

A rapid apparatus is set up to perform both controlled dielectric surface contacts and surface charge measurement, where the former requires both repeatable contact force exertion and characterization of surface topography. While some existing works quantify surface roughness under microscopy [22]–[25], here its influence is excluded by examining optically smooth (locally) surfaces only as well as ensuring adequate softness for contact intimacy by involving elastomers as one of the surfaces, details of which are explained in Section 2.4.1. The measurement of dielectric surface charge, on the other hand, is conventionally done by enclosing an entire charged sample surface in a Faraday cup connected to a grounded electrometer that reads the net amount of charge [26] (or to measure twice, before and after the contact, to obtain the increment). An adaptation of this method is to replace the Faraday cup with a planar electrode (screen) on the back of the dielectric sample so that when the contacting surfaces fully separate, (image) charge of the same amount as on the insulator surface is induced to the electrode and can thus be measured *in situ* [2], [27]. Note that such inductive approaches require that the sample surfaces are distant from each other after detachment so as to exclude induction due to the opposite charge on the sample surface other than the one being measured, otherwise knowledge of more physical parameters

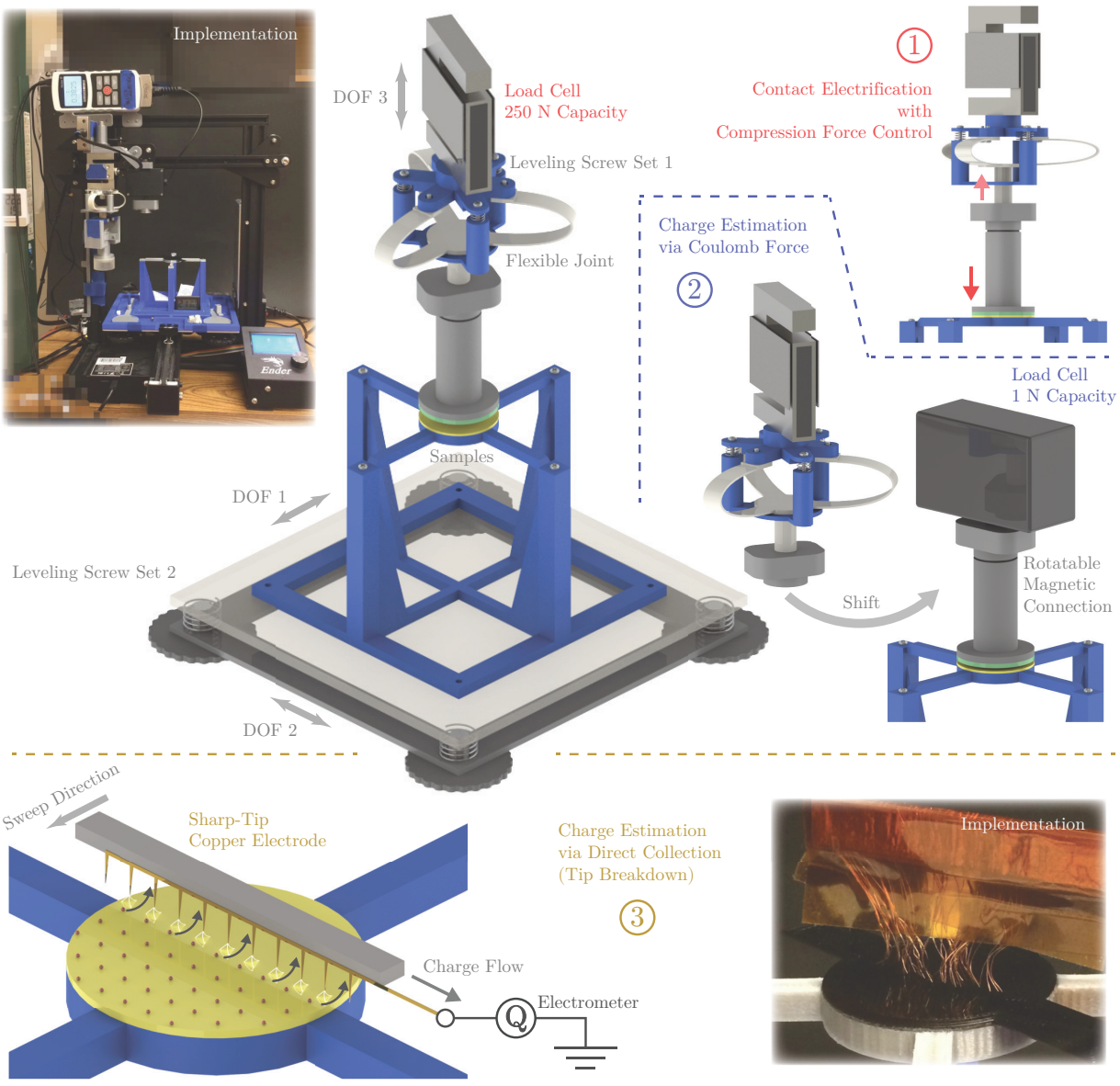

Figure 2.3. Rapid test apparatus for examination of breakdown-limited post-contact surface charge density in room air: Stage 1 - sample surface contact cycles with compression forces monitored and controlled with a 250 N load cell mounted on a 3-axis platform. Stage 2 - surface charge density measurement by estimations from the Coulomb force (attraction) between the charged surfaces with a 1 N load cell to which the top sample is transfered. Stage 3 - verification of the surface charge density measurement with destructive direct surface charge collection using a sharp-tip conductive probe grounded through an electrometer.

is required in variations of the method where surface charge densities are calculated from voltage or charge measurements with the electrometer connecting the screens of the two sample surfaces instead of being grounded [28]–[30]. This is illustrated in Figure A.1 where a preliminary investigation of the present work [31] used the inductive method to reflect dielectric surface charge accumulation in air. More advanced techniques include local charge density measurements using atomic force microscopy [32]–[35]. A known practical challenge in some of the post-contact measurements lies in the transportation of samples [30], i.e., from the apparatus for controlled contacts to that for charge measurement (Faraday cup or force microscope), during which errors can be caused by random ambient charge being attracted to the sample as noise, or direct loss of the surface charge (accidental environment breakdown, especially when the time interval between test stages is long). On the other hand, methods that monitor the charge transfer *in-situ* and are thus free of transportation issues may encounter complications by inevitably interfering with the electrification process, e.g., an insulator with an electrode (screen) on its back tends to gain more charge from contacts [2]. As a result an electrode-free post-contact charge measurement method is adopted here using the Coulomb attraction between the charged surfaces to reflect surface charge density as well as the gap voltage.

The system for controlled compression cycles consists of one sample surface fixed on the base plate of a 3-axis platform adapted from a commercial 3D printer (Creality Ender), as shown in Figure 2.3, while the other sample surface is mounted via a flexible joint onto a load cell with 250 N capacity (Mark-10 MR01-50, 0.1 N resolution). Both samples are well insulated and kept substantially far away from any grounded or massive conductor during the entire test process to avoid charge leakage. The flexible joint (printed in TPU 95A) enables smooth contact force control through its deformation and at the same time compensates any inclination between the surfaces (less than 0.15° after calibration using leveling screw set 1). The amount of charge transfer after the controlled CE cycles is measured via a two-way strategy. The top sample is first taken off the 250 N load cell and mounted onto another load cell with capacity 1 N (Mark-10 MR03-025, 0.5 mN resolution) and lowered to a certain height above the bottom surface, giving the Coulomb force (attraction) between the surfaces based on which the charge density can be calculated. In this step the inclination

between the sample surfaces is corrected using leveling screw set 2 on the base plate, i.e., two screw sets are used to parallel three surfaces (bottom sample, top sample on 250 N load cell and on 1 N load cell, respectively), and uniformity of the surface charge distribution is further examined via consistent Coulomb force measurements when rotating the top sample. The compromise is made that two load cells, instead of one, have to be used for contact force and Coulomb force measurements, respectively, due to the difference in the order of magnitudes of the contact force and the Coulomb force. The charge density deduced from Coulomb force is then verified with a direct charge collection method where a copper probe (brush) with sharp tips, which is originally placed far away (more than 1 meter) from the apparatus (to avoid error due to electrostatic induction) and grounded across an electrometer (Keithley 6514), is manually swept over the two sample surfaces consecutively so that the majority of charge accumulated on the surfaces flows to ground through air breakdown channels triggered by enhanced electric fields around the tips. The copper brush is placed back at its original location after sweeping each surface so that the increment in the charge measurement by the electrometer directly reveals the total amount of charge collected from the surface. During the sweep the copper tips are controlled to only allow point contacts with the samples to limit error due to electrification between the tips and the surfaces. Results from the two surface charge measurement methods, one nondestructive (Coulomb force) and one destructive (sharp-tip probe collection), match well in most cases as will be shown in Section 2.3.2. All preliminary test results are obtained in room air with loosely controlled temperature (between 20 °C and 22 °C) and relative humidity (between 18 % and 21 %).

2.3.2 Results and Discussions

Time histories of a complete test run where the top and bottom samples are made of silicone rubber (Ecoflex 00-20) and PTFE (Teflon), respectively, are demonstrated in Figure 2.4a, for which motion and force controls as well as data collection are implemented via the serial communication module in the QT framework. The sample surfaces are first cleaned with isopropyl alcohol and deionized water successively and then dried before mounting onto the fixtures, but they are not cleaned between test runs as it is assumed that a sharp-tip-probe

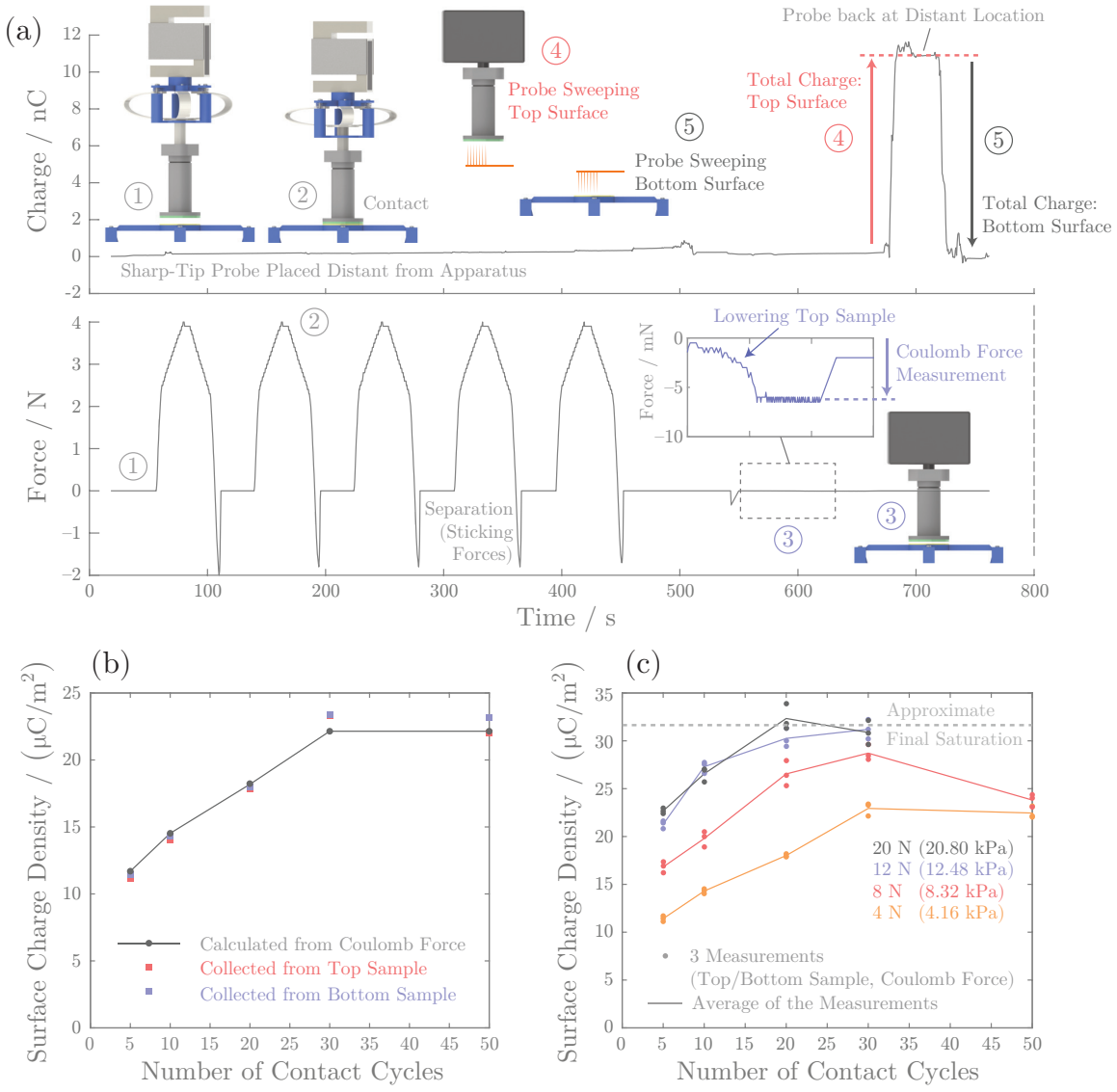

Figure 2.4. Test results of breakdown-limited contact electrification in atmospheric air with a silicone-PTFE contact pair: a) Time histories of load cell (combined, one for compression and one for Coulomb forces) and electrometer (charge flow) readings through 3 stages of a typical test run. b) Saturation of surface charge density with increased number of contact cycles under a fixed compression force magnitude of 4 N (4.16 kPa). c) Saturation of surface charge density under various compression force magnitudes exhibiting a final saturation level under sufficient force magnitude and number of contact cycles, which reflects an approximate breakdown limit in atmospheric air close to predictions by Paschen's law.

collection process sufficiently neutralizes the surfaces (further assuming that the mechanism of electrification is mainly electron transfer), effectiveness of which can be examined by a proof measurement of Coulomb force (reading zero) right before bringing the surfaces into contact. The samples undergo five contact cycles, during each the top sample is slowly lowered until a peak contact force of 4 N (4.16 kPa) is reached. When the surfaces separate a sticking force is measured which is a combination of van der Waals forces [36], air pressure and Coulomb force by the raw surface charge density. After the contact cycles the top sample is mounted onto the 1 N load cell and lowered to a certain height (1.5 mm) above the bottom sample surface and the Coulomb force is measured. The surfaces are then fully separated again and the sharp-tip probe (copper brush), which has been resting far away from the apparatus, first sweeps the top sample and is then placed back to the original location and the difference in the electrometer readings (with the probe at the same location, before and after the sweeping) represents the total amount of charge collected from the top surface. The process is then repeated for the bottom surface, which concludes the test run. In the present case the total charge collected from the top surface (silicone) reads 10.7 nC while that from the bottom surface (PTFE) reads -11 nC, yielding surface charge densities 11.12 µC/m^2 (top) and -11.43 µC/m^2 (bottom). Meanwhile the magnitude of Coulomb force reads 6 mN, indicating an average surface charge density of 11.70 µC/m^2, which is satisfactorily close to the results from direct charge collection. The estimation of surface charge density by Coulomb force is performed by releasing the infinite-parallel-plate assumption so that two circular dielectric surfaces with identical radii R, an even gap distance d and uniform surface charge densities σ_1 and σ_2 is attracted to each other with a Coulomb force magnitude of

$$|F_{\text{Coulomb}}(d,\bar{\sigma})| = \frac{d\bar{\sigma}^2}{2\varepsilon_{\text{air}}}\int_0^{2\pi}\int_0^R\int_0^R \frac{r_1 r_2}{(r_1^2+r_2^2-2r_1r_2\cos\theta+d^2)^{\frac{3}{2}}}\,\mathrm{d}r_1\,\mathrm{d}r_2\,\mathrm{d}\theta\ , \tag{2.2}$$

where $\bar{\sigma}^2 = |\sigma_1\sigma_2|$ and ε_{air} is the permittivity of air, and as $d \to 0$ the infinite-parallel-plate assumption is approached so that $|F_{\text{Coulomb}}| \to \dfrac{\pi R^2\bar{\sigma}^2}{2\varepsilon_{\text{air}}}$.

The same combination of materials (silicone against PTFE) is then tested under same conditions while varying the number of contact cycles, as shown in Figure 2.4b where the residual surface charge density generally increases after more cycles while reaching saturation.

The tests are then repeated while also varying the peak contact force, results of which are plotted in Figure 2.4c. It shows that an increased contact force generally raises the residual charge density after a fixed number of cycles while a saturation also exists when the force exceeds a threshold. In summary, the residual surface density increases both with larger contact forces and with increased number of contact cycles, and when the force and number of cycles both reach a threshold a final saturation level is obtained which in the case of silicone-PTFE contacts under study is around $30\,\mu C/m^2$. This may be briefly explained by conceptually envisioning the microscopic surface topography, as depicted in Figure 2.5. In multiple contact cycles the surfaces engage with tiny random offsets that are however large enough compared to the size of surface asperities so that different regions on the asperities are electrified, and the surface charge density saturates when all reachable regions have been contacted. There are, however, corners or cavities that can only be covered when the global contact force is increased so that the surfaces may engage with greater depth. It can then be concluded that the dual final saturation reflects a nearly full effective contact area where charge is deposited, so that the saturated charge density is a reasonable estimation of the breakdown limit for the given test conditions.

The dual saturation behavior is further studied for two other material combinations by fixing the number of contacts at 20 (assumed enough for saturation, at least under large forces, and varying the contact force, results of which are shown in Figure 2.5c. The saturation level previously found for the residual charge density (around $30\,\mu C/m^2$) appears universal for all tested cases. While the top sample is fixed as silicone thanks to its stretchability to ensure intimate contacts, it gains negative charge when pressed against nylon or ABS but gains positive charge against PTFE. The fact that it is charged with opposite polarities but still saturates at the same magnitude of charge density indicates that the saturation level is governed by air breakdown instead of being intrinsic of the silicone material. A quick examination can be done using a rough knowledge of the dielectric strength of air [18] being around $3\,kV/mm$, which is equivalent to the electric field strength generated by infinite parallel dielectric plates with surface charge densities equal in the magnitude of $26.6\,\mu C/m^2$, which is comparable to the observations. At the meantime, Paschen's law 2.1 for atmospheric air [37] assuming $p = 1.013 \times 10^5\,Pa$, $A_g = 11.25\,Pa^{-1}\,m^{-1}$, $B_g = 273.75\,V\,Pa^{-1}\,m^{-1}$ and

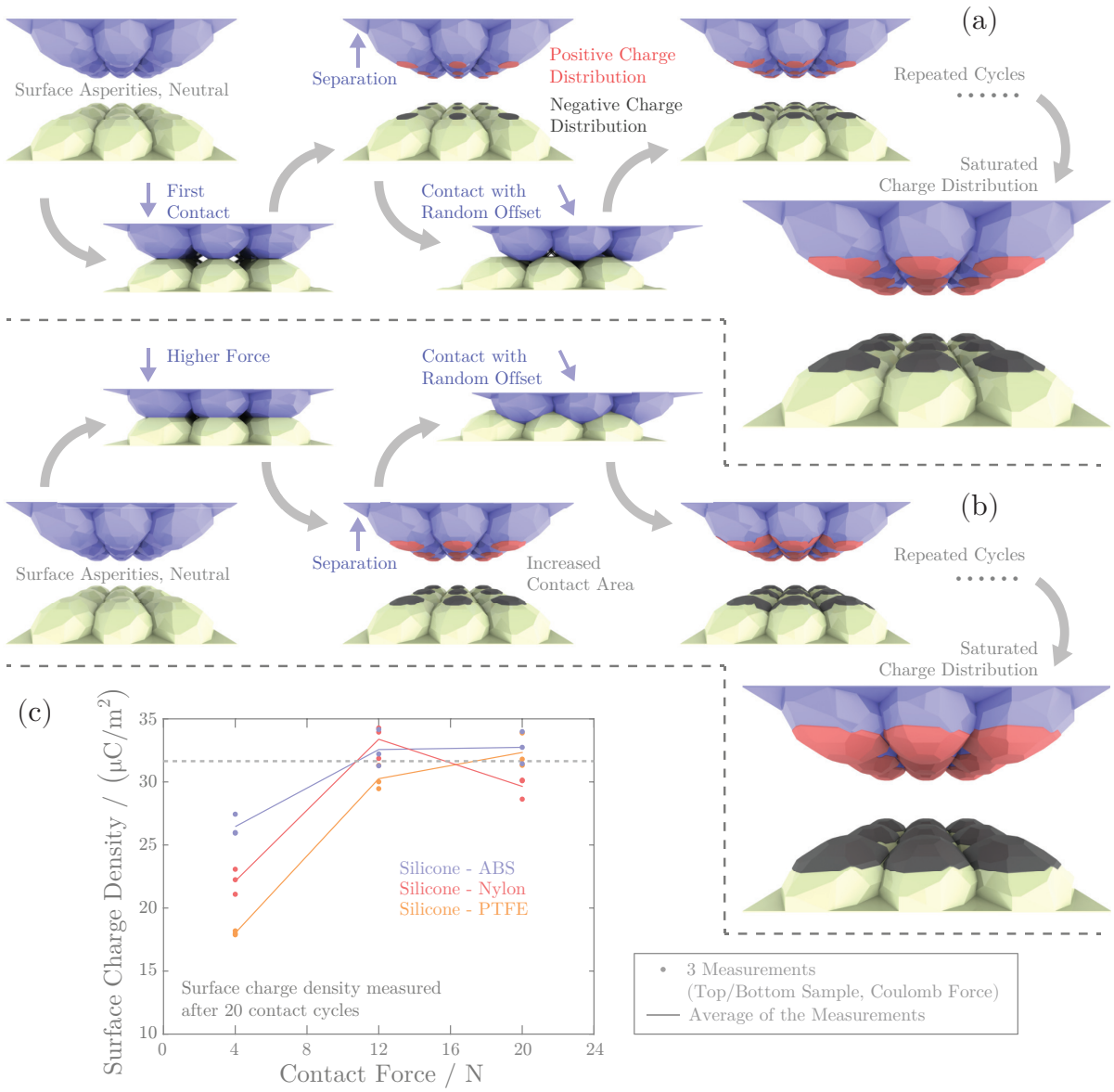

Figure 2.5. Dual saturation trend of post-contact surface charge density with respect to number of contact cycles and magnitude of compression force: a) Surface charge density saturates with number of contact cycles due to microscopic offsets in between, which covers all reachable areas with a fixed magnitude of compression force. b) Surface charge density saturates with increased compression force which deposits charge in more corners and cavities as the surface asperities engage deeper. c) Universal surface charge density saturation with various contact pairs where the number of contact cycles is fixed while compression force magnitude is varied.

$\gamma_{se} = 0.02$ (conventionally determined for copper electrodes) predicts a saturated residual charge density of around $30\,\mu C/m^2$ for a final gap distance of 10 mm to 20 mm which roughly estimates the separation in the conducted tests before switching the load cells, not taking into consideration the decreasing validity of the infinite-parallel-plate assumption with increasing gap distance. It reveals that the raw charge density for all three material combinations are beyond the air breakdown limit and therefore the measured charge densities at saturation are dominated by the breakdown process toward the same level. An auxiliary test has also been briefly done to attribute the saturation level to air breakdown, where the sample surfaces are manually compressed against each other and after each contact the sharp-tip probe is used to collect charge from only one of the surfaces. The charge collected from the single surface decreases to zero as the number of contacts increases, and eventually the surface charge density on the other surface, which has not been cleaned ever by the electrode, reaches a level approximately double that of the original saturation level.

The preliminary tests done in atmospheric air serve as the preparation for those to be performed in a vacuum chamber where air pressure can be varied. Besides revealing a universal limit for residual surface charge density dominated by air breakdown, the tests have also verified the method of using Coulomb force measurements to estimate surface charge densities via comparisons to direct charge collection using conductive probes. This is helpful since the charge collection can hardly be achieved in a vacuum chamber not only due to challenges in the apparatus design but also because the sharp-tip discharge also relies on air breakdown which is to be suppressed in vacuum. Meanwhile, the charge collection step also tells the polarity of the contacting surfaces, which can not be decided from the Coulomb force alone.

2.4 Experimental Verification of Paschen's Law in Contact Electrification

Dielectric contact electrification is performed in a vacuum chamber in order to investigate the validity of Paschen's law in its separation stage. A test setup reconstructed from that in room air (Figure 2.3) is detailed in Section 2.4.1, which is used to measure the breakdown

voltage between the charged surfaces at various gap distances and air pressures, as illustrated in Section 2.4.2, results of which are discussed in Section 2.4.3.

2.4.1 Apparatus Setup and Sample Fabrication

A test apparatus simplified to fit in an acrylic vacuum chamber (12-inch cubic, with an absolute pressure gauge, manufactured by Sanatron) is assembled as shown in Figure 2.6. The bottom sample surface is mounted on a load cell (1 N capacity, 0.5 mN resolution, for Coulomb force measurements) which is fixed on the base via a set of 4 leveling screws which calibrates its orientation. Unlike the tests in air where the 1 N load cell is not involved in the contact cycles, here it undergoes all compression and sticking forces for which a pair of external mechanical stops is applied to protect it from overloading. The top sample surface is mounted on another load cell (25 N capacity, 0.1 N resolution, for monitoring contact and sticking forces) whose motion is driven by a pair of synchronized stepper motors with a resolution of 0.02 mm in displacement control. All mechanical connections and fixtures are printed in ABS and PLA plastic, while all analog signals (load cell outputs and input to the motors) are transmitted via a customized wire feedthrough on the back of the vacuum chamber.

The bottom sample is chosen among commercially available insulators while the top sample is fixed as PDMS (Sylgard 184) favoring its appropriate stretchability so that it ensures intimate contact with the bottom surface while being stiff enough to neither exhibit a significant deflection under remarkable Coulomb forces nor impede surface separation with a large deformation under the sticking force. It is fabricated by casting PDMS in a circular ABS sample holder pressed against a smooth plastic surface, as demonstrated in Figure 2.7, where liquid PDMS is injected through channels at its bottom which then ventilates any bubbles generated during the injection and compensates any shrinkage or leakage of the curing liquid. The cured PDMS replicates the smoothness of the plastic surface and its stiffness prevents any distortion of the sample when the plastic sheet is peeled off. Girders are printed on the floor of the mold so that when liquid PDMS surrounds them and cures they surve as a mechanical lock to grip the PDMS sample without any chemical bond. The

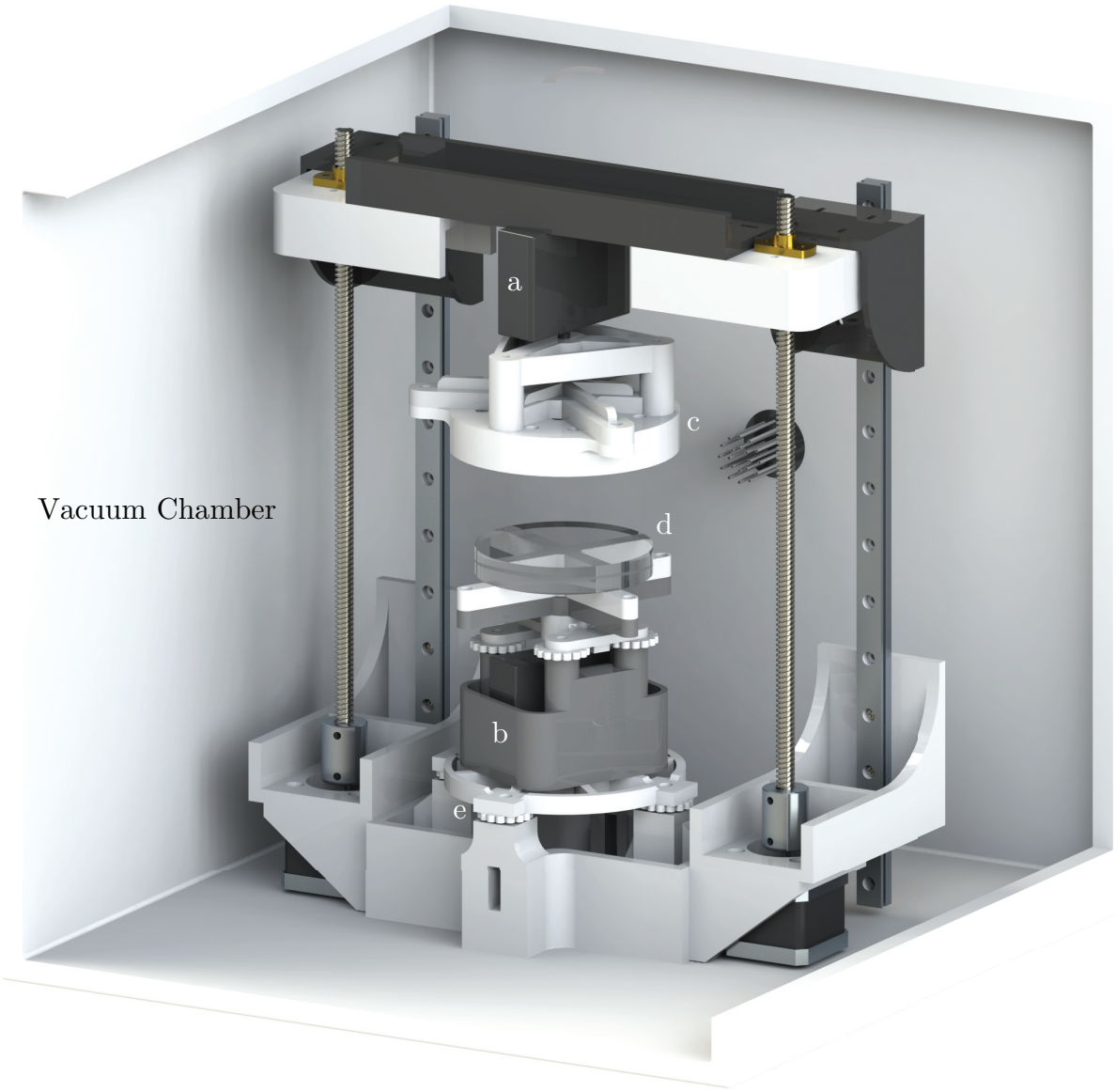

Figure 2.6. Test apparatus in a 12-inch cubic vacuum chamber with digital pressure monitor (0.1 mTorr resolution) and wire feedthroughs for stepper motor controls and sensor outputs: a) Top load cell (25 N capacity, 0.1 N resolution) for compression and sticking force measurements. b) Bottom load cell (1 N capacity, 0.5 mN resolution) for Coulomb force measurements, installed with external mechanical stops for overload protection. c) Top sample surface: clear PDMS elastomer cast directly in a mold with mechanical locks (see Figure 2.7). d) Bottom sample surface: acrylic as anode or PTFE as cathode against PDMS (Chapter 2), or other dielectric surfaces (Chapter 3). e) A set of 4 leveling screws for surface alignment.

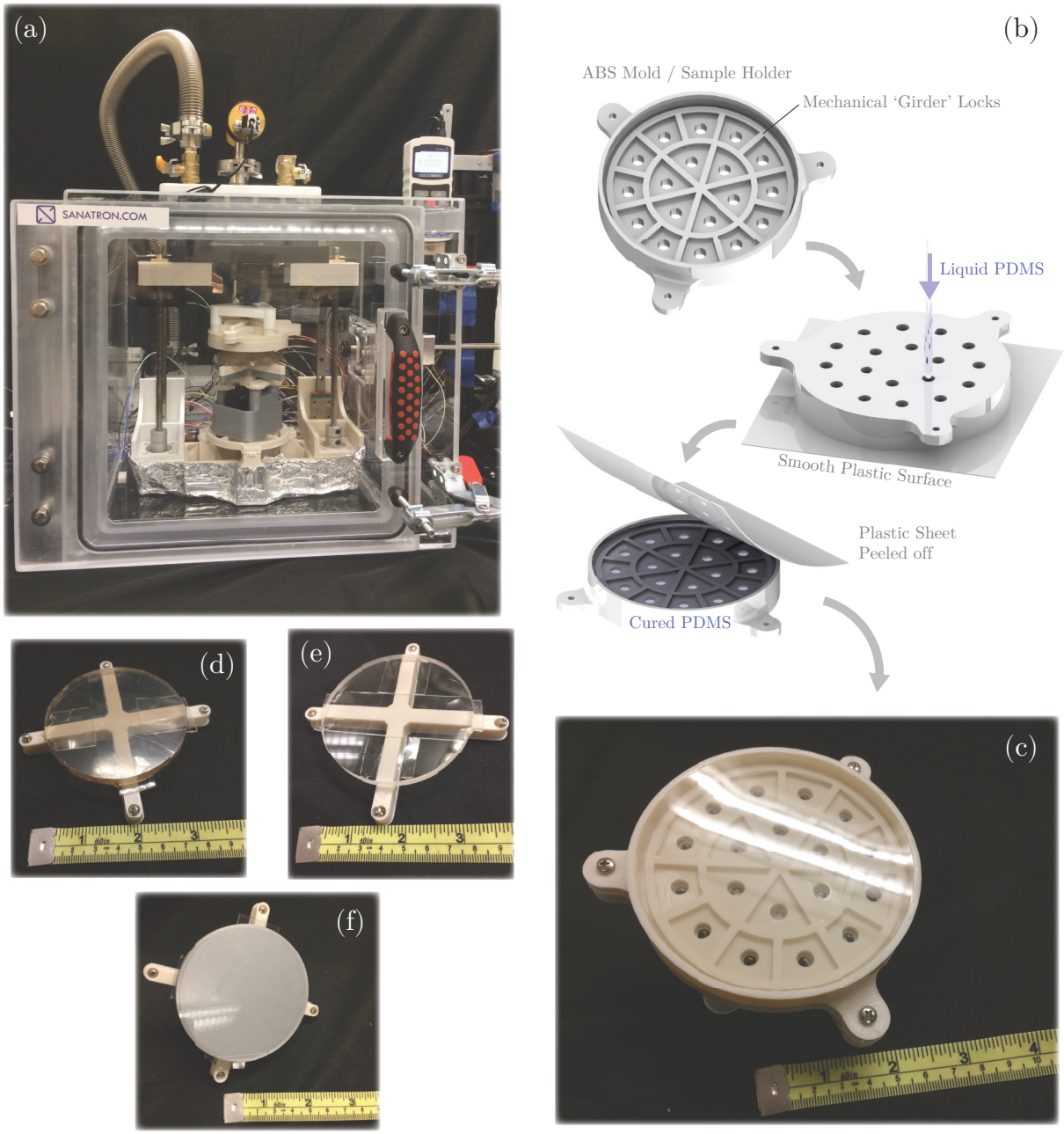

Figure 2.7. Test apparatus implementation and sample fabrication: a) Test apparatus in vacuum chamber. b) Fabrication of c) the top sample surface by casting PDMS in an ABS mold (with mechanical locks) pressed against a smooth plastic sheet. Bottom samples surfaces include d) PTFE, e) acrylic and f) PLA.

bottom sample has a diameter of 76.2 mm (3 in) and the top sample has an effective diameter of 95 mm, both of which are considerably large as a compromise to ensure a reasonable signal-to-noise ratio in Coulomb force measurements, especially when the minimum voltage (as in Figure 2.1c) is to be revealed in the tests.

2.4.2 Test Strategies

Paschen's law 2.1 considers the dependence of breakdown voltage on two variables, gas pressure p and gap distance d, and test strategies are designed accordingly. Air breakdown in contact electrification is first investigated by fixing a gap distance between two charged dielectric surfaces and observing the charge dissipation when air pressure is varied in the vacuum chamber. The test steps are illustrated in Figure 2.8 where two halves of the Paschen curve, divided at $pd = \frac{\mathrm{e}}{A_\mathrm{g}} \ln\left(1 + \gamma_\mathrm{se}^{-1}\right)$ where the minimum breakdown voltage is achieved (Section 2.1), are examined separately. In a vacuum-to-air test the pressure in the vacuum chamber is first pumped below 200 mTorr, after which the sample surfaces undergo several contact electrification cycles to obtain a certain surface charge density. During the contact cycles an infinitesimal separation is not achievable due to the existence of sticking forces, but the maximum separation is limited (less than 1.5 mm) to avoid any air breakdown before following steps. The surfaces are then brought to the destination gap distance (with a certain voltage across the gap induced by the raw surface charge, state 2) and air is slowly released into the chamber (voltage is fixed, step 2) until the Paschen's law predicts a breakdown incident (state 3) which dissipates a certain amount of surface charge, resulting in a reduced voltage (state 4). A series of breakdown incidents dissipate the surface charge consecutively as the air pressure continues to increase (step 3) until the gap voltage is lower than the minimum breakdown voltage predicted by Paschen's law so that this gap voltage survives till the end of the test where the pressure reaches atmosphere. The Coulomb force between the surfaces and the corresponding air pressure are recorded so that drops in the gap voltage calculated from Coulomb attraction measurements indicate intersections with the left half of the Paschen curve. An air-to-vacuum test follows a similar procedure where the sample surfaces undergo contact electrification cycles under atmospheric pressure, dur-

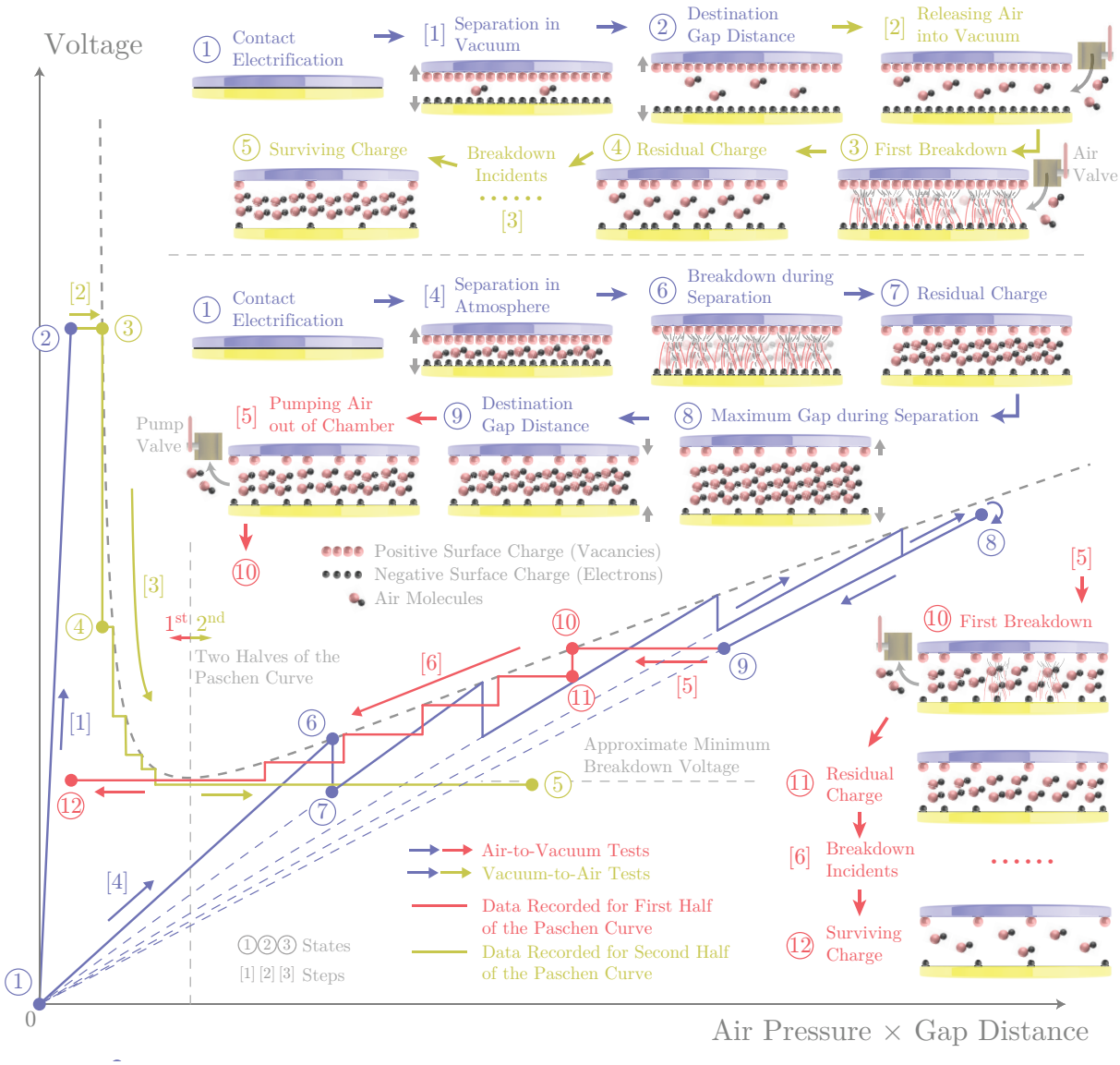

Figure 2.8. Steps of fixed-gap varied-pressure tests for verification of Paschen's law: Two independent procedures, vacuum-to-air and air-to-vacuum, indicated by paths starting with steps 1 and 4, respectively, are used to examine two halves of the Paschen curve. Steps with a nonzero slope represent variation of gap distance under fixed air pressure while those with a zero slope represent variation of pressure with a fixed gap. Breakdown incidents implied by drops in the monitored Coulomb attraction (and thus the voltage) between the surfaces are recorded as intersections with the Paschen curve. The voltage (Coulomb force) that survives in the end of each test is recorded to approach the infimum breakdown voltage predicted by Paschen's law.

ing which breakdown of the air is however inevitable under the given circumstances. The gap voltage exceeds the breakdown voltage predicted by Paschen's law for atmospheric air when the surfaces are separated to some minor gap distance around several micrometers (step 4 to state 6). When the surfaces reach a maximum distance during separation in the contact electrification cycles, the surface charge density is already reduced after a series of breakdown incidents (state 8) so that it is generally lower than the initial charge density in vacuum-to-air tests. The surfaces are then brought to the destination distance (state 9) and air is slowly pumped out of the chamber (voltage is fixed, step 5) to trigger a breakdown incident (state 10) followed by more until the gap voltage falls below the minimum breakdown voltage. The tests can be repeated at different destination gap distances where a same voltage reflects a lower charge density at a larger gap and thus a lower Coulomb attraction so that the resolution of the load cell may not be satisfactory for revealing the minimum breakdown voltage. Therefore ideally a small destination gap distance is preferred, especially since the gap voltage is proportional to the surface charge density while the Coulomb force is proportional to it squared. Practically the destination gap is chosen around 0.5 mm as a compromise between confidence in Coulomb force measurements and that in surface alignment.

Paschen's law is then examined with fixed-pressure varied-gap contact electrification tests which simulate the general separation process discussed in Section 2.2 and Figure 2.2, and detailed in Figure 2.9. The tests start in vacuum (below 200 mTorr) where the samples undergo several contact cycles to deposit an arbitrary amount of surface charge (state 1). They are then separated to a minimal gap around 0.2 mm (step 1 to state 2) although practically the separation results in a larger gap after overcoming sticking forces and the surfaces are retracted back to the minimal gap (state 2). Air is then briefly released into the chamber until a destination pressure is reached (step 2 to state 3 or 6), after which the gap is slowly enlarged while the destination pressure is maintained (step 3 or 4), until Paschen's law predicts the breakdown air in between (step 4 or 7). A series of drops observed in the gap voltage (Coulomb force) as the surfaces separate further are then recorded to represent intersections with the Paschen curve until the Coulomb force measurements are within the noise level of the load cell. The tests can be repeated under different destination pressures

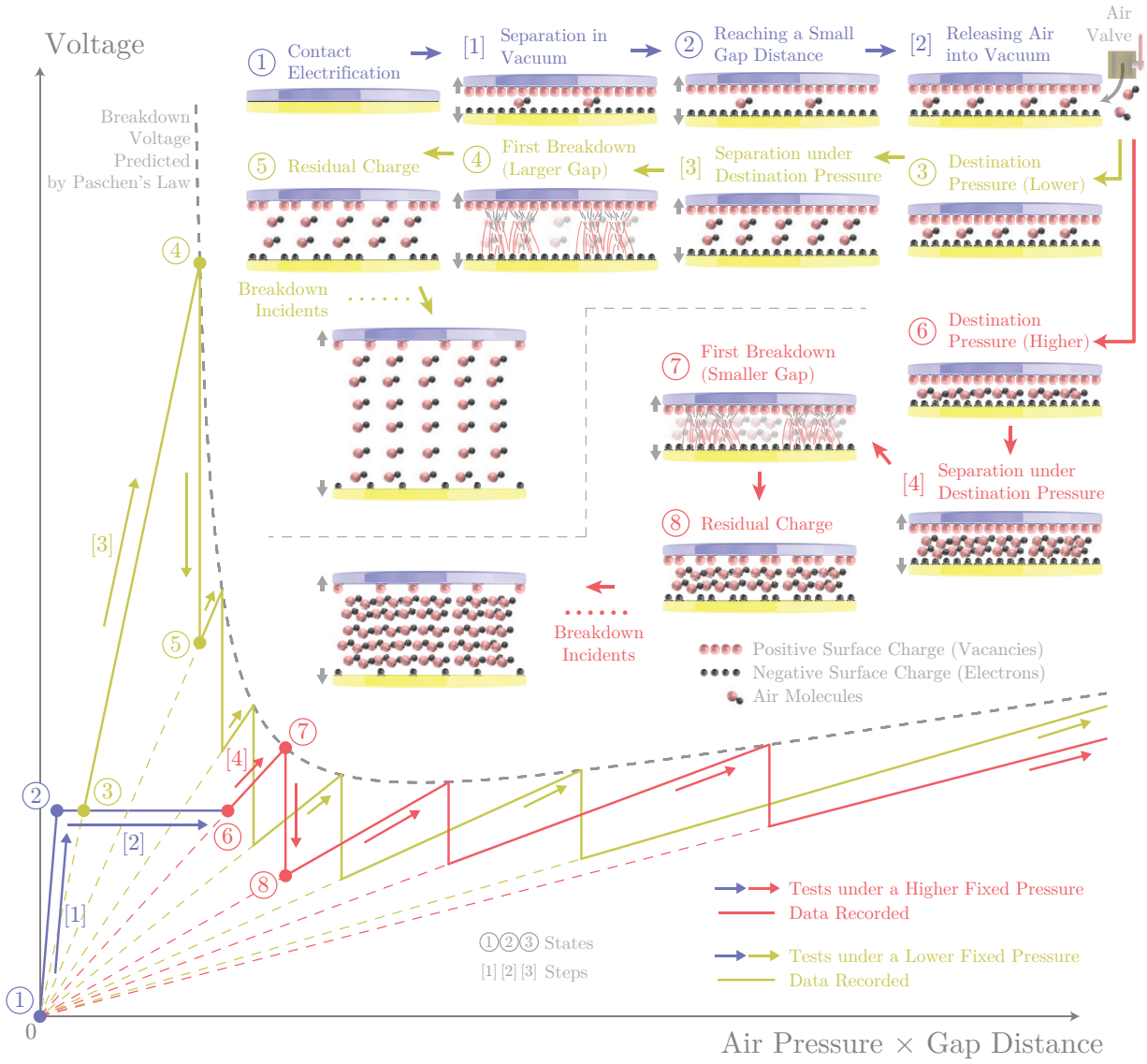

Figure 2.9. Steps of fixed-pressure varied-gap tests for verification of Paschen's law: Sample surfaces are charged in vacuum below 200 mTorr (state 1) and slowly separated at a destination air pressure (step 3 or 4) until a series of breakdown incidents (drops of gap voltage reflected by Coulomb force measurements) are recorded as intersections with the Paschen curve. Tests under a higher destination pressure reveals further parts of the Paschen curve (to the right) given limited load cell resolution and assuming a same raw surface charge density right after separation.

where breakdown incidents are triggered earlier (at smaller gap distances) under a higher destination pressure (the separation is represented with a lower slope in Figure 2.9 for a higher pressure) so that tests under a lower destination pressure reveal the nearer part (to the left) of the Paschen curve while those under a higher pressure reveal the farther part (to the right) given the same raw surface charge density and load cell resolution. Unfortunately with practical limitations the fixed-pressure varied-gap tests can hardly reveal the second half of the Paschen curve (defined in the Figure 2.8).

The voltage V across the gap in all tests is estimated from Coulomb force measurements by first calculating the surface charge density $\bar{\sigma}$ using Equation 2.2 and then applying the infinite-parallel-plate assumption so that $V = \dfrac{\bar{\sigma} d}{\varepsilon_{\text{air}}}$ where ε_{air} is the permittivity of air and d is the gap distance, which, although is less valid near edges of the surfaces when the distance increases, is not further corrected like what is done for the Coulomb forces since it predicts the maximum local voltage (typically at the center of the samples) which, instead of the average voltage, is what triggers the breakdown. Before each test the surfaces are brought to a considerably large gap (15 mm) and the air pressure inside the vacuum chamber is swept from atmospheric to below 200 mTorr to eliminate any residual surface charge, at which point the load cells are zeroed.

2.4.3 Results and Discussions

Air breakdown between the contact pair PDMS (top) and acrylic (bottom) is investigated using the above test strategies and Figure 2.10 exhibits results of test runs at destination gap distances of 0.3 mm and 0.44 mm, for which the theoretical Paschen curves (assuming air between copper electrodes) are depicted for reference. The predicted behavior of consecutive discharge incidents by air breakdown is revealed in both vacuum-to-air and air-to-vacuum tests and the combination of sample size and load cell resolution manages to capture the survival of a certain amount of surface charge after sweeping the air pressure in each test run, which closely reflects the minimum breakdown voltage predicted by the conventional Paschen's law. The air pressure at which the minimum voltage is arrived at, i.e., approximately 30 Torr for the 0.3 mm gap and 20 Torr for 0.44 mm, is fairly consistent for the

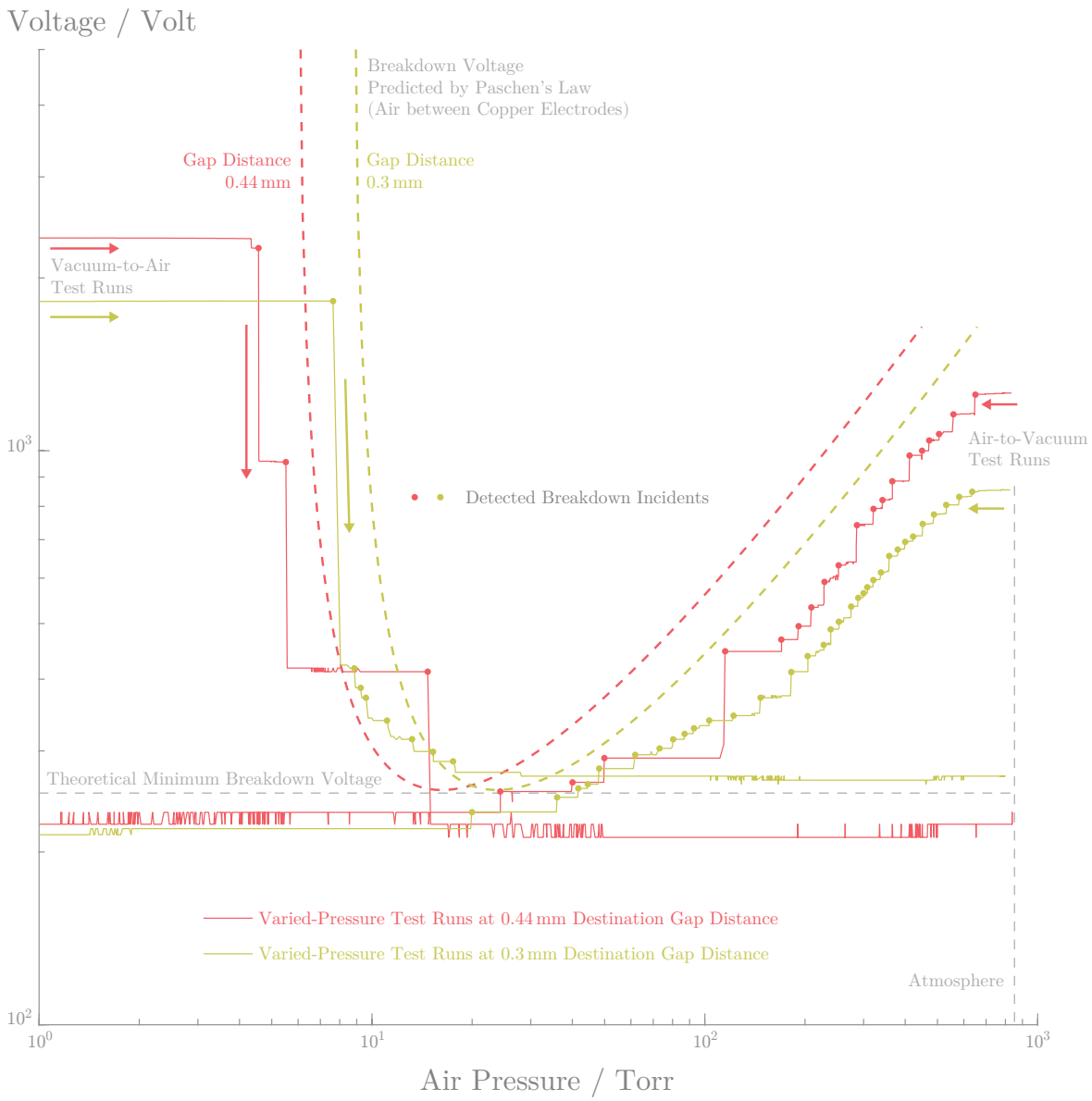

Figure 2.10. Fixed-gap varied-pressure test runs for a PDMS-acrylic contact pair: Two tests, one from atmospheric air to vacuum and one from vacuum to air, are performed at two destination gap distances 0.3 mm and 0.44 mm, respectively, where the corresponding breakdown voltage predicted by conventional Paschen's law (assuming air between copper electrodes) as a function of air pressure is depicted as reference, while detected significant drops of gap voltage are marked as indications of breakdown incidents.

two test runs at each destination gap distance and comparable to the theoretical values of 23.8 Torr and 16.2 Torr for the 0.3 mm and 0.44 mm gaps, respectively. Drops of the gap voltage in test runs at a 0.44 mm gap are generally more significant than those at a 0.3 mm gap since for a larger gap a given amount of charge loss results in a higher voltage drop and meanwhile more air molecules are involved in Townsend avalanches. Varied-gap tests at several destination air pressures are exhibited in Figure 2.11 with reference of the corresponding breakdown voltage predicted by Paschen's law as a function of gap distance. Most test runs reveal only intersections with the first half of the Paschen curve since further breakdown incidents as the gap increases are not detectable due to limited load cell resolution as well as the decreasing Coulomb force following Equation 2.2. A series of minor discharge incidents are monitored closely before the first significant breakdown, e.g., in test runs at 0.2 Torr destination pressure, which are preliminarily attributed to non-self-sustaining local avalanches. All results for the PDMS-acrylic contact pair can be gathered as in Figure 2.12 to display the dependence of breakdown voltage on the product of air pressure and gap distance, where varied-gap and varied-pressure test runs coincide fairly well along the first half of the unique theoretical Paschen curve. The detected breakdown incidents are further collected in Figure 2.13 with error bars showing the propagation of precision errors.

Similar tests are performed with two other bottom samples, PTFE (tape) and PLA (3d-printed), with results presented in Figure 2.14. Minor discharge incidents before the first significant breakdown incident are again observed in varied-gap tests at low destination pressures, i.e., PTFE at 0.2 Torr and PLA at 0.4 Torr, while tests at high destination pressures briefly hint the arrival at the minimum breakdown voltage, i.e., PTFE at 4 Torr and PLA at 9.5 Torr. In most test runs the breakdown incidents occur earlier than predictions by the conventional Paschen's law. Despite the potential deviation from the theoretical breakdown voltage due to difference in surface materials (PDMS against selected insulators under consideration, while copper electrodes in theory) and thus in the coefficient of secondary electron emission, it is also attributed to the potential non-uniform surface charge density so that air breakdown is always triggered at locations with a voltage higher than the recorded average gap voltage. Moreover, errors in the representation of gap distance using stepper motor feedback can be caused by misalignment of the surfaces as well as deflections of components in

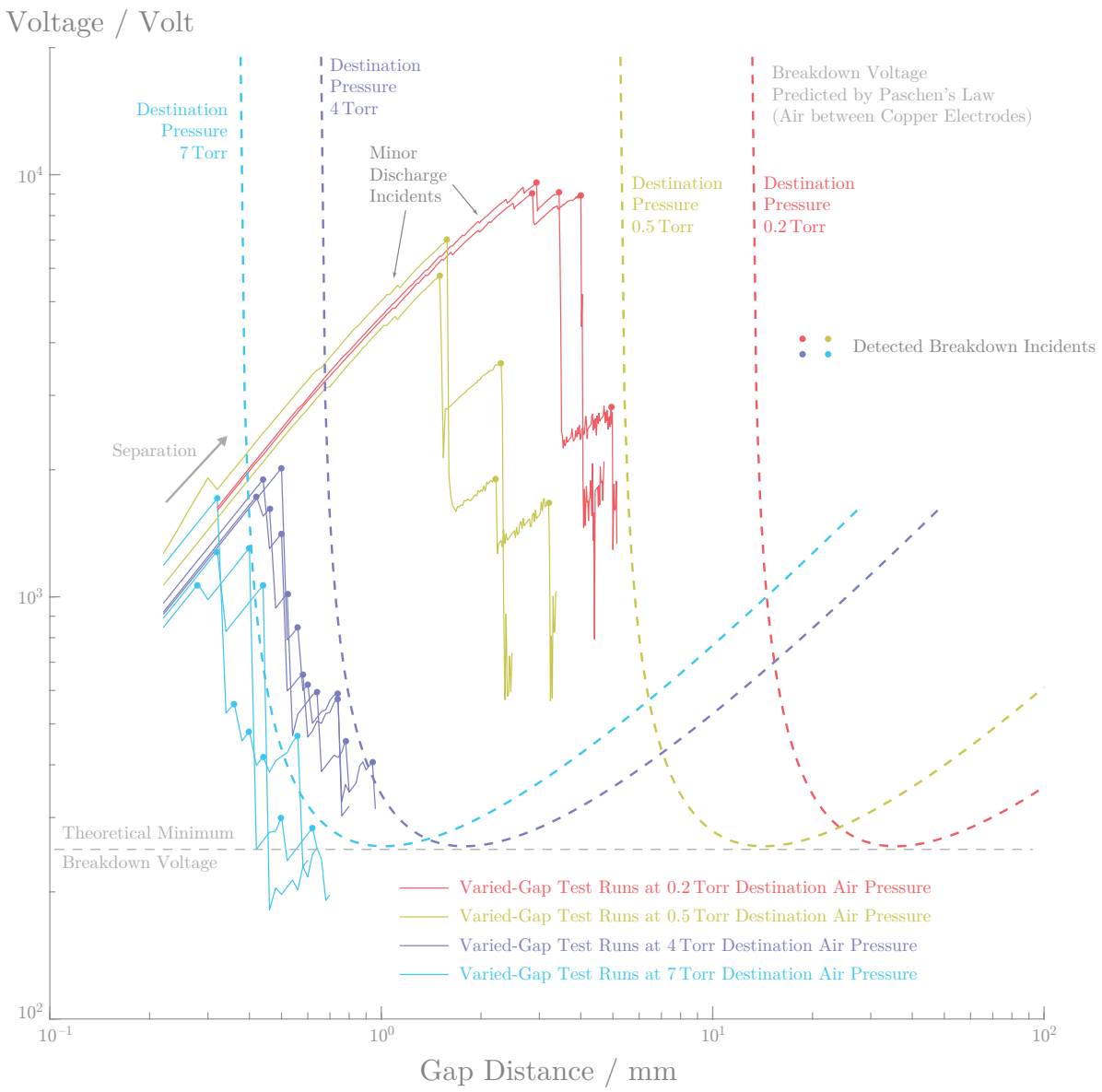

Figure 2.11. Fixed-pressure varied-gap test runs for a PDMS-acrylic contact pair: Multiple test runs are performed at several destination air pressures 0.2 Torr, 0.5 Torr, 4 Torr and 7 Torr, where the corresponding breakdown voltage predicted by conventional Paschen's law (assuming air between copper electrodes) as a function of gap distance is depicted as reference, while detected significant drops of gap voltage are marked as indications of breakdown incidents.

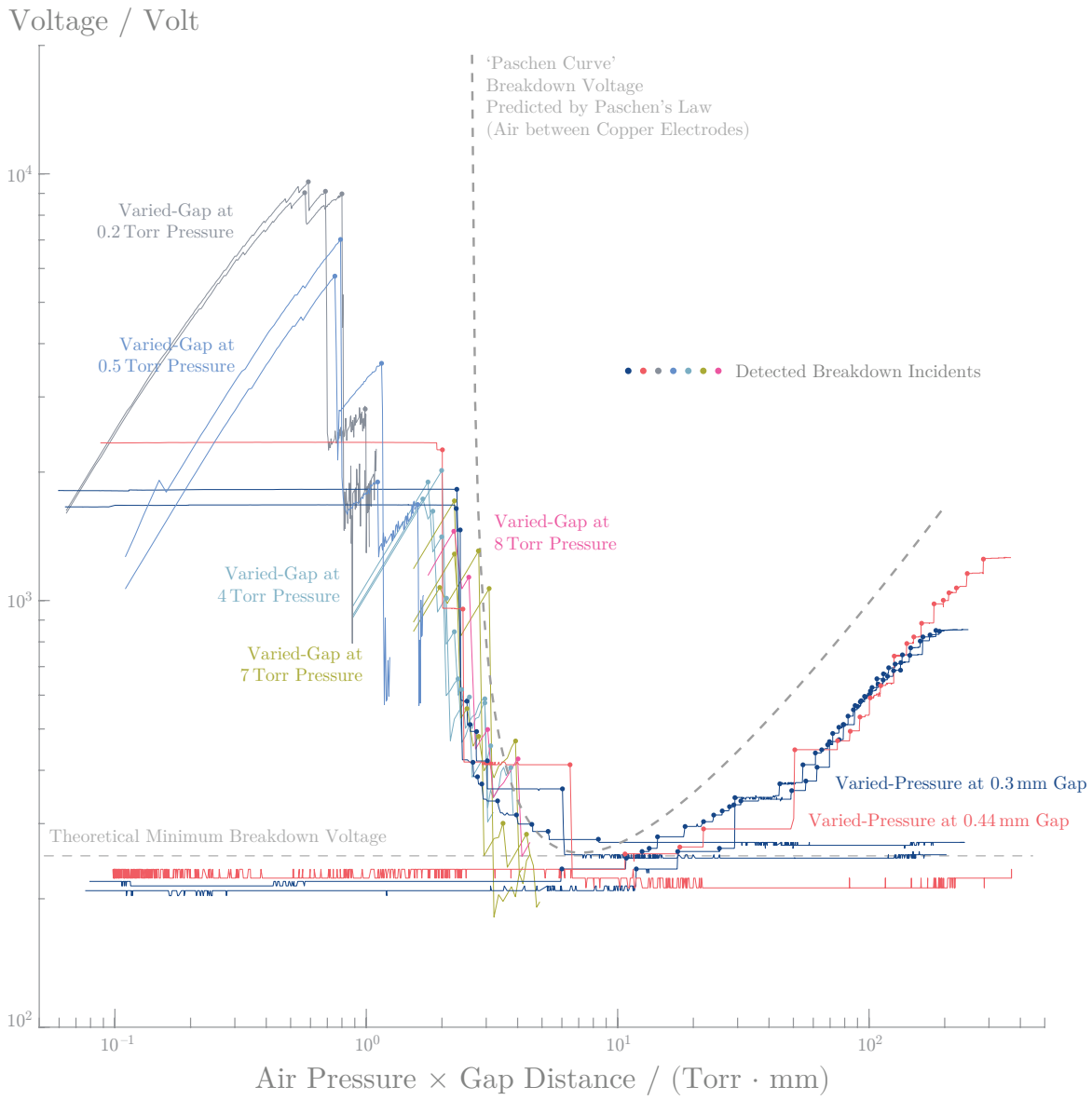

Figure 2.12. Gathered results for a PDMS-acrylic contact pair: All varied-gap and varied-pressure test results are collected to reveal the dependence of breakdown voltage on the product of air pressure and gap distance where the unique theoretical Paschen curve for air between copper electrodes is shown as reference.

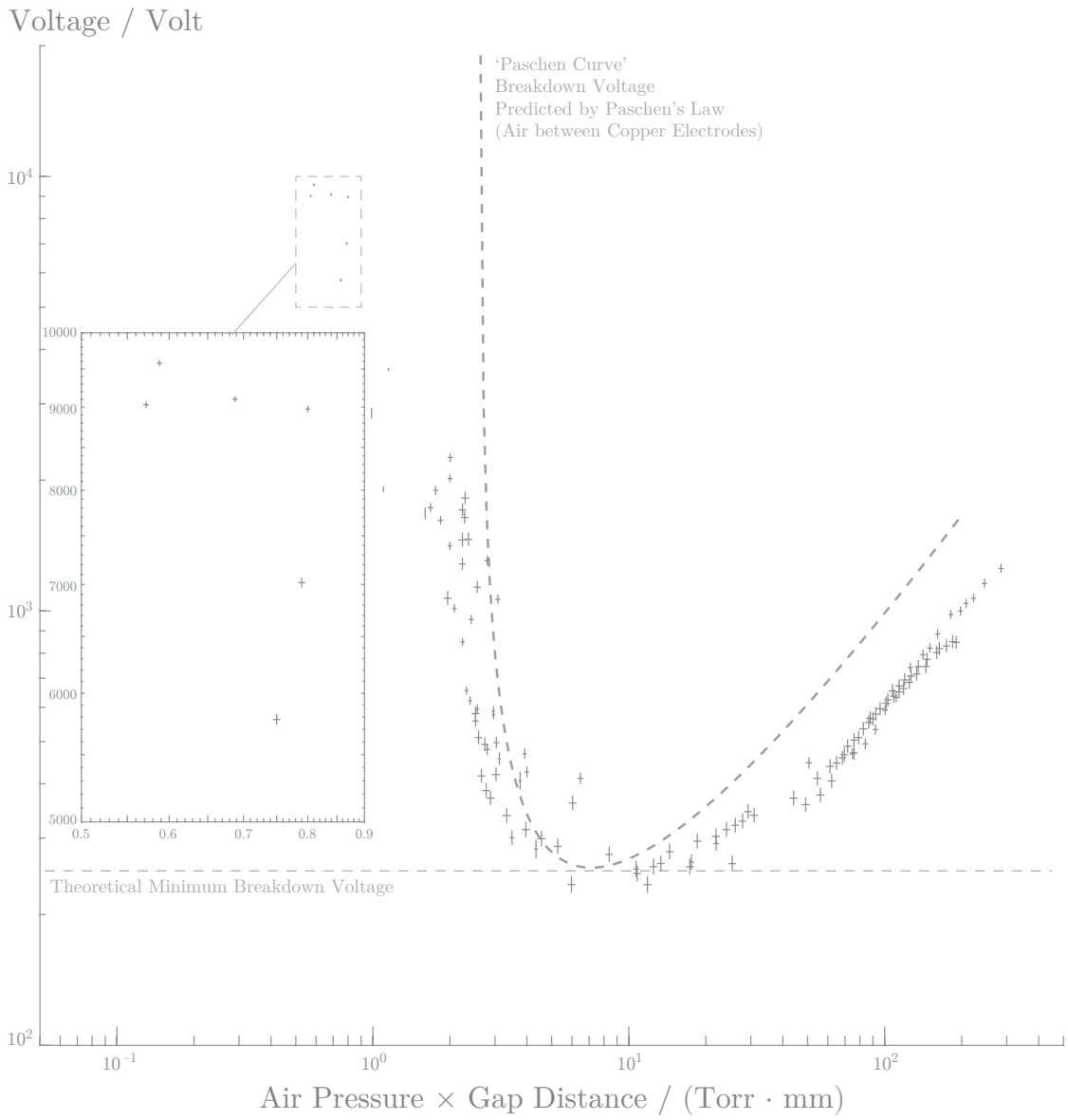

Figure 2.13. Extracted air breakdown points for a PDMS-acrylic contact pair: Horizontal error bars indicate the combination of precision errors in displacement (stepper motor, 0.02 mm resolution) and air pressure (gauge, floating resolution with 3 significant digits) measurements, and vertical error bars indicate the propagation of precision errors in displacement and Coulomb force (load cell, 0.5 mN resolution) measurements in the calculation of gap voltage.

the apparatus such as mechanical fixtures, the bulk PDMS elastomer and the load cell shaft. Nonetheless, it is implied that the experimentally determined Paschen curves suggest a more accurate safe region for test conditions (combination of air pressure and maximum gap distance) within which significant charge loss due to air breakdown can be eliminated. More importantly, even with such conservative criteria the required constraints of air pressure and gap distance are fairly feasible and are applied in Chapter 3 to uncover the accumulation of raw surface charge density for the electrification between multiple contact pairs.

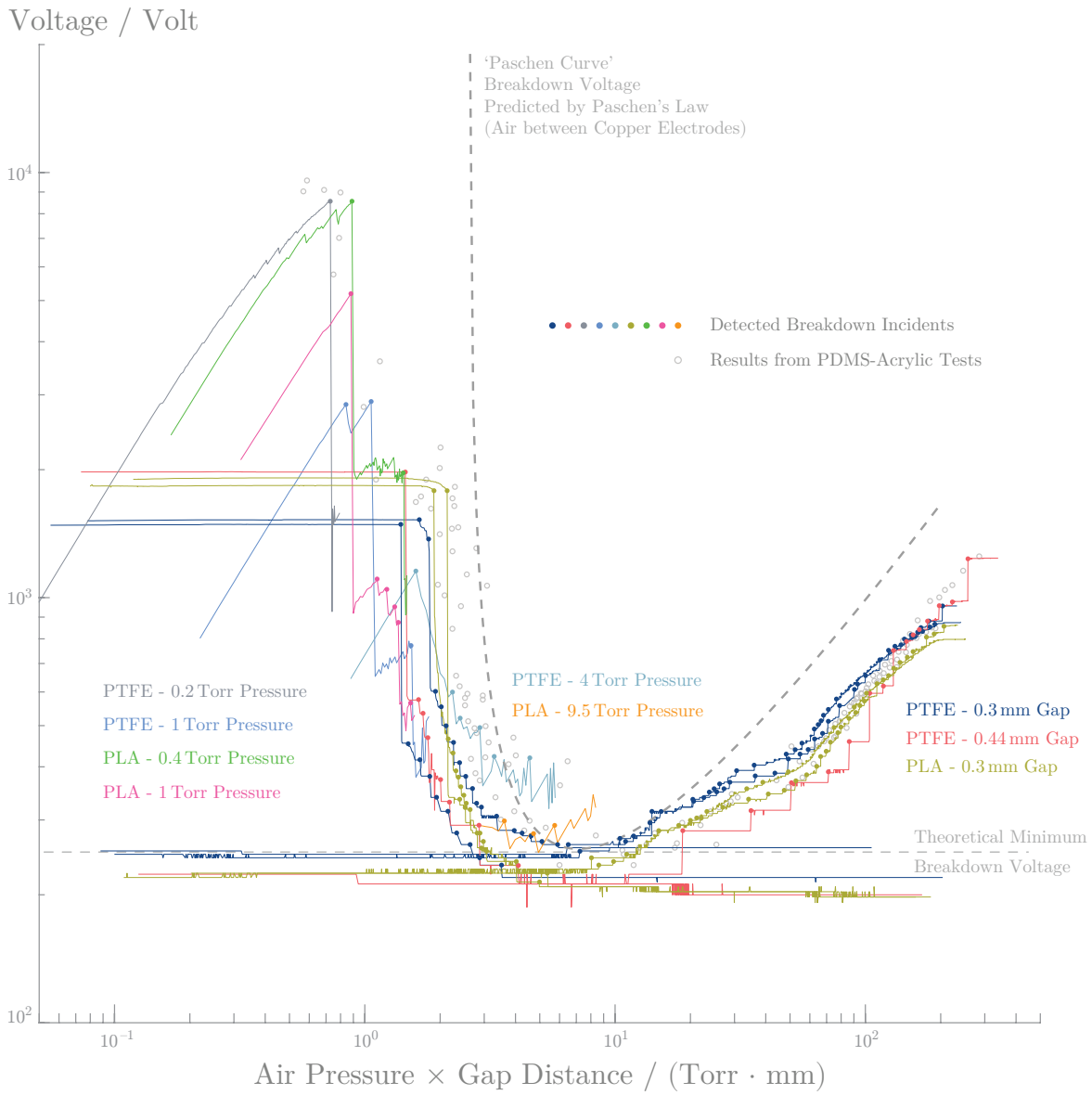

Figure 2.14. Gathered results for PDMS-PTFE and PDMS-PLA contact pairs with PDMS-acrylic results shown as reference.

3. QUANTIFYING RAW TRIBOELECTRIC CHARGE

Observations of the air breakdown behavior in the separation phase of general contact electrification instruct experimental investigation of the raw amount of charge transfer toward the goal of analyzing the charge carriers. Test strategies based on Section 2.4.2 are illustrated in Section 3.1 and performed in Section 3.2.

3.1 Motivation and Test Strategies

Characterization of contact electrification is challenging as experimental results are known to be highly unrepeatable due to difficulties in controlling test conditions as well as the interference by breakdown of the medium as discussed in Chapter 2. The presented verification of Paschen's law reveals the possibility of eliminating breakdown discharge in the contact charging process, with the presumption that the initial phase in both fixed-pressure and vacuum-to-air fixed-gap tests represents the raw surface charge density before the first breakdown incident. It is then expected that investigations on various other aspects of contact electrification can be achieved if contact cycles are performed with air pressure and final gap distance controlled so that the combination of their product and the gap voltage is distant from regions above the (experimental) Paschen curve. A primary goal aims at establishing a quantitative triboelectric series [38]–[40] that predicts the amount of charge transfer between any two materials under given conditions, which has conventionally been generated qualitatively by detecting the relative polarity between each contact pair which can be successfully done in air. A recent attempt [28] quantified the charge transfer of various materials against a fixed reference chosen as mercury (liquid) which guarantees the intimacy of contacts, and a similar investigation can be done with the presented test apparatus using any material as reference. The quantitative triboelectric series benefits not only applications utilizing triboelectric surface charge (Chapter 4) but more importantly the understanding of the mechanism of contact electrification and identification of the charge carriers. While it is widely accepted that contact charging between metals is primarily due to electron transfer dominated by difference in the work function of the dissimilar surfaces [2], the charge carriers

in contact electrification involving dielectric/insulator surfaces are still under debate among theories on potential electron [27], ion [41]–[43] and massive material transfer [44], [45].

The test apparatus presented in Figure 2.6 is directly applied for investigations of raw post-contact surface charge densities, with the modification that the bottom load cell (1 N capacity, 0.5 mN resolution) is removed so that the top load cell (25 N capacity, 0.1 N resolution) measures all forces including compression during contacts, adhesion (sticking) during separation and Coulomb force after separation. The same top sample (PDMS, 95 mm diameter) is used while the size of bottom samples is reduced to 44.5 mm (1.75 in) in diameter to ensure that contact forces within the capacity of the load cell are sufficient for the saturation of surface charge, as discussed in Figure 2.5. The samples are lifted to a large gap (20 mm) under atmospheric pressure before each set of test runs, and the chamber is then pumped to vacuum (below 0.1 Torr) where the load cell is zeroed, during which the majority of any residual surface charge is dissipated by air breakdown. The samples then simply undergo a series of contact cycles with a controlled peak compression force, as demonstrated in Figure 3.1. In the separation stage a nontrivial displacement of the top sample is required to overcome the adhesion (sticking force) by strains in the bulk PDMS elastomer (state 4 in Figure 3.1) while the maximum gap distance after the surfaces physically detach is ensured to not trigger any breakdown of the air in between. The Coulomb force measured immediately before the surfaces engage in each cycle (state 2 in Figure 3.1) is extracted to represent the real-time accumulation of surface charge, for which the infinite-parallel-plate assumption is valid so that $|F_{\text{Coulomb}}| = \dfrac{\pi R^2 \bar{\sigma}^2}{2\varepsilon_{\text{air}}}$ and the derivation using Equation 2.2 is unnecessary.

3.2 Results and Discussions

The following illustrates contact electrification tests with confidence of eliminated breakdown discharge, which, as expected, reflect significantly higher surface charge densities than those limited by air breakdown as observed in Section 2.3.2. However, inconsistencies in repeated test results as to be discussed have impeded the establishment of a qualitative triboelectric series which requires refinement of multiple other test conditions except air pressure and gap distance.

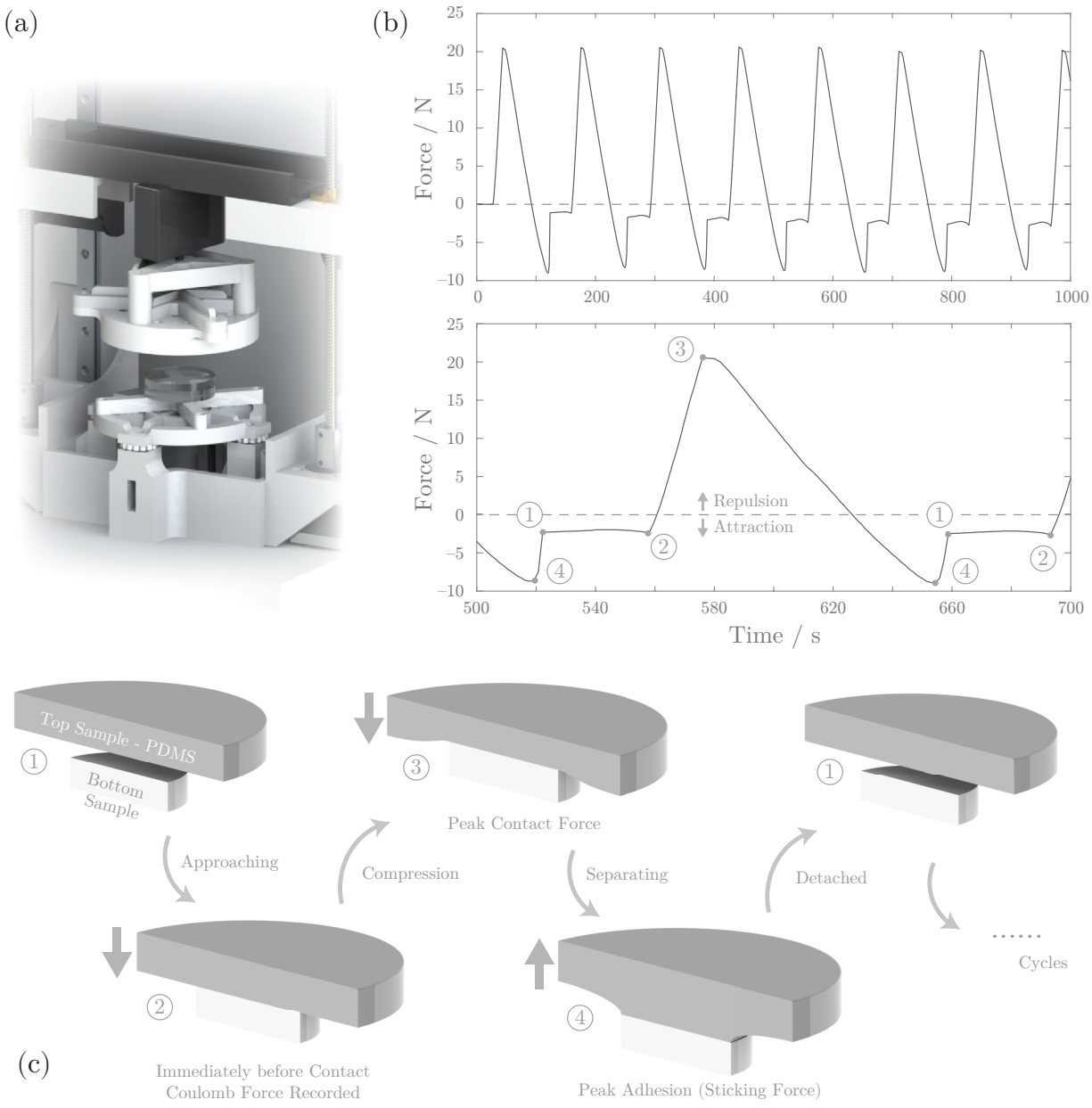

Figure 3.1. Test apparatus and strategies for investigation of raw surface charge transfer: a) Modified test apparatus with bottom load cell removed and bottom sample size reduced. b) Time histories of load cell readings in a typical test run of contact electrification cycles during which discharge by air breakdown is eliminated by limiting air pressure and maximum gap distance, where measurements of compression, adhesion and Coulomb forces are labeled at different test stages explained in (c).

3.2.1 Charge Accumulation in Multiple Contact Pairs

The test strategies described in Section 3.1 is applied to investigate the raw amount of charge transfer in contact electrification of PDMS against a series of materials. The real-time force measurements for a PDMS-ABS contact pair during 60 compression cycles with a peak force of 20 N (10.1 kPa) are recorded and shown in Figure 3.2a and the corresponding average surface charge density after each contact cycle is shown in Figure 3.2b. A rapid saturation to a high level of 200 $\mu C/m^2$ is observed. The surfaces are discharged at the end of the test by bringing the surfaces to a sufficient gap distance that triggers air breakdown, which is verified by a zero Coulomb force measurement when they approach each other again. The test is then repeated under same conditions, as shown in Figure 3.2c, where charge accumulates at a slower rate but converges to a similar saturation level. Same test runs are performed on two other polymer samples, Nylon and PLA, as well as a conductive copper sample, results of which are shown in Figure 3.3. In all cases the surface charge density saturates to similar levels with slight deviations which is attributed to the initial surface conditions before the first test run. Meanwhile, the sticking force measured in the separation phase of each contact cycle (e.g., Figure 3.2a) is both significantly larger than and also increasing with the maximum Coulomb attraction immediately before contacts, indicating that Coulomb force is not the dominant factor of the surface adhesion where a more significant contribution is made by intermolecular forces. It is also preliminarily concluded that comparatively hydrophobic polymer surfaces such as PTFE and PLA tend to build less surface charge under higher relative humidity, while comparatively hygroscopic polymer surfaces such as ABS and Nylon, as well as the conductive copper sample (which appears porous according to the SEM image), are more consistent. The explanation can conceptually be that the water (vapor) molecules at the interface are absorbed into hygroscopic surfaces under compression while remaining between the hydrophobic ones to impede either their physical contact or the charging. Moreover, it is also concluded that transient effects or charge backflow may exist in the accumulation of surface charge since it is observed that if the compression stage in a contact cycle is held longer than others then the next Coulomb force measurement typically shows a decrease.

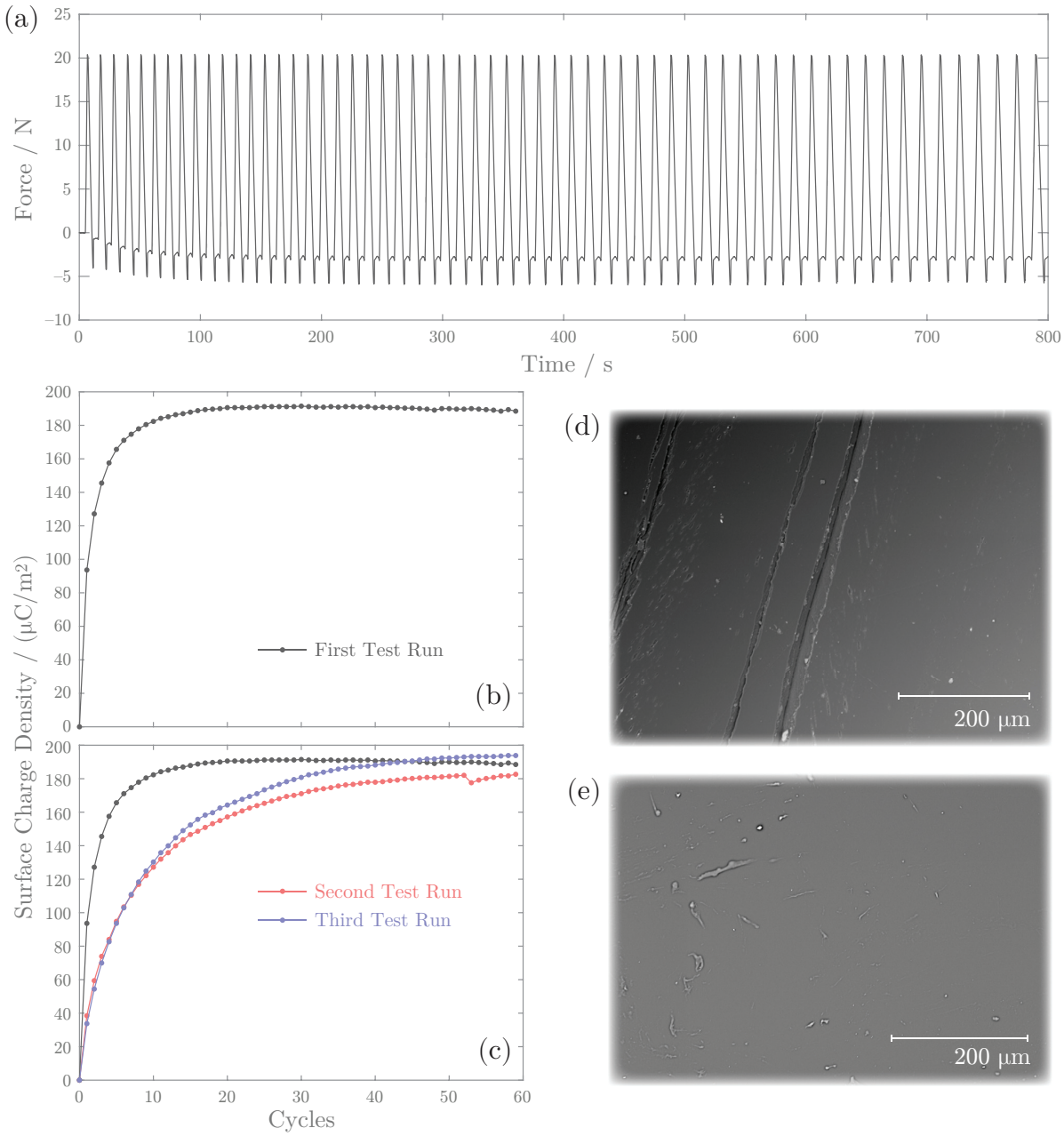

Figure 3.2. Surface charge accumulation in PDMS-ABS contact electrification cycles: a) Time history of force measurements (positive for repulsion) which yield b) the real-time average surface charge density after each contact cycle. c) Three consecutive test runs where the surfaces are discharged by air breakdown at the end of each, and SEM images of d) the ABS and e) PDMS surfaces.

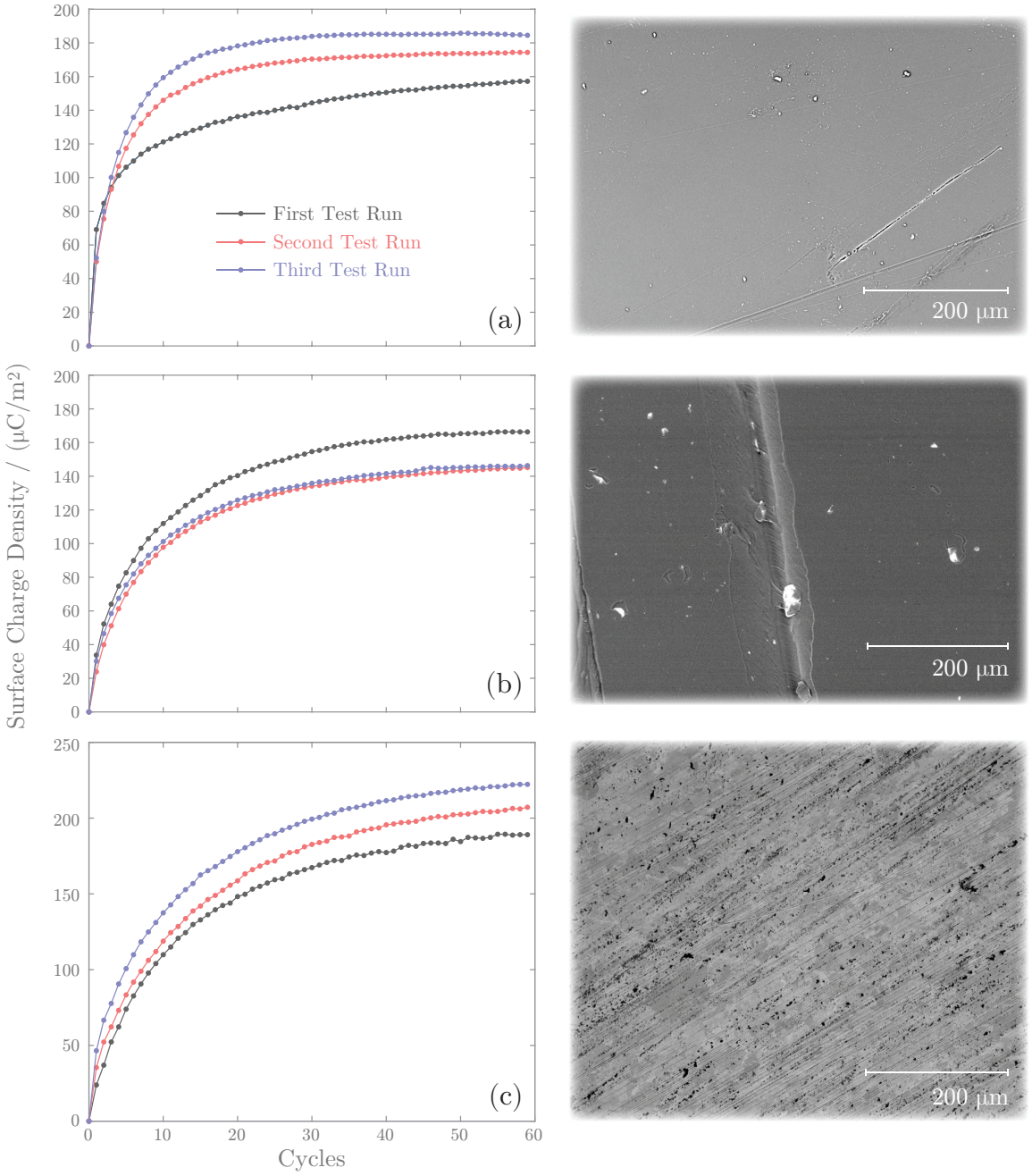

Figure 3.3. Surface charge accumulation for multiple material combinations: Real-time surface charge density measurements in three consecutive test runs of contact electrification cycles using a) PDMS-Nylon, b) PDMS-PLA and c) PDMS-copper contact pairs and SEM images of the Nylon, PLA and copper samples, respectively.

3.2.2 Observations of Post-Discharge Surface Alternation

The same test procedure is repeated on a PDMS-PTFE contact pair, as shown in Figure 3.4a, which exhibits both a comparatively lower saturated surface charge density and a significantly reduced saturation level in repeated tests after the surfaces are discharged. The SEM (Phenom ProX) images of the PTFE sample after the tests show an alteration of the surface textures, as shown in Figure 3.4c. The explanation that this is purely caused by contacts against the PDMS surface is excluded since it has been observed only in PTFE samples that are charged to a sufficient level (over 50 $\mu C/m^2$) and then discharged in low air pressure (below 0.1 Torr), but not in samples that undergo similar contact cycles while discharged under higher air pressure. This explains why results of PTFE electrification remained consistent for preliminary tests conducted in air as in Section 2.3.2. The PTFE surface alternation is preliminarily attributed to the strike of cations from Townsend avalanches during the breakdown discharge process, based on observations of PTFE surface degradation as in Figure A.2. It is found that under high SEM magnifications or currents the electron beams with energies between 5 keV and 15 keV are capable of knocking out secondary electrons from the PTFE surface at high rates that break its chemical bonds. Meanwhile, the observed damage pattern of Au-Pd-coated PTFE surface (Figure A.2d) excludes the possibility that the surface textures in Figure 3.4c are due to exposure to electron beams in the SEM instead of the contact electrification tests. It is concluded that the post-discharge surface textures displayed characteristics similar to early stages of uncoated and carbon-coated PTFE degradation under SEM electron beams (Figure A.2), where the energy of the cations that strike the PTFE surfaces during the discharge can be estimated to show that it is comparable to that of the SEM. A brief estimation assuming a surface charge density of 50 $\mu C/m^2$ which triggers an initial air breakdown incident typically at gap distances higher than 3 mm under an air pressure lower than 0.1 Torr will generate a gap voltage higher than 17 kV. Meanwhile the mean free path for air at 0.1 Torr is around 0.5 mm (assuming nitrogen) so that the electrons and cations generated in Townsend avalanches may only experience several collisions with air molecules when they are accelerated across the gap and therefore it is reasonable to estimate that a significant portion of the particles that strike the PDMS and PTFE surfaces

have obtained energies higher than 10 keV, especially given that the above assumptions are conservative in that the surface charge densities observed in the tests are typically higher than 50 µC/m^2 while the air pressure in the vacuum chamber is typically below 0.05 Torr when the surfaces are discharged. Although the breakdown discharge is an instantaneous process compared to continuous electron beams, the surge of current equal to the majority of the surface charge divided by the duration of the discharge can be high enough to cause degradation of the PTFE surfaces in the same way that the electron beams do in the SEM. It is further assumed that such alternation of the PTFE surface causes the reduction of surface charge accumulation in following contact electrification cycles, the reason of which remains to be investigated. This prevents the observation of potential further surface damage stages since the lower surface charge densities may not accelerate particles in Townsend avalanches to the same high energies as in the first test run. The post-discharge surface alternation is not observed in the PDMS surfaces, although particles accelerated to the same energy level also strike it during the breakdown discharge, which can be attributed to that PTFE is more prone to degradation under electron/cation beams as shown in Figure A.2 where the PDMS surface exhibits only charging instead of visible damage even after high-intensity EDS tests.

The high surface charge densities measured here for contact electrification in vacuum implies the potential improvement of devices utilizing triboelectric charge by avoiding air breakdown in their designs. This is illustrated in Chapter 4 with the typical application of triboelectric energy harvesters.

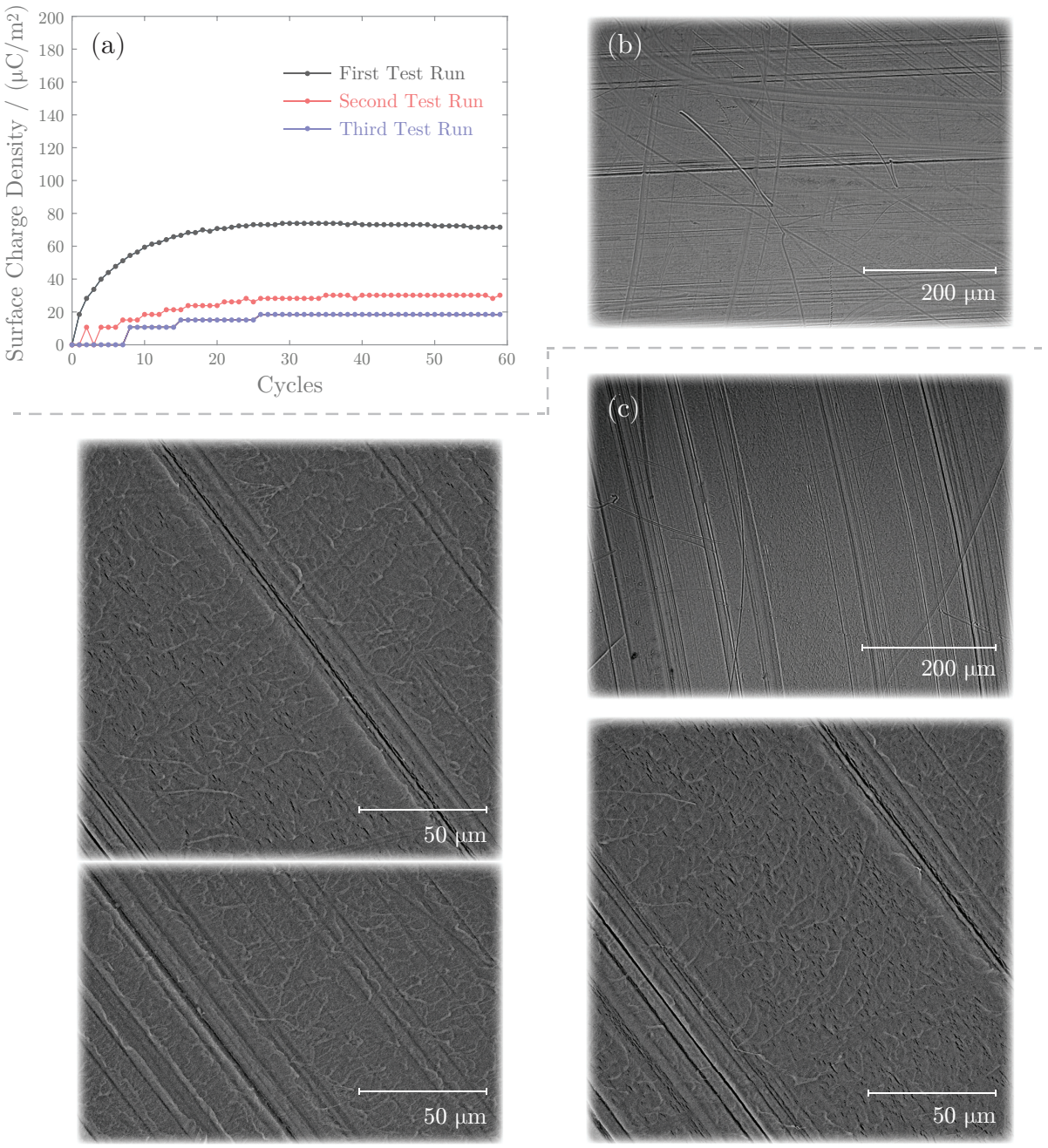

Figure 3.4. Charge accumulation and potential surface damage for PDMS-PTFE contact electrification: a) Real-time surface charge density measurements in three consecutive test runs. b) SEM image of the PTFE sample prior to the tests. c) SEM images of the PTFE sample after the tests, with a layer of Au-Pd coating.

4. MODELING TRIBOELECTRIC ENERGY HARVESTERS

Experimental quantification of both raw surface charge transfer and dissipation by air breakdown in general contact electrification sees direct practice in the recent research interest of triboelectric energy harvesters, which is introduced in Section 4.1 as an outstanding strategy of vibro-impact energy harvesting and then illustrated with an application in Section 4.3.

4.1 Introduction on Vibro-Impact Triboelectric Energy Harvesting

Energy harvesters are generators that convert excessive energy from ambient excitations into electricity to either directly power units in the same system or be stored for later use, studies of which have emerged in recent years exploring their applications in self-powered devices where batteries are not desired. Among various strategies that have been exploited for different sources, vibratory energy harvesters stand as a popular design that generate electricity from mechanical vibrations. The efficiency of vibratory energy harvesters is typically related to their response to the rich frequency components in ambient excitations and while a linear system is only efficient at discrete resonant frequencies, its functional bandwidth can be expanded by integrating nonlinearities into the system, a detailed illustration of which can be found in [46] and is briefly adapted as follows. Consider, in the simplest case, a 1-degree-of-freedom vibratory energy harvester in which the mechanical subsystem is modeled as a proof mass m (with displacement x_s from equilibrium) attached onto a host system (base) through linear stiffness (spring constant k) and damping (coefficient c) elements, as shown in Figure 4.1. Let the base be substantial and thus neglect feedback from the proof mass, so that its motion can be prescribed as an input displacement x_b. Along with the linear couplings, let there be a general nonlinear restoring force $f_\mathrm{NL}(x_\mathrm{s} - x_\mathrm{b})$ between the masses, yielding the equation of motion for the mechanical subsystem

$$m\ddot{x}_\mathrm{s} + c(\dot{x}_\mathrm{s} - \dot{x}_\mathrm{b}) + k(x_\mathrm{s} - x_\mathrm{b}) + f_\mathrm{NL}(x_\mathrm{s} - x_\mathrm{b}) = 0 \ . \tag{4.1}$$

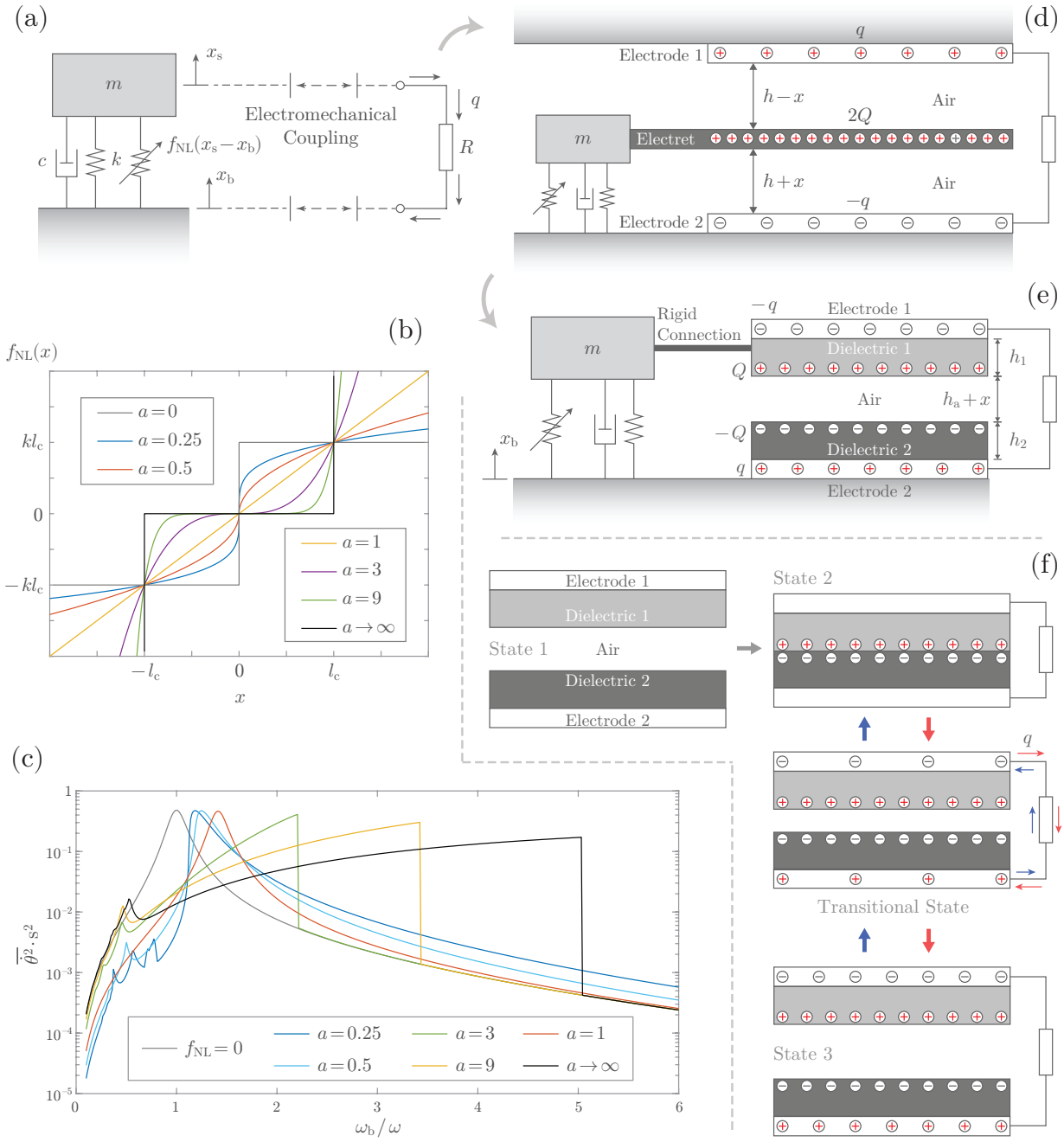

Figure 4.1. Theoretical model of triboelectric generators as vibro-impact energy harvesters: a) Schematics of a general vibratory energy harvester. b) A family of nonlinear restoring forces and c) the corresponding simulated output power of a simple electret-based energy harvester (d) with respect to excitation frequency. e) A vertical contact triboelectric generator and f) mechanism of its electromechanical coupling.

Define the relative displacement $x = x_\mathrm{s} - x_\mathrm{b}$ and rewrite Equation 4.1 as

$$m\ddot{x} + c\dot{x} + kx + f_\mathrm{NL}(x) = -m\ddot{x}_\mathrm{b} \ . \tag{4.2}$$

Energy harvesting is fulfilled via electromechanical coupling methods such as piezoelectric, electromagnetic and electrostatic mechanisms, i.e., the current $\dot{q}$ running through a general external load R is driven by motions in the mechanical system. Assume temporarily, for simplicity of demonstration, an asymmetric coupling so that $\dot{q} = f_\mathrm{EM}(q, x, \dot{x}, R)$ but the mechanical equations of motion (4.2) remains unaffected. Let f_EM be a simple electrostatic coupling expressed as

$$\dot{q} = f_\mathrm{EM}(q, x, \dot{x}, R) = -\frac{2}{\varepsilon A R}\left(hq + Qx\right) \ . \tag{4.3}$$

While this form is for demonstrative purposes only, physically it represents an electret-based vibratory energy harvester, as shown in Figure 4.1d. Let a thin planar rigid electret polarized with uniformly distributed charge $2Q$ follow the motion of the proof mass. Fix two identical rigid planar electrodes on base and let them be symmetric about the electret with clearance h at equilibrium. Connect the electrodes with external load R and assume charge conservation in the circuit so that the electrodes possess equal amount of charge with opposite signs ($\pm q$). Equation 4.3 then describes the induced current in the circuit, where ε is the permittivity of air and A is the surface area of both the electret and the electrodes.

Consider a family of nonlinear couplings defined as odd functions

$$f_\mathrm{NL}(x) = \mathrm{sgn}(x) \cdot k_\mathrm{NL} \left|x\right|^a \equiv \mathrm{sgn}(x) \cdot k l_\mathrm{c} \left|\frac{x}{l_\mathrm{c}}\right|^a , \ a \in \mathbb{R}_{\geq 0} \ , \tag{4.4}$$

where a characteristic length l_c is adopted to replace the conventional nonlinear stiffness k_NL. Note that k is the previously defined linear stiffness constant, and a is allowed non-integer values which are not necessarily trivial [47]. Members in this family with selected values of a are plotted in Figure 4.1b, those of which with $a > 1$ and $0 < a < 1$ exhibit hardening and softening natures, respectively. Special members include: $a = 1$ which is equivalent to paralleling a duplicate of the linear spring, $a = 0$ where the coupling is a step function

analogous to a fictional discontinuous field, and $a \to \infty$ where a rigid impact is approached, as will be discussed soon.

The energy harvester system described by Equations 4.2, 4.3 and 4.4 is briefly studied in the following to illustrate the benefits of structural nonlinearities f_{NL} in improving the energy-harvesting bandwidth. Partially nondimensionalize the equation of motion into

$$\begin{cases} \ddot{\xi} + 2\zeta\omega\dot{\xi} + \omega^2 \left[\xi + \operatorname{sgn}(\xi) \cdot |\xi|^a\right] = F_{\mathrm{b}} \triangleq -\dfrac{\ddot{x}_{\mathrm{b}}}{l_{\mathrm{c}}} \\ \dot{\theta} + \dfrac{1}{\tau_q}\left(\xi_h \theta + \xi\right) = 0 \end{cases} \tag{4.5}$$

where $\xi = \dfrac{x}{l_{\mathrm{c}}}$, $\theta = \dfrac{q}{Q}$, $\omega = \sqrt{\dfrac{k}{m}}$, $\zeta = \dfrac{c}{2\sqrt{mk}}$, $\tau_q = \dfrac{\varepsilon A R}{2 l_{\mathrm{c}}}$ and $\xi_h = \dfrac{h}{l_{\mathrm{c}}}$. Assign a harmonic base excitation $F_{\mathrm{b}} = \tilde{F}_{\mathrm{b}} \sin \omega_{\mathrm{b}} t$ and numerically simulate the system under fixed parameters $\omega = 1\,\mathrm{rad/s}$, $\zeta = 0.1$, $\tilde{F}_{\mathrm{b}} = 1$, $\tau_q = 1\,\mathrm{s}$ and $\xi_h = 5$ while sweeping the excitation frequency ω_{b} and varying exponent a, yielding the frequency response of nondimensional average steady-state output power $\overline{\dot{\theta}^2} \cdot \sec^2$ as shown in Figure 4.1c. Note that ω_{b} is only swept one-way from low to high, and that the parameter set guarantees $|\xi| < \xi_h$ so that motion of the electret is constrained between the electrodes.

It is clear that while softening restoring forces ($0 < a < 1$ in family 4.4) slightly affected the spectrum, hardening couplings ($a > 1$) significantly broadened the resonant bandwidth which in fact increased with a. It is thus natural to propose the introduction of such hardening nonlinearities into general energy harvester designs beyond the rather simplified case studied in this section. Specially, the extreme case $a \to \infty$ in the family of hardening nonlinearities has exhibited the best resonance bandwidth, as inferred from Figure 4.1c. Like aforementioned, it also has a comparatively clear physical interpretation as a pair of rigid walls on the base that symmetrically limit the displacement of the proof mass, where the characteristic length l_{c} directly measures the clearance. In other words the nonlinear coupling $f_{\mathrm{NL}}(x)|_{a\to\infty}$ is equivalent to the conservative rigid impact constraint, i.e., $\dot{x}^+ = -\dot{x}^-$ whenever $|x| \geq l_{\mathrm{c}}$, an informal proof of which can be synthesized from [48] and [49]. This implies that while nonlinearities in continuous forms (such as $f_{\mathrm{NL}}(x)$ with $0 < a < \infty$) may be difficult to find physical counterparts for implementation, it is efficient to start energy har-

vester designs with models involving impact pairs. (In fact, the infinite-square-well potential corresponding to rigid impacts is often of equal significance with the quadratic one corresponding to a harmonic oscillator, both in quantum [50] and classical mechanics [51], [52].) Note that while a conservative rigid impact corresponds to $c_r = 1$ in the stereo-mechanical impact law $\dot{x}^+ = -c_r \dot{x}^-$ where c_r is called the restitution coefficient [53]–[55], variations in modeling conservative mechanical impacts also exist in elastic forms such as bilinear [48], [56]–[58] and Hertzian [59], [60], defined as (recalling Equation 4.2)

$$f_{NL}(x) = \begin{cases} \text{sgn}(x) k_c \left| x - l_c \right|^b & , |x| \geq l_c \\ 0 & , \text{otherwise} \end{cases}, \text{ where } b = \begin{cases} 1 & , \text{Bilinear} \\ 1.5 & , \text{Hertzian} \end{cases}. \tag{4.6}$$

Clearly when $k_c \gg k$ (i.e., the stiffness of contact is strong compared to the linear structural stiffness during impact-free travels) both models converge to rigid impacts, thus retaining the feature of broad resonance bandwidth desired for energy harvesting. In addition, the behavior of vibro-impact energy harvesters is further investigated in Section 4.2 by analyzing the energy-frequency dependence of a multi-degree-of-freedom vibro-impact oscillator.

The choice of electromechanical coupling strategy is critical in energy harvester designs. While the addition of energy conversion elements inevitably reshapes the original mechanical subsystem, e.g., a piezoelectric patch attached to a beam changes its stiffness, the triboelectric mechanism possesses the intrinsic vibro-impact nonlinearity desired as proposed above. Triboelectric energy harvesters, which are more often called triboelectric generators [61], [62], are essentially electret-based generators that operate with electrostatic induction. However, they differ from the system described in Figure 4.1d in that instead of using an electret with permanent or semi-permanent distributed charge, a triboelectric generator builds comparatively transient electrets by depositing charge on dielectric surfaces using contact electrification. Figure 4.1f illustrates a classic double-dielectric vertical-contact triboelectric generator composed of two electrodes covered with dissimilar dielectric layers with nontrivial thickness. In the initial state (state 1) all components are electrically neutral. When the dielectric layers come into contact under some excitation (state 2), contact electrification happens and charge is transferred between them. As they separate, charge accumulated on the dielectric

surfaces remains fixed while image charge is induced in the electrodes as a current flows across external load R (transitional state). The amount of charge flow maximizes with the gap distance (state 3) and the system acts like an AC power source if it's driven by mechanical excitations into cyclic motion between states 2 and 3, as indicated by red (forward) and blue (backward) directions. A triboelectric vibro-impact energy harvester can then be formalized by including the mechanical couplings, as shown in Figure 4.1f and will be discussed in Section 4.4.

Triboelectric generators became popular in the past decade as a novel, low-cost but efficient energy harvesting mechanism that is characterized by a high open-circuit output voltage. Despite the aforementioned double-dielectric vertical contact mode, they may also operate with a single dielectric, as well as in other modes such as sliding [63] or even direct charge flow via air breakdown [64], as long as a combination of contact electrification and electrostatic induction is employed. Given the ubiquitous nature of triboelectricity, a vast range of materials are available for their designs, among which flexible and stretchable candidates have greatly broadened their applications to cover fields such as wearable electronics and soft robots [65], [66]. As a detailed illustration for principles and features of triboelectric energy harvesting, a side project on an application of such flexible vertical-contact generator is presented in Section 4.3.

4.2 Frequency-Energy Dependence of Vibro-Impact Oscillators

The behaviors of energy-harvesters involving nonlinear restoring forces in the family 4.4 are further studied by applying the method of numerical continuation to reveal the underlying mechanism of shifted frequency responses.

4.2.1 Method of Numerical Continuation

The nonlinearity-enhanced energy-harvesting bandwidth exhibited in Figure 4.1 is obtained with a one-way simulation sweep from low to high frequencies. A backward sweep from high to low frequencies, however, usually yields a different spectrum where the attenuated response does not shift back to the resonant one until a frequency much lower than

where it previously dropped downwards, as shown in Figure 4.2a. This essentially reveals a coexistence of attractors and efforts are required for energy harvesters to stay on the resonant one. The phenomenon can be further investigated by applying the numerical continuation method which solves branches of periodic solutions of nonlinear dynamical systems using the Newton-Raphson method and is capable of revealing unstable solutions such as the hidden branch shown in Figure 4.2a that connects the coexistent attractors via two saddle-nodes.

The numerical continuation scheme considers the general state-space dynamical system

$$\dot{\boldsymbol{z}} = \boldsymbol{f}\left(\boldsymbol{z}, t, \theta\right) \tag{4.7}$$

where $\boldsymbol{z}$ is the vector of motion states, t time and θ a parameter of interest. The system can be non-smooth in that it not only allows piecewise-defined functions $\boldsymbol{f}$ but is also subject to discontinuities in the form of instantaneous transformations

$$\boldsymbol{z}^{+} = \boldsymbol{g}\left(\boldsymbol{z}^{-}\right), \text{ if } p\left(\boldsymbol{z}\right) = 0 \tag{4.8}$$

where the superscripts $+$ and $-$ indicate states after and before meeting the condition p, respectively. Define solution space $\boldsymbol{s} = \left[\boldsymbol{z}_0^{\mathrm{T}}\ \boldsymbol{\tau}^{\mathrm{T}}\ \theta\right]^{\mathrm{T}}$ where $\boldsymbol{z}_0$ are motion states right after a certain discontinuity at $t_0 = 0$, while assuming the orbit contains N discontinuities, let $\boldsymbol{\tau} = \left[\tau_1\ \tau_2 \ldots \tau_N\right]^{\mathrm{T}}$ be the time interval between each so that $\tau_k = t_k - t_{k-1}$, where t_j, $j = 0, 1, ..., N$ are instants of the discontinuities and define $\boldsymbol{z}_k = \boldsymbol{z}^{+}\left(t_k\right)$. Define target equations $\boldsymbol{F}(\boldsymbol{s}) = \left[\boldsymbol{F}_z^{\mathrm{T}}\ \boldsymbol{F}_p^{\mathrm{T}}\right]^{\mathrm{T}} = \boldsymbol{0}$, where $\boldsymbol{F}_z = \boldsymbol{z}_N - \boldsymbol{z}_0$ and $\boldsymbol{F}_p = \left[p_1\ p_2 \ldots p_N\right]^{\mathrm{T}}$ in which $p_i\left(\boldsymbol{z}_{i-1}\right)$ is the presumed condition of discontinuity met at the ith instant. It has the Jacobian matrix

$$\boldsymbol{J}(\boldsymbol{s}) = \frac{\mathrm{d}\boldsymbol{F}}{\mathrm{d}\boldsymbol{s}} = \begin{bmatrix} \dfrac{\mathrm{d}\boldsymbol{F}_z}{\mathrm{d}\boldsymbol{z}_0} & \dfrac{\mathrm{d}\boldsymbol{F}_z}{\mathrm{d}\boldsymbol{\tau}} & \dfrac{\mathrm{d}\boldsymbol{F}_z}{\mathrm{d}\theta} \\ \dfrac{\mathrm{d}\boldsymbol{F}_p}{\mathrm{d}\boldsymbol{z}_0} & \dfrac{\mathrm{d}\boldsymbol{F}_p}{\mathrm{d}\boldsymbol{\tau}} & \dfrac{\mathrm{d}\boldsymbol{F}_p}{\mathrm{d}\theta} \end{bmatrix} \tag{4.9}$$

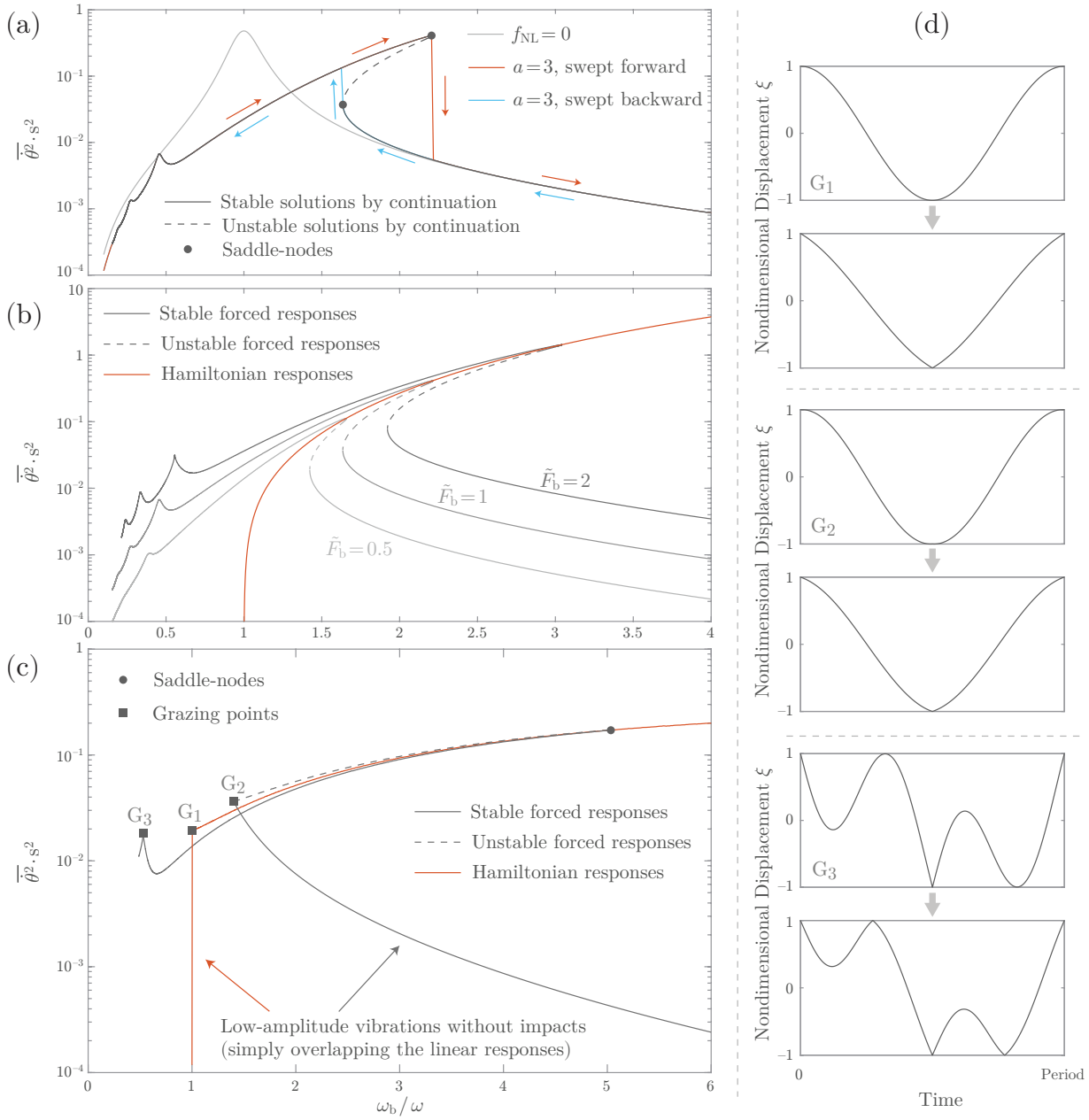

Figure 4.2. Numerical continuation on nondimensional power output of an electret-based energy harvester (Equation 4.5): a) Forced and b) Hamiltonian frequency responses assuming a cubic restoring force compared to revisited results from Figure 4.1c. c) Forced ($\tilde{F}_b = 1$) and Hamiltonian responses assuming stereo-mechanical impacts with d) time histories illustrating labeled grazing bifurcations.

which can be evaluated as follows. Consider, the mapping from $\boldsymbol{z}_{k-1}$ to $\boldsymbol{z}_k$ between time instants t_{k-1} and t_k and denote $t^* = t - t_{k-1}$ so that in this time interval there is

$$\boldsymbol{z} = \boldsymbol{z}\left(\boldsymbol{z}_{k-1}, \tau_1, ..., \tau_{k-1}, \theta, t^*\right) \tag{4.10}$$

which gives

$$\boldsymbol{z}_k = \boldsymbol{g}_k\left(\boldsymbol{z}^-\left(\boldsymbol{z}_{k-1}, \tau_1, ..., \tau_{k-1}, \theta, \tau_k\right)\right) \triangleq \boldsymbol{h}_k\left(\boldsymbol{z}_{k-1}, \tau_1, ..., \tau_k, \theta\right) \tag{4.11}$$

which introduces local Jacobian matrices $\dfrac{\mathrm{d}\boldsymbol{h}_k}{\mathrm{d}\boldsymbol{z}_{k-1}}$, $\dfrac{\mathrm{d}\boldsymbol{h}_k}{\mathrm{d}\boldsymbol{\tau}}$ and $\dfrac{\mathrm{d}\boldsymbol{h}_k}{\mathrm{d}\theta}$. To solve $\dfrac{\mathrm{d}\boldsymbol{h}_k}{\mathrm{d}\boldsymbol{z}_{k-1}} = \dfrac{\mathrm{d}\boldsymbol{g}_k}{\mathrm{d}\boldsymbol{z}_k^-}\dfrac{\mathrm{d}\boldsymbol{z}_k^-}{\mathrm{d}\boldsymbol{z}_{k-1}}$, where $\boldsymbol{z}_k^- = \boldsymbol{z}^-\left(\boldsymbol{z}_{k-1}, \tau_1, ..., \tau_{k-1}, \theta, \tau_k\right)$, define $\boldsymbol{D}_z = \dfrac{\mathrm{d}\boldsymbol{z}}{\mathrm{d}\boldsymbol{z}_{k-1}}$ so that

$$\frac{\mathrm{d}\boldsymbol{D}_z}{\mathrm{d}t^*} = \frac{\mathrm{d}\dot{\boldsymbol{z}}}{\mathrm{d}\boldsymbol{z}_{k-1}} = \frac{\partial\dot{\boldsymbol{z}}}{\partial\boldsymbol{z}}\boldsymbol{D}_z,\ \boldsymbol{D}_z\left(0\right) = \boldsymbol{I}\,, \tag{4.12}$$

and then $\dfrac{\mathrm{d}\boldsymbol{h}_k}{\mathrm{d}\boldsymbol{z}_{k-1}}$ can be obtained by integrating $\boldsymbol{D}_z$ along with $\boldsymbol{z}$ from $t^* = 0$ to $t^* = \tau_k$. Meanwhile, to solve $\dfrac{\mathrm{d}\boldsymbol{h}_k}{\mathrm{d}\tau_j} = \dfrac{\mathrm{d}\boldsymbol{g}_k}{\mathrm{d}\boldsymbol{z}_k^-}\dfrac{\mathrm{d}\boldsymbol{z}_k^-}{\mathrm{d}\tau_j}$, $j = 1, 2, ..., k-1$, define $\boldsymbol{D}_j = \dfrac{\mathrm{d}\boldsymbol{z}}{\mathrm{d}\tau_j}$ so that

$$\frac{\mathrm{d}\boldsymbol{D}_j}{\mathrm{d}t^*} = \frac{\mathrm{d}\dot{\boldsymbol{z}}}{\mathrm{d}\tau_j} = \frac{\partial\dot{\boldsymbol{z}}}{\partial\boldsymbol{z}}\boldsymbol{D}_j + \frac{\partial\dot{\boldsymbol{z}}}{\partial\tau_j},\ \boldsymbol{D}_j\left(0\right) = \boldsymbol{0}\,, \tag{4.13}$$

and then integrate in a similar way. At the same time, $\dfrac{\mathrm{d}\boldsymbol{h}_k}{\mathrm{d}\theta} = \dfrac{\mathrm{d}\boldsymbol{g}_k}{\mathrm{d}\boldsymbol{z}_k^-}\dfrac{\mathrm{d}\boldsymbol{z}_k^-}{\mathrm{d}\theta}$ can be solved in a similar way, and finally, evaluate $\dfrac{\mathrm{d}\boldsymbol{h}_k}{\mathrm{d}\tau_k} = \dfrac{\mathrm{d}\boldsymbol{g}_k}{\mathrm{d}\boldsymbol{z}_k^-}\dot{\boldsymbol{z}}\left(\tau_k\right)$. The desired Jacobian matrix $\boldsymbol{J}(\boldsymbol{s})$ can then be obtained by successive assembly of the local ones through

$$\frac{\mathrm{d}\boldsymbol{z}_k}{\mathrm{d}\boldsymbol{z}_0} = \frac{\mathrm{d}\boldsymbol{h}_k}{\mathrm{d}\boldsymbol{z}_{k-1}}\frac{\mathrm{d}\boldsymbol{z}_{k-1}}{\mathrm{d}\boldsymbol{z}_0} \tag{4.14}$$

and

$$\frac{\mathrm{d}\boldsymbol{z}_k}{\mathrm{d}\theta} = \frac{\mathrm{d}\boldsymbol{h}_k}{\mathrm{d}\boldsymbol{z}_{k-1}}\frac{\mathrm{d}\boldsymbol{z}_{k-1}}{\mathrm{d}\theta} + \frac{\mathrm{d}\boldsymbol{h}_k}{\mathrm{d}\theta} \tag{4.15}$$

and

$$\frac{\mathrm{d}\boldsymbol{z}_k}{\mathrm{d}\boldsymbol{\tau}} = \frac{\mathrm{d}\boldsymbol{h}_k}{\mathrm{d}\boldsymbol{z}_{k-1}}\frac{\mathrm{d}\boldsymbol{z}_{k-1}}{\mathrm{d}\boldsymbol{\tau}} + \frac{\mathrm{d}\boldsymbol{h}_k}{\mathrm{d}\boldsymbol{\tau}}\,. \tag{4.16}$$

Given an initial guess $\boldsymbol{s}^{(0)}$, a solution of the target equation $\boldsymbol{F}(\boldsymbol{s}) = \boldsymbol{0}$ can be sought by applying the shooting method with iterations

$$\boldsymbol{s}^{(i+1)} = \boldsymbol{s}^{(i)} + \boldsymbol{\zeta},\ \boldsymbol{J}^*\left(\boldsymbol{s}^{(i)}\right)\boldsymbol{\zeta} = -\boldsymbol{F}^*\left(\boldsymbol{s}^{(i)}\right) \tag{4.17}$$

where $\boldsymbol{F}^*\left(\boldsymbol{s}^{(i)}\right) = \left[\boldsymbol{F}^{\mathrm{T}}\left(\boldsymbol{s}^{(i)}\right)\ \ 0\right]^{\mathrm{T}}$ and $\boldsymbol{J}^*\left(\boldsymbol{s}^{(i)}\right) = \left[\boldsymbol{J}^{\mathrm{T}}\left(\boldsymbol{s}^{(i)}\right)\ \ \boldsymbol{p}\right]^{\mathrm{T}}$ and $\boldsymbol{p}$ is a constant vector normal to the desired search direction. Branches of solutions of the target equation $\boldsymbol{F}(\boldsymbol{s}) = \boldsymbol{0}$ can then be tracked using the pseudo-arclength continuation method [67], [68] so that if $\boldsymbol{s}_j^{(i)}$ denotes the ith iteration in search of the jth solution point and $\boldsymbol{s}_j^*$ denotes the converged jth solution point, then the initial guess for the $(j+1)$th point is given by $\boldsymbol{s}_{j+1}^{(0)} = \boldsymbol{s}_j^* + \alpha\boldsymbol{p}_j$ where α is the step length and $\boldsymbol{p}_j$, which is the tangent vector at $\boldsymbol{s}_j^*$, lies in the null space of $\boldsymbol{J}\left(\boldsymbol{s}_j^*\right)$ and is assigned as the normal direction vector in $\boldsymbol{J}^*\left(\boldsymbol{s}_{j+1}^{(i)}\right)$ for all iterations $\boldsymbol{s}_{j+1}^{(i)}$.

The general continuation method can also solve the underlying Hamiltonian (conservative) system for a given nonlinear system with excitation and dissipation terms, for which numerical simulations typically will not converge to steady state since solutions are marginally stable and thus not attracting adjacent initial conditions. The solved periodic responses of the Hamiltonian system, also known as nonlinear normal modes, form a backbone branch that governs the frequency response of the original system under different excitation magnitudes, as shown in Figure 4.2b when applied to the electret-based harvester described by equations of motion 4.5. The piecewise algorithm designed to deal with discontinuities can also solve periodic responses of dynamical systems such as those with stereo-mechanical impacts corresponding to $a \to \infty$ in Equation 4.4, results of which are shown in Figure 4.2c. It can be interpreted that the smooth deviation of nonlinear normal modes from the underlying linear system (e.g., the bended backbone for a cubic nonlinearity as in Figure 4.2b) evolves into a non-smooth grazing transition (point G_1) where the energy in the mechanical system is high enough to hit the impact constraints. Similarly, the saddle-node bifurcation that occurs when sweeping the system with cubic nonlinearity from high to low frequencies

also evolves into such a grazing point G_2 while dynamics in the low frequency regions for systems with smooth nonlinearities may also find counterparts as more complicated grazing bifurcations (G_3) in the impacting system.

4.2.2 Frequency-Energy Plots of a 2-Degree-of-Freedom Vibro-Impact Oscillator

This section includes content from the publication: Hongcheng Tao and James Gibert. Periodic orbits of a conservative 2-dof vibro-impact system by piecewise continuation: Bifurcations and fractals. *Nonlinear dynamics*, vol. 95, no. 4, pp. 2963-2993, 2019. [49]

The performance of nonlinear energy harvesters can benefit from more degrees of freedoms favoring richer resonant behaviors to exploit. Consider the conservative 2-degree-of-freedom system with an internal nonlinear restoring force

$$\begin{cases} m_1\ddot{x}_1 + (k_1+k_2)\,x_1 - k_2x_2 = k_2\,|x_2-x_1|^a\,\mathrm{sgn}\,(x_2-x_1) \\ m_2\ddot{x}_2 - k_2x_1 + k_2x_2 = -k_2\,|x_2-x_1|^a\,\mathrm{sgn}\,(x_2-x_1) \end{cases} \tag{4.18}$$

where the displacements are normalized with a characteristic length which equals the gap distance in the vibro-impact limit $a \to \infty$. The system's periodic responses display a dependency of frequency on the energy (Hamiltonian) which if assuming a to be a positive odd integer is expressed as

$$H = \frac{1}{2}\left[m_1\dot{x}_1^2 + m_2\dot{x}_2^2 + k_1x_1^2 + k_2\,(x_1-x_2)^2\right] + \frac{k_2}{a+1}\,(x_2-x_1)^{a+1}\ . \tag{4.19}$$

The vibro-impact limit $a \to \infty$ of the system is studied using the numerical continuation scheme from Section 4.2.1 with parameters $m_1 = 2m_2 = 2\,\mathrm{kg}$, $k_1 = 8k_2 = 8\,\mathrm{N/m}$, which yields the frequency-energy plot of the periodic orbits as shown in Figure 4.3. With low energies the vibrations of the masses are simply linear and do not involve impacts so that the two backbones (nonlinear normal modes) start from the natural frequencies ω_1 and ω_2 of the linear subsystem. As the energy increases impacts are triggered at grazing solution points G_1 and G_2 as shown in Figure 4.4. The backbone starting from ω_2 extends to infinite

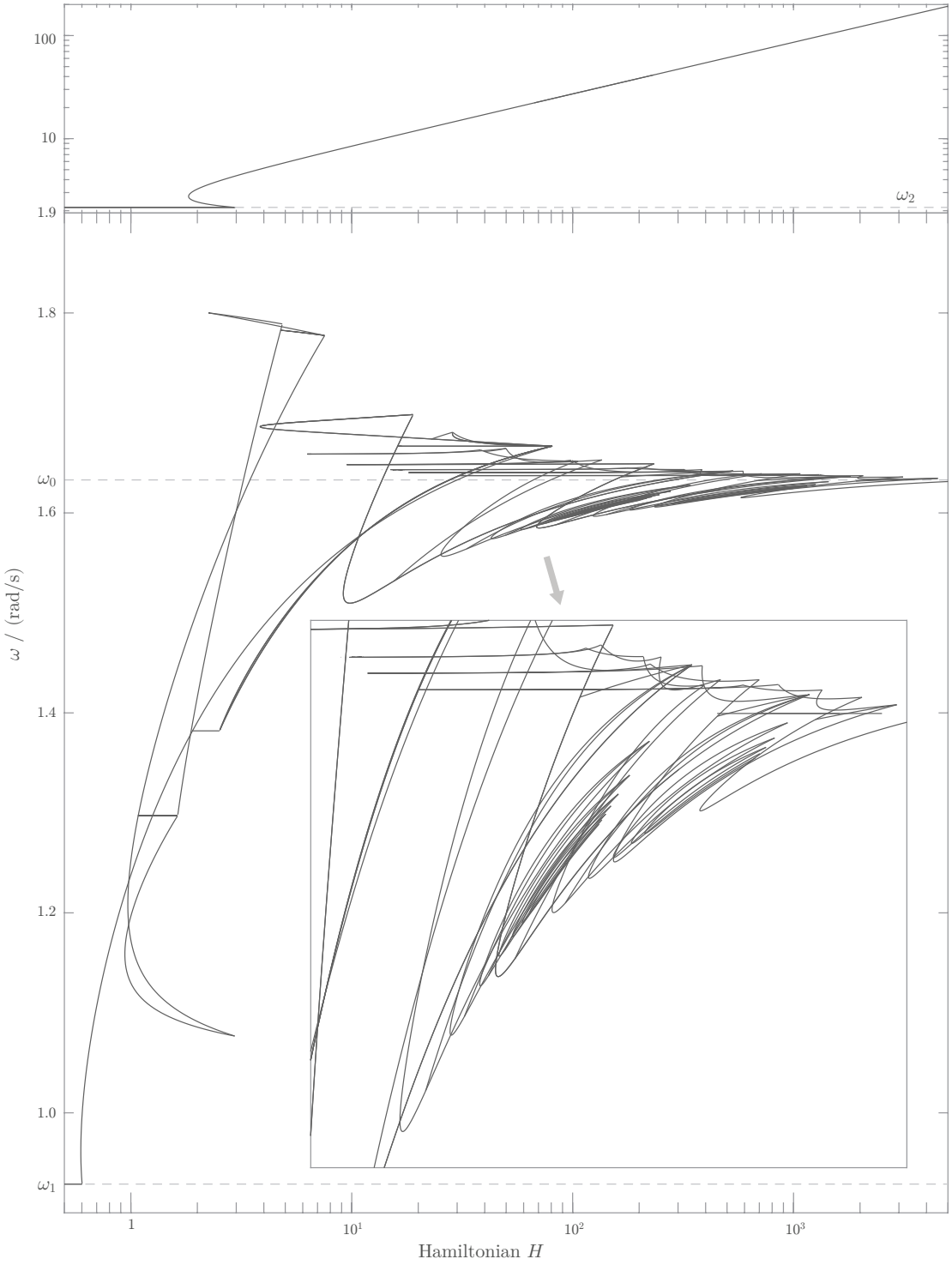

Figure 4.3. Partial frequency-energy plot of a 2-degree-of-freedom vibro-impact oscillator obtained by numerical continuation.

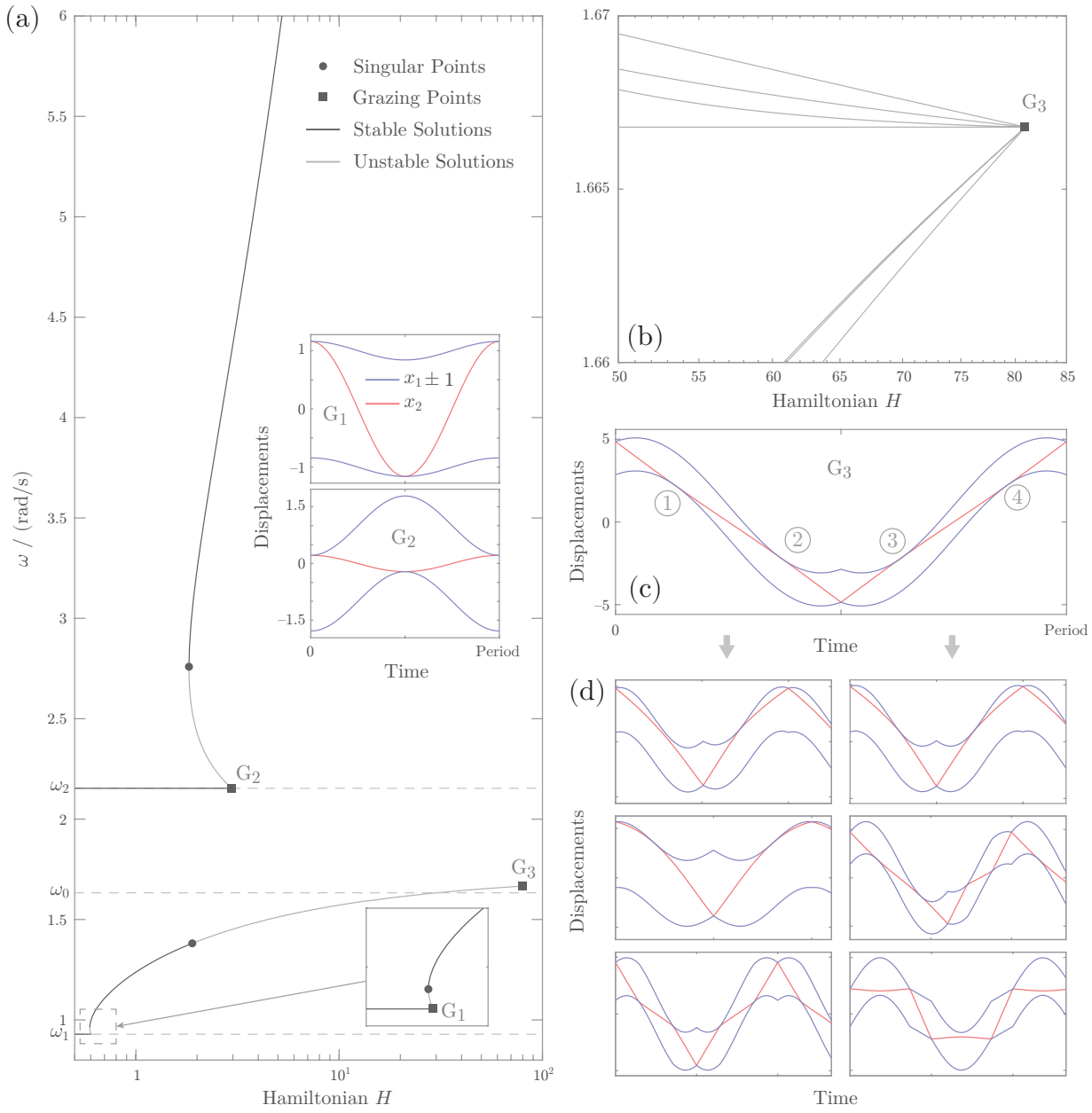

Figure 4.4. Grazing bifurcations in the initialization of the frequency-energy plot: a) Transition of the backbone branches from linear responses to simple vibro-impact responses. b) A complex grazing point encountered in the lower backbone with c) 4 grazing incidents which bifurcates into d) multiple solution branches turning selected grazing incidents into impacts.

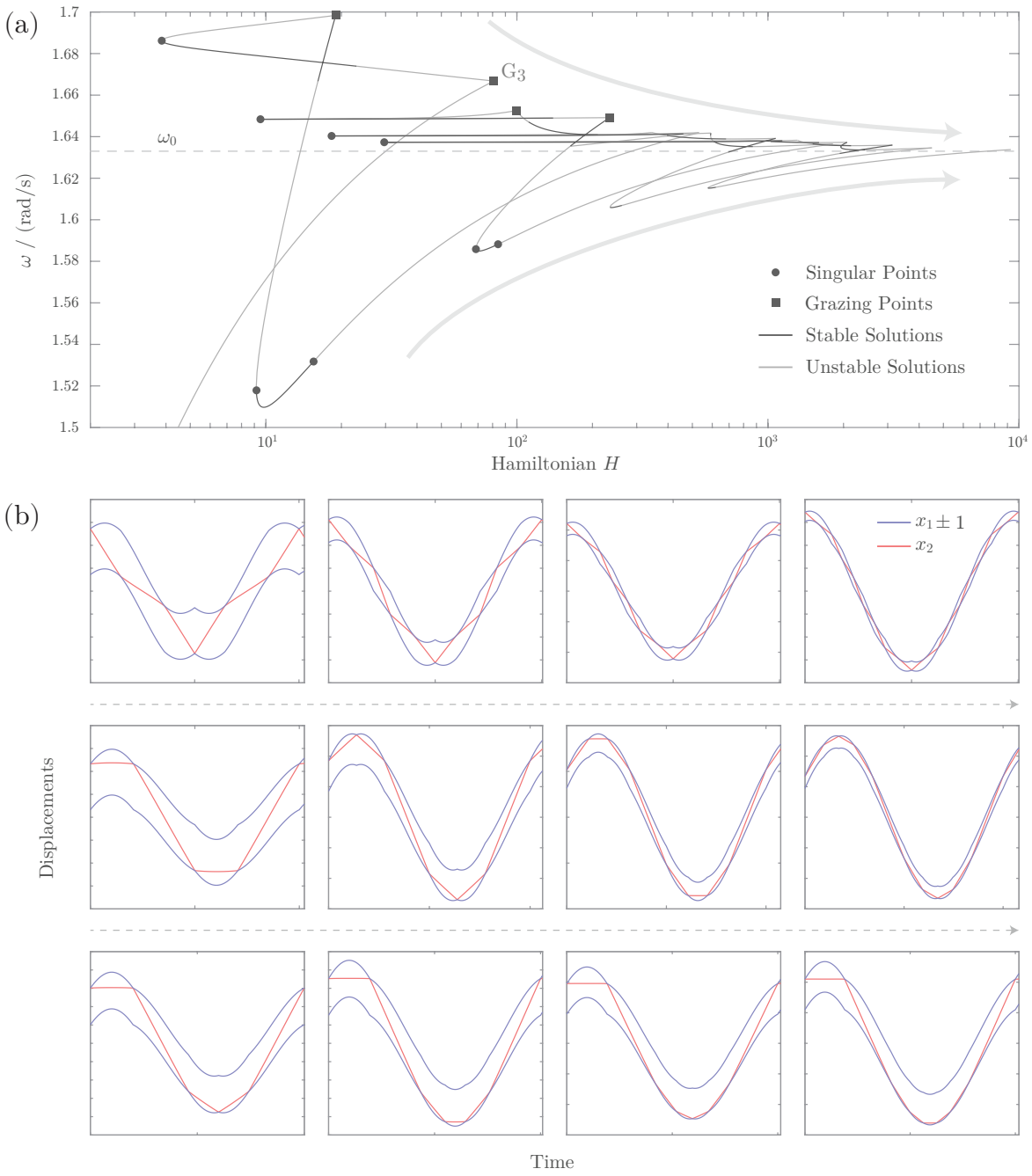

Figure 4.5. Convergence of the lower backbone branch to the natural frequency of an underlying 1-degree-of-freedom system: a) Convergence on the frequency-energy-plot. b) Time histories of selected solution points on the backbone branch (and asymmetric side tongues not shown on the frequency-energy plot) depicting chattering and sticking transitions to a 1-degree-of-freedom motion.

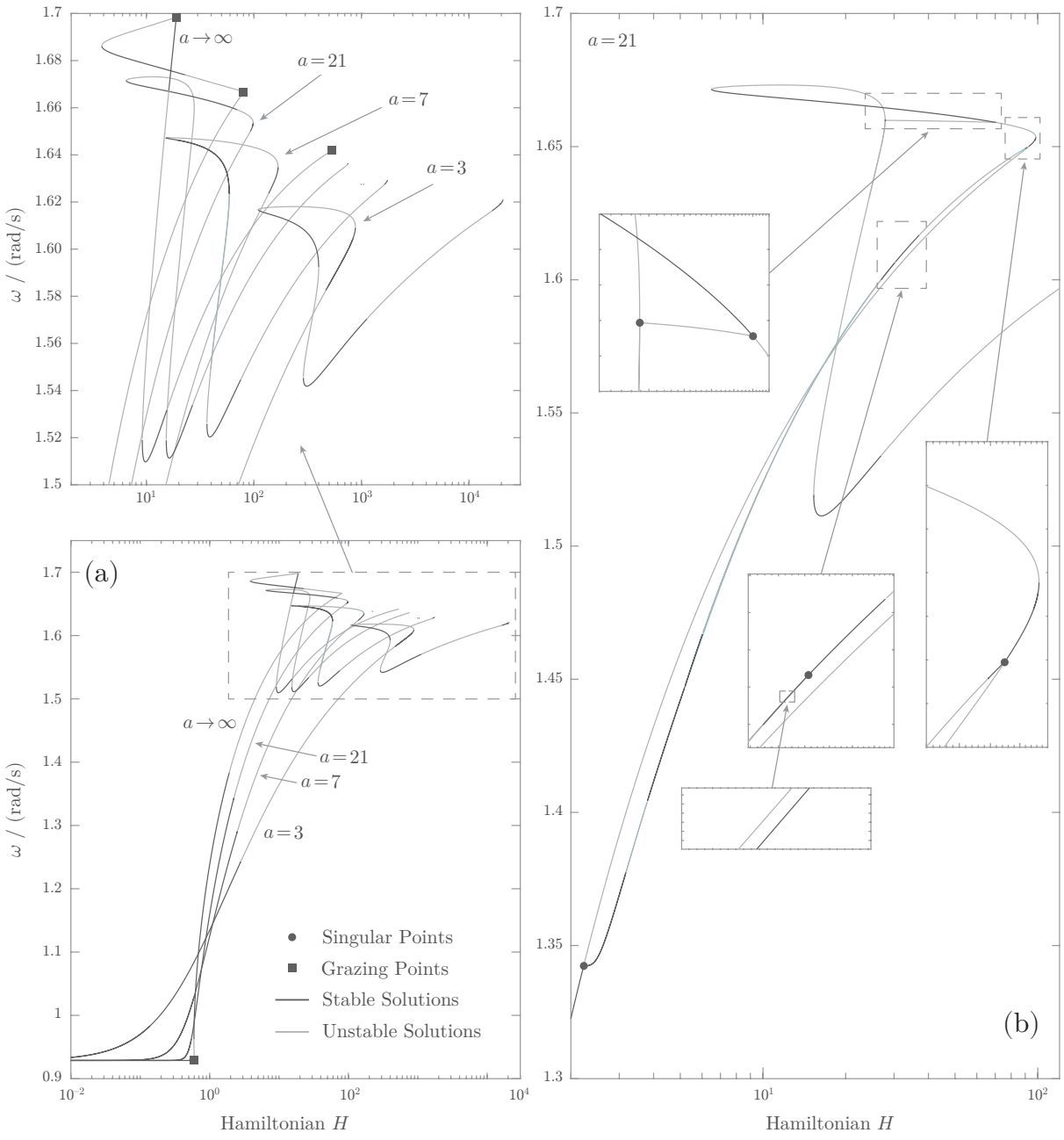

Figure 4.6. Counterpart frequency-energy plots of corresponding systems with continuous nonlinearities: a) Similarities showing a gradual transition from $a \to \infty$ to $a = 3$ with simpler topologies on the frequency-energy plot. b) Degeneration of the grazing point G_3 from Figure 4.5b into scattered singular points as a becomes finite.

frequency as energy increases, while that starting from ω_1 converges to ω_0 which is the natural frequency of an underlying system where the masses are fixed on each other. In other words, with high energies the nonlinear system degrades to a linear system where the degrees of freedom related with the nonlinear restoring force are combined. This convergence can be further demonstrated with selected time histories of chattering and sticking motions along the lower backbone as shown in Figure 4.5. The corresponding frequency-energy plots of the same system with a being finite are shown in Figure 4.6a while Figure 4.6b illustrates the degeneration of the bifurcation at grazing point G_3 in Figure 4.4 into scattered singular points as the nonlinearity becomes continuous. This indicates that the vibro-impact system, as the extreme case in the nonlinearity family 4.4, represents a fundamental scenario where conventional bifurcation (singular) points can be distinguished from grazing bifurcation points so that the intrinsic properties of the nonlinearity such as fractal structures of subharmonic bifurcations as shown in Figure A.3 can be revealed with minimal disturbance, where the Floquet multipliers of the corresponding Poincoré maps of the solution branches exhibit clean monotonic paths along the unit circle.

4.3 An Application of Embedded Triboelectric Generators

This section includes content from the publication: Hongcheng Tao and James Gibert. Multifunctional mechanical metamaterials with embedded triboelectric nanogenerators. *Advanced Functional Materials*, 30(23):2001720, 2020. [69]

The vertical-contact triboelectric generator (Figure 4.1f) is demonstrated in detail herein with an application of triboelectric mechanical metamaterials. Aspects such as physical interpretation of mechanical (mass, spring and static clearance) elements, dielectric and electrode construction, quasi-static and dynamic performance as well as multifunction of both energy harvesting and active sensing of general triboelectric generators are reflected.

4.3.1 Motivation

The ubiquitous nature of contact electrification between dissimilar materials as well as its almost universal saturation behavior in air allows design freedoms for flexible or even

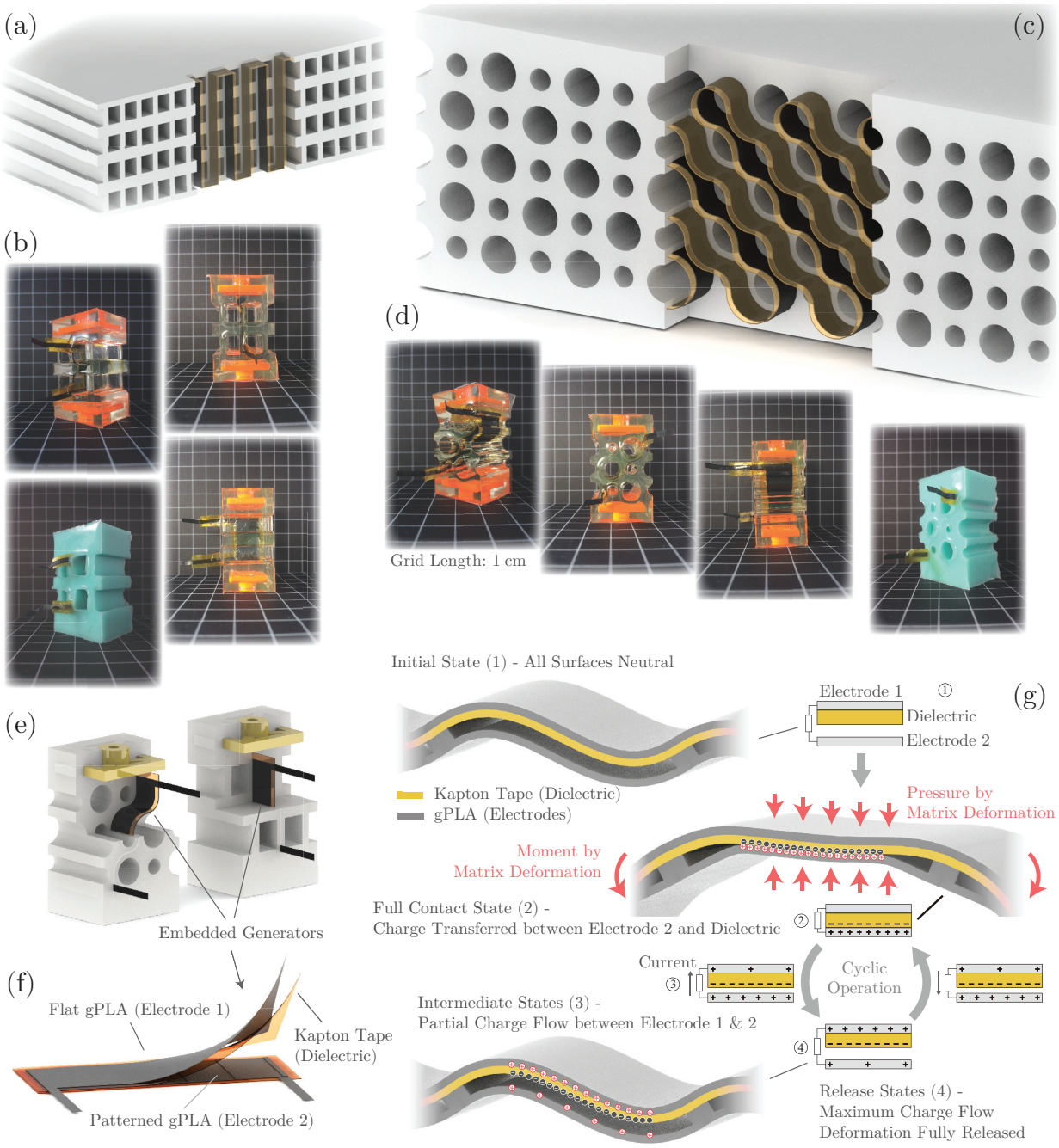

Figure 4.7. Construction of triboelectric-generator-embedded mechanical metamaterials: Conceptual design and semi-unit-cell fabrications of beam-array a) b) and bi-circular-hole c) d) samples. e) Inner structures of the semi-unit-cell samples showing embedded triboelectric generators f) and operational mechanism g).

stretchable triboelectric generator applications. This motivated the integration of triboelectric generators into mechanical structures that undergo large deformations to serve as a compliant attachment that provides additional functions such as energy harvesting and self-powered sensing with minimal interference to the designated structural purposes. Here, this concept is explored by prototyping triboelectric-generator-embedded mechanical metamaterials which, as a recently emerged topic, take advantage of deformation of localized geometric features rather than physical or chemical characteristics of the constituent material to achieve exotic and tunable mechanical or acoustic properties that do not occur naturally [70]–[72]. Typical designs include auxetic metamaterials that have negative Poisson's ratios [73], [74] and metamaterials employing local multi-stabilities for negative stiffness or tailorable constitutive relations [75]–[77]. Two archetypal geometries, namely the beam-array [78] and the bi-circular-hole [79] mechanical metamaterials, are selected here for illustration of triboelectric metamaterials given the large deformations during their operations and the simplicity of their 2-dimensional shapes. The beam-array geometry is a straightforward representative of shock absorbing metamaterials that utilize non-affine deformation due to buckling of its local members to yield a near-zero-stiffness plateau on their global macroscopic stress-strain curves, while the bi-circular-hole topology is an example of programmable metamaterials that can not only meet specific structural criteria by variations of design parameters but also adapt to updated requirements by external confinements or local geometric changes that can be easily applied to the already fabricated product. Figure 4.7a and 4.7c briefly explain the concept where the triboelectric generator is encapsulated in elastomeric polymer matrices cast into the selected geometries of mechanical metamaterials. As such the generator's deformation conforms to the localized deformation of the metamaterial, making the generator sensitive to the global macroscopic strain. This concept is parallel to, but also a natural continuation of, triboelectric generators employing porous materials [80], [81] which not only have rich exploitable structural properties but are also beneficial to the electric output performance thanks to increased contact areas.

4.3.2 Fabrication and Mechanisms

Triboelectric metamaterial specimens shown in Figure 4.7b and 4.7d are fabricated via a two-step silicone casting procedure. In the first step the main body of metamaterial geometries is cast where a relatively stiff placeholder is used to leave a slot along the designated wall for embedding the generator. The placeholder is removed after the matrix material cures and the flexible generator is then inserted into the slot, and the second casting step then seals it inside. The embedded generators are made of two 3D-printed conductive graphene PLA (gPLA) films and Kapton tape. Specifically, one flat gPLA film is placed as the electrode backing a layer of Kapton tape which serves as the dielectric for contact electrification. Another gPLA film is printed with a macroscopic surface pattern and used as the contact surface against the Kapton tape. The surface pattern behaves as discrete spacers and the two layers (the gPLA-Kapton layer and the patterned gPLA layer) thus form a single-dielectric vertical-contact triboelectric generator [82], and finally another Kapton tape is used to simply seal its edges to avoid silicone infiltration.

The embedded triboelectric generators give electric output signals when the matrix (silicone) structures deform, as shown in Figure 4.7g which is slightly different than the double-dielectric configuration as in Figure 4.1f. The gPLA and the Kapton tape surfaces are forced into contact by the combined effort of a moment due to bending of the matrix walls and a pressure due to both a component of the axial load on the matrix wall and the transverse stress it induces. The contact electrifies both surfaces so that negative charge is trapped on the surface of the Kapton tape while positive charge accumulates on the gPLA surface. The transferred charge remains on the dielectric (Kapton) surface when the matrix deformation is released and the layers are again separated from each other. This forms a static electric field and thus a potential difference between the gPLA electrodes which can be used as an open-circuit output voltage for active sensing purposes. When the electrodes are connected to any external load with finite impedance a transient current will be generated as the positive charge transferred to the gPLA electrode previously in contact flows to the other in order to balance the potential difference. Similarly, a current in the opposite direction emerges

when the matrix structure deforms again, and the system continuously generates electricity when the structure undergoes periodic deformations.

4.3.3 Quasi-Static and Dynamic Functions of Embedded Triboelectric Generators

The constructed metamaterials are multifunctional in that they not only inherit the assigned mechanical properties of the matrix structure but are also capable of harvesting energy as well as actively sensing its own deformation either quasi-statically or dynamically. Quasi-static deformation sensing is realized upon a map from the global strain of the matrix structure to the open-circuit output voltage which is highly dependent on the metamaterial geometry and the location of the generator. This is studied via uniaxial compression tests as shown in Figure 4.8a. The characteristic quasi-static deformation-voltage relations of the two prototyped geometries have exhibited different potential applications: in the beam-array geometry the voltage changes linearly with respect to the global displacement only within the initial small interval and the saturation that follows is used to indicate the onset of local beam buckling and thus entering a zero-stiffness functional region. The bi-circular-hole geometry under compression undergoes a relatively smooth deformation process, yielding a nonlinear but monotonic map from deformation to output voltage which can be directly adopted for measurements. The experimental results qualitatively match predictions by finite element analysis in COMSOL Multiphysics, which are linearly scaled by a presumed amount of saturated charge transfer resulting from contact electrification.

In practice mechanical metamaterials including the two geometries in discussion operate as mediums or supports that undergo continuous excitations, which is the fundamental scenario for applications of energy harvesters. The dynamic performance of the triboelectric metamaterials is herein studied by installing the metamaterials as a connection between a lumped mass and a shaker table that provides uniaxial motions, as shown in Figure 4.8d. The table executes a sinusoidal oscillation with constant magnitude while performing a sweep in frequency. Both samples benefit from their geometric nonlinearities to attain a broad bandwidth as the magnitude of the output voltage (measured across a finite resistance) closely follows the trend of the mass acceleration, which is potentially exploitable for calibrated

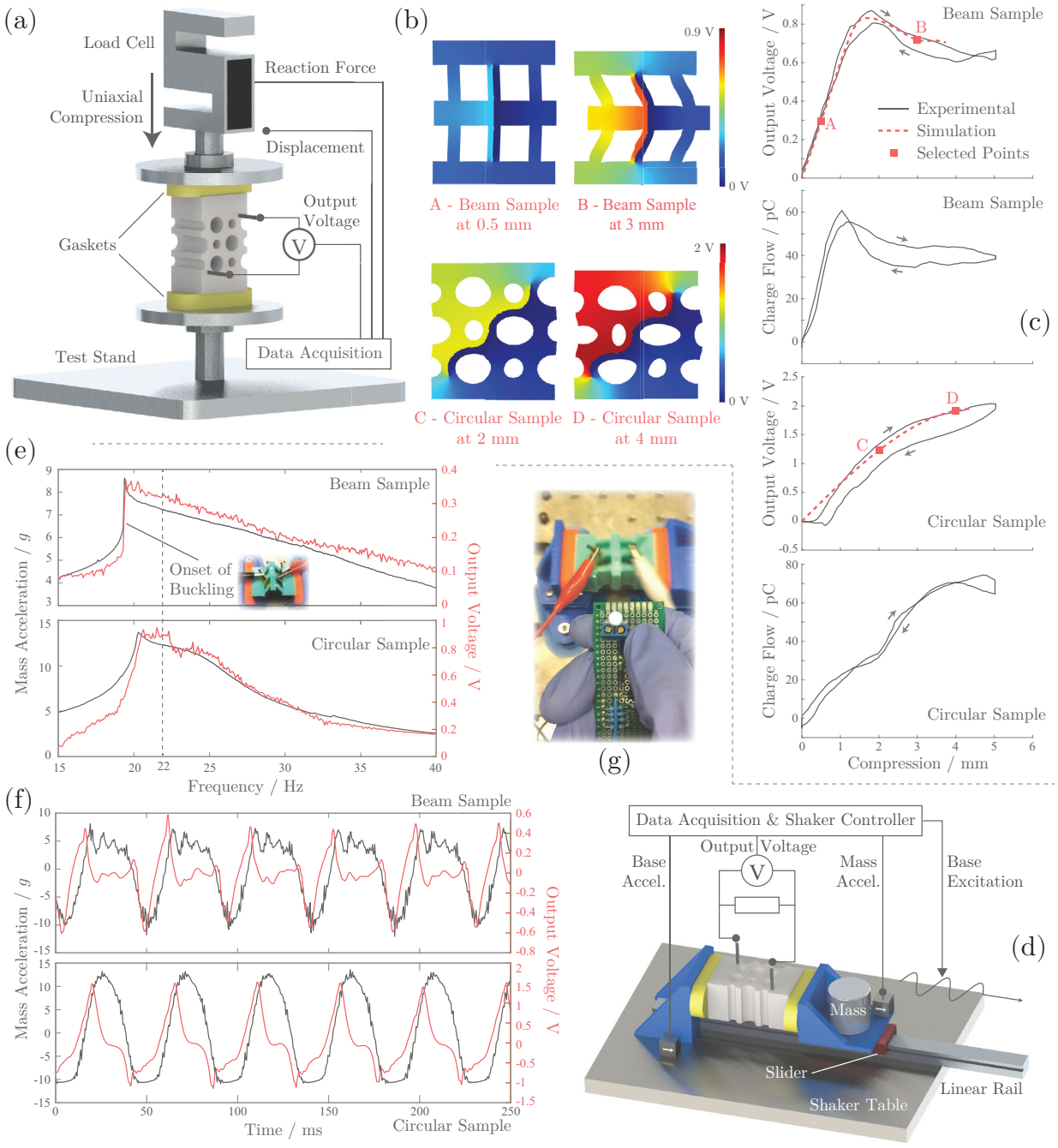

Figure 4.8. Quasi-static and dynamic functions of the mechanical metamaterial with embedded triboelectric generators: a) Test apparatus for quasi-static loading. b) Finite-element simulations of the potential field at selected points in c) the map from compression depth to electric output. d) Test apparatus for dynamic loading with e) frequency response and f) time history of the mass acceleration and output voltage from the generator. g) Energy harvesting illustrated during dynamic tests.

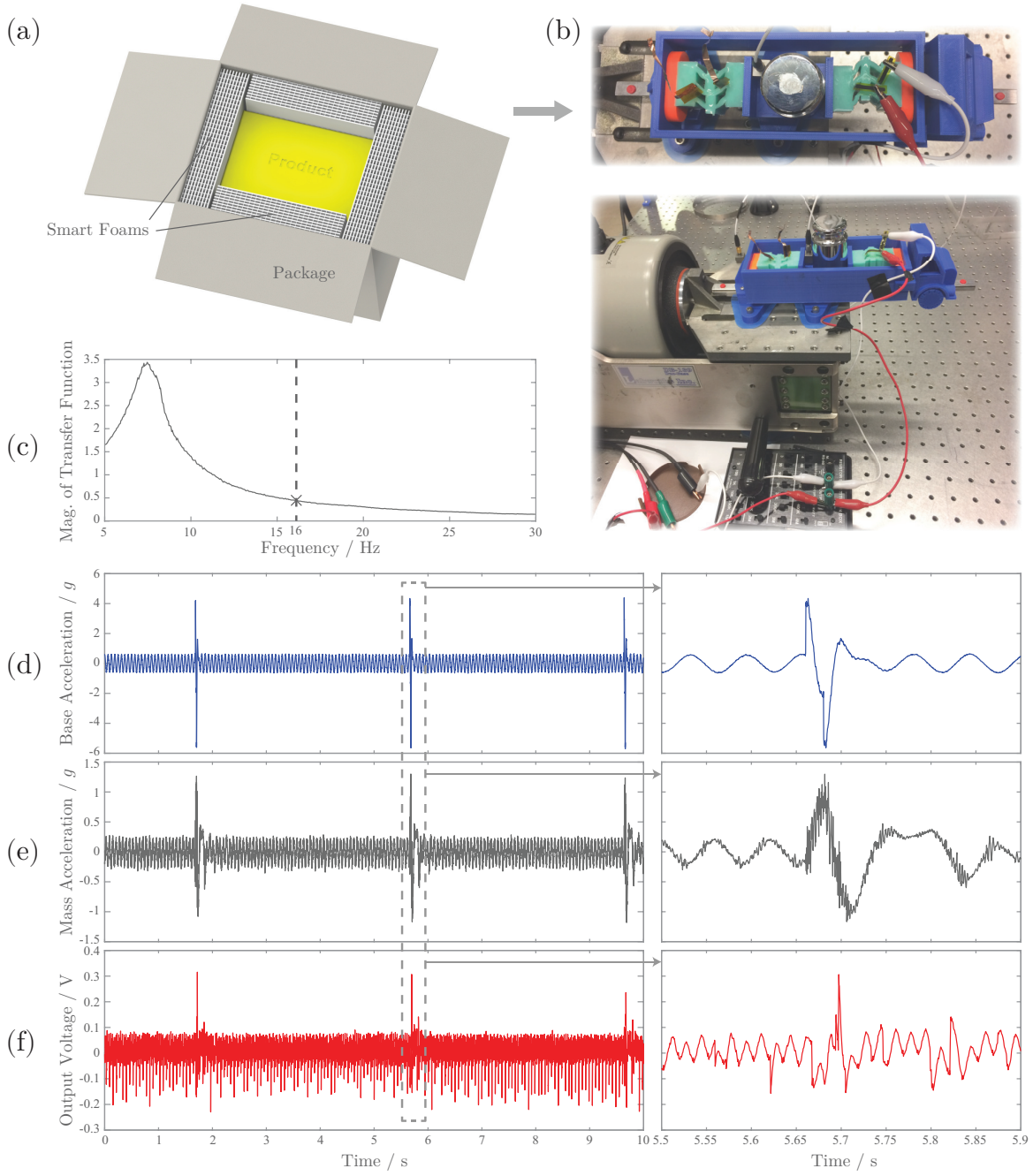

Figure 4.9. Triboelectric-generator-embedded mechanical metamaterials applied as smart foams for packaging: a) Concept and b) test apparatus on a shaker table, where two beam-array samples are preloaded to support a mass. c) Frequency response of the foam-mass system and time histories of d) base acceleration, e) mass acceleration and f) output voltage with details of a shock signal and its responses.

acceleration-sensing applications. The frequency response of the beam-array sample experiences a jump in magnitudes of mass acceleration and output voltage simultaneously while approaching a characteristic resonance of softening nonlinear springs, indicating the onset of beam buckling and thus near-zero stiffness leading to large deformations. The energy harvesting capability is demonstrated in the time history of output voltage as well as using the embedded generator to charge a capacitor that lights an LED intermittently. Finally, the multifunctional metamaterial is tested in a natural practice where the beam-array specimens are utilized as self-powered smart foams for general packaging systems, as shown in Figure 4.9, that structurally mitigate both vibrations and shocks during transportation while systematically monitoring such vibrations or shocks transmitted to the product in the package. This is briefly exhibited where a mass of 500 g is supported by two beam-array specimens acting as foams in a cart under shaker excitation. In this test the cart undergoes a sinusoidal excitation of $0.5g$, 16 Hz, simulating background vibrations in transportation, superposed with intermittent impulses simulating shocks caused by obstacles. The corresponding response of the mass shows both a 50 % attenuation for background vibrations and a 75 % attenuation for shocks, indicating the inherent structural function of the metamaterial shape. The output voltage of the embedded generator measured across a 10 MΩ resistance demonstrates the self-powered sensing function which successfully reflects the onset of shocks.

4.4 Air Breakdown in Triboelectric Energy Harvesters

Observations on the air breakdown in contact electrification as presented in Chapters 2 and 3 can be applied to generalize models of triboelectric energy harvesters [17]. Consider the equation of motion describing the double-dielectric triboelectric generator in Figure 4.1f

$$\begin{cases} m\ddot{x} + c\dot{x} + kx + f_{\mathrm{NL}}(x) + f_{\mathrm{ES}}(x,q) = -m\ddot{x}_{\mathrm{b}} \\ R\dot{q} + \left(\dfrac{h_1}{\varepsilon_1 A} + \dfrac{h_2}{\varepsilon_2 A}\right) q + \dfrac{h_{\mathrm{a}} + x}{\varepsilon_{\mathrm{air}} A} (q - Q) = 0 \end{cases} \tag{4.20}$$

where $f_{\mathrm{NL}}(x)$ defines the nonlinearity introduced by impacts (neglecting other intrinsic mechanical nonlinear restoring forces), $f_{\mathrm{ES}}(x,q)$ represents the Coulomb (electrostatic) force, A

is the identical macroscopic surface area of both the electrodes and the dielectric layers, h_{a} is the air gap distance at equilibrium before the surfaces are charged, h_1 and h_2 are thicknesses of the dielectric layers, and $\varepsilon_{\mathrm{air}}$, ε_1 and ε_2 are permittivities of air and the dielectric materials, respectively. Let the impacts be stereo-mechanical so that the velocity of the proof mass is updated by $\dot{x}^+ = -c_{\mathrm{r}}\dot{x}^-$ whenever $x + h_{\mathrm{a}} \leq 0$, and by neglecting transient charge accumulations let each impact update the dielectric surface charge density to the raw level so that $Q^+ = \sigma_{\mathrm{r}} A$. Neglect breakdown of the dielectric layers and let charge dissipation by air breakdown be continuous so that the dielectric surface charge is updated by

$$Q = q + \frac{2\varepsilon_{\mathrm{air}} A}{x + h_{\mathrm{a}}} V_{\mathrm{b}} = q + \frac{2\varepsilon_{\mathrm{air}} A B_{\mathrm{g}} p}{\ln\left[A_{\mathrm{g}} p \left(x + h_{\mathrm{a}}\right)\right] - \ln\left[\ln\left(1 + \gamma_{\mathrm{se}}^{-1}\right)\right]} \tag{4.21}$$

whenever

$$\frac{Q - q}{2\varepsilon_{\mathrm{a}} A}\left(x + h_{\mathrm{a}}\right) \geq V_{\mathrm{b}} = \frac{B_{\mathrm{g}} p \left(x + h_{\mathrm{a}}\right)}{\ln\left[A_{\mathrm{g}} p \left(x + h_{\mathrm{a}}\right)\right] - \ln\left[\ln\left(1 + \gamma_{\mathrm{se}}^{-1}\right)\right]},$$

assuming $Q > q$, while the Coulomb force is evaluated using the infinite-parallel-plate assumption so that $f_{\mathrm{ES}}(x, q) = \dfrac{(Q - q)^2}{2\varepsilon_{\mathrm{air}} A}$. Apply physical parameters $m = 0.1\,\mathrm{kg}$, $k = 20\,\mathrm{kN/m}$, $\zeta = \dfrac{c}{2\sqrt{km}} = 0.1$, $c_{\mathrm{r}} = 0.9$, $A = 0.01\,\mathrm{m}^2$, $\varepsilon_1 = \varepsilon_2 = 3\varepsilon_{\mathrm{air}}$, $h_{\mathrm{a}} = 1\,\mathrm{mm}$, $h_1 = h_2 \triangleq h_{\mathrm{d}} = 0.5\,\mathrm{mm}$, $\ddot{x}_{\mathrm{b}} = |\ddot{x}_{\mathrm{b}}| \sin \omega_{\mathrm{n}} t$ where $|\ddot{x}_{\mathrm{b}}| = 200\,\mathrm{m/s}^2$ and $\omega_{\mathrm{n}} = \sqrt{\dfrac{k}{m}} = 447\,\mathrm{rad/s}$, $R = 200\,\mathrm{k\Omega}$ and $\sigma_{\mathrm{r}} = 200\,\mu\mathrm{C/m}^2$.

The average of simulated steady-state output power $P = \dot{q}^2 R$ for various air pressures is depicted in Figure 4.10a, while time histories of system states at atmospheric pressure are displayed in Figre 4.10b where it is clear that air breakdown during the separation stages immediately dissipates the charge deposited on the surfaces at instants of impact. Time histories of the system response at pressures labeled in Figure 4.10a are shown in Figure 4.11. At either extremely low (e.g., 1.2 Torr) or high pressures (e.g., 2400 Torr) the voltage across the air gap can not trigger breakdown at any instant, allowing the dielectric surface charge density to maintain the raw saturation level σ_{r} so that the current $\dot{q}$ shows higher impulses than that at atmospheric pressure. However, this does not yield the maximum power output which is found instead at intermediate pressures (e.g., 3.4 Torr) where the first air breakdown incident is triggered at a significant gap distance so that it induces another impulse in the

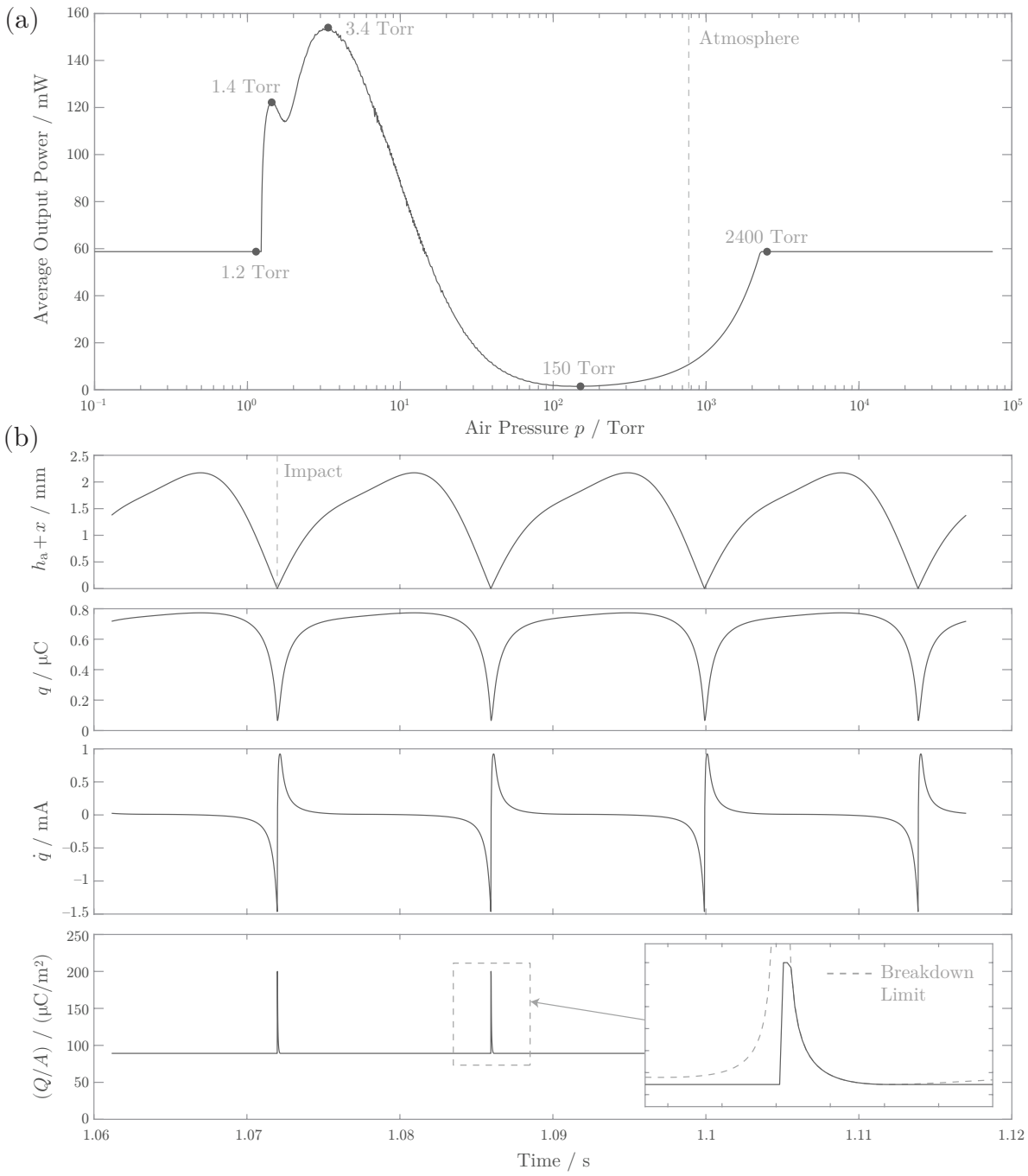

Figure 4.10. Simulated performance of a vibro-impact triboelectric energy harvester under various air pressures: a) Average steady-state output power. b) Steady-state time histories of gap distance $x + h_a$, charge flow q, current $\dot{q}$ and dielectric surface charge density Q/A, subjected to both breakdown discharge and resets at impacts, under atmospheric pressure.

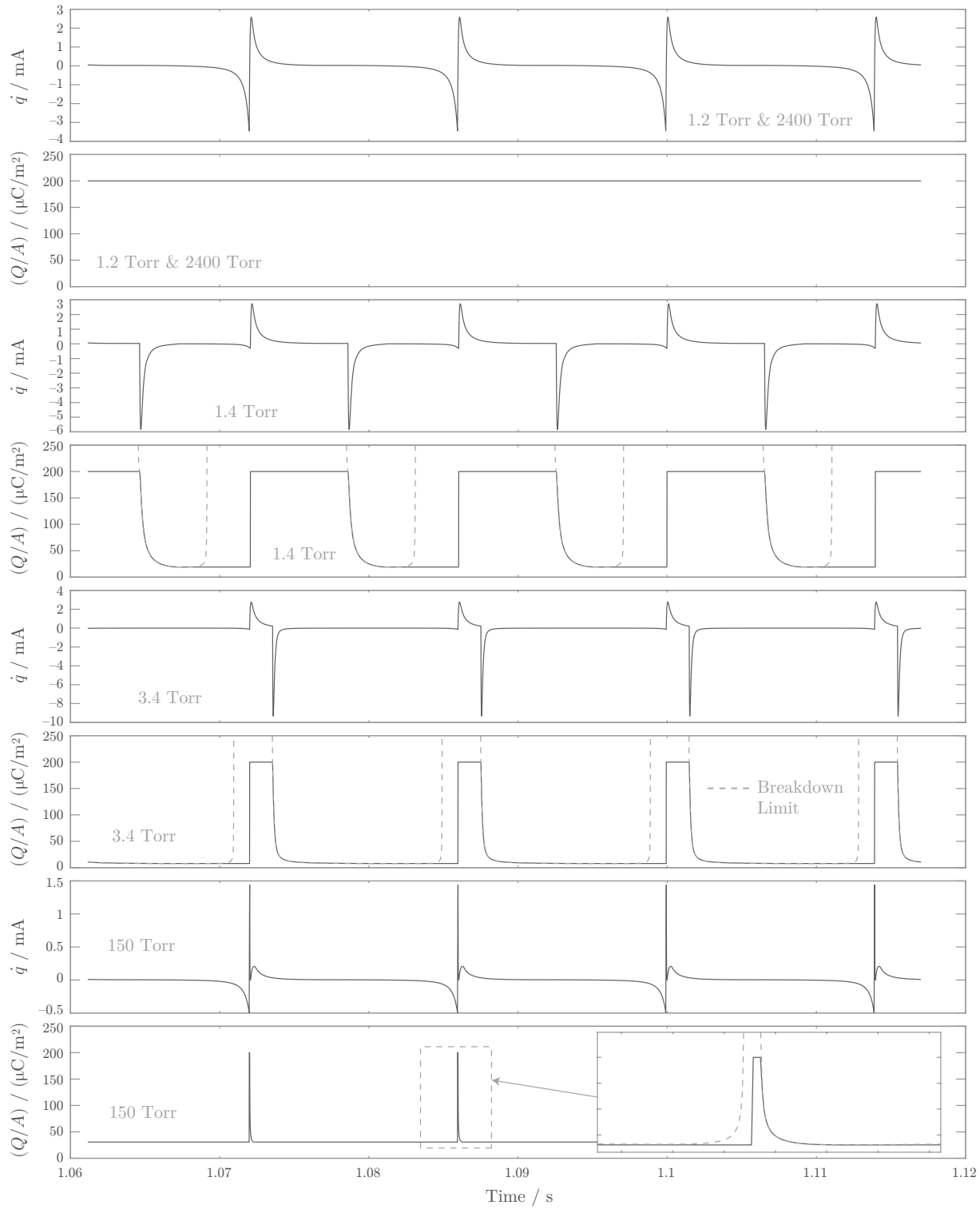

Figure 4.11. Steady-state time histories of current and dielectric surface charge density under selected air pressures.

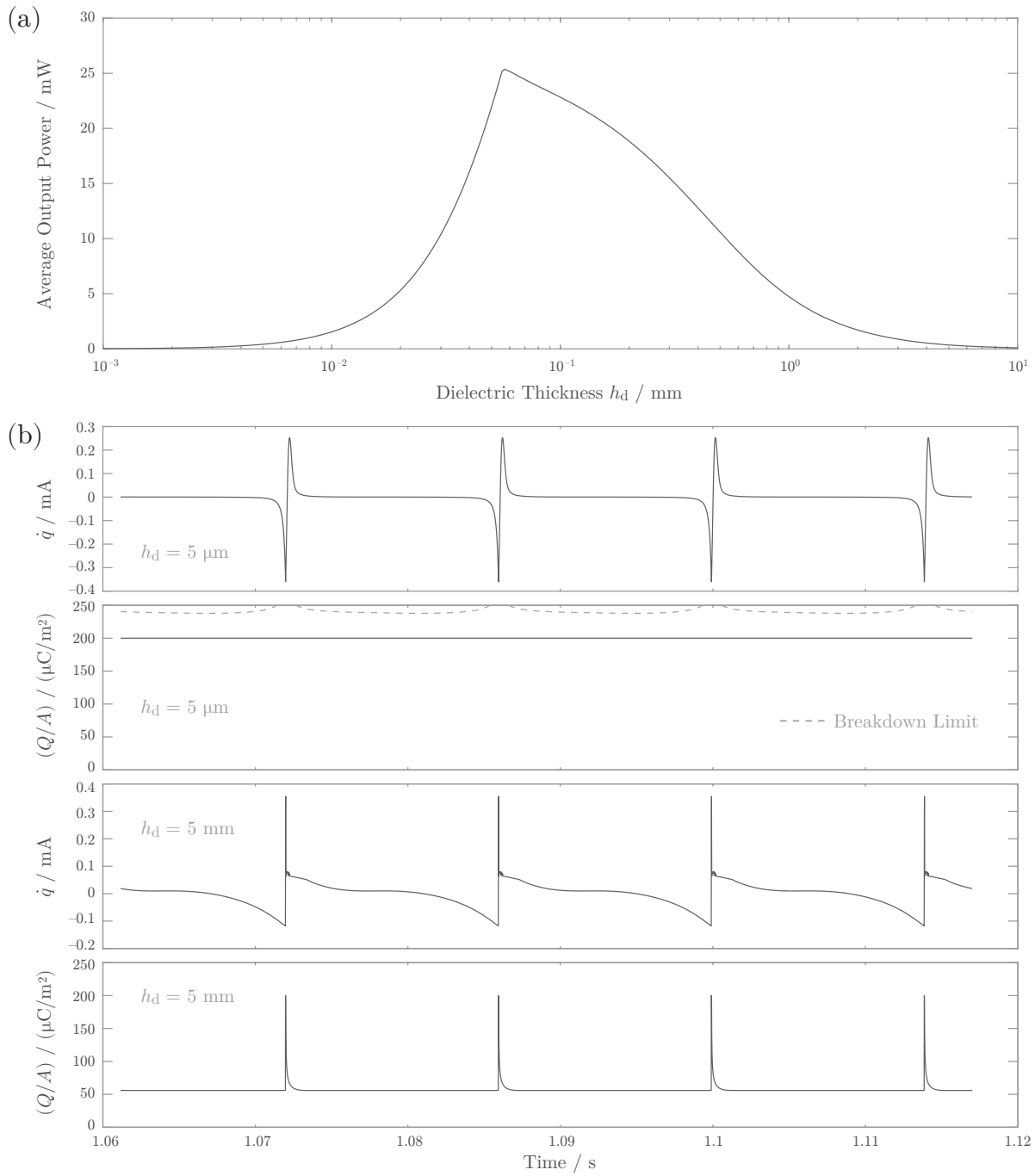

Figure 4.12. Simulated performance of a vibro-impact triboelectric energy harvester with various dielectric layer thicknesses under atmospheric pressure: a) Average steady-state output power. b) Steady-state time histories of current and dielectric surface charge density with selected dielectric thicknesses.

current and adds to the total power output, which is preferable compared to the breakdown incidents under higher air pressures where such second impulse is both indistinguishable from that due to charge reset at impacts and low in magnitude since it is triggered at smaller gaps and thus provides a lower change of voltage. Nonetheless, the existence of such boost of power output by air breakdown incidents late in a cycle may be less promising in reality because the assumption that each impact resets the dielectric surface charge density to the saturated level is overly optimistic since more cycles are generally required for the surface charge to accumulate.

The dielectric layer thickness h_{d} is another practical design parameter since ambient air pressure is not controllable in most applications. The average steady-state output power for various dielectric thicknesses under atmospheric pressure is shown in Figure 4.12 indicating the existence of an optimal thickness. While dielectric layers which are magnitudes thinner than the air gap help eliminate its breakdown by mitigating the gap voltage with induced charge in the electrodes, the induced current is reduced for dielectric layers either too thick or too thin. This also implies that a compact design of triboelectric energy harvester where both the variance of air gap and the dielectric thicknesses are limited under several micrometers can sufficiently suppress surface charge loss due to air breakdown, which justifies a more popular terminology known as triboelectric nanogenerators. Meanwhile, the significance of the Coulomb attraction $f_{\mathrm{ES}}(x, q)$ is not investigated since its influence is correlated with mechanical parameters m and k which can be easily manipulated.

5. SUMMARY AND DISCUSSIONS

The primary contribution of the present work lies in the design and implementation of a test strategy for determining Paschen's law for the separation stage of contact electrification between dielectric materials. The experimental results have demonstrated two halves of the Paschen curve divided at the location of minimum breakdown voltage with respect to air pressure, i.e., the left half where the breakdown voltage decreases with pressure and the right half where it increases. However, only the left half of the Paschen curve with respect to gap distance is revealed due to the loss of accuracy for Coulomb force measurements as the gap increases, even after adopting a substantial sample size. The situation may be improved using a load cell with higher precision to yield a convincing increase of breakdown voltage with respect to gap distance past the minimum point.

The verification of Paschen's law for dielectric contact electrification proves the feasibility of performing charging cycles and Coulomb force measurements with eliminated interference of air breakdown using the same test setup, which is conducted to investigate the raw charge accumulation of multiple contact pairs. Significantly higher surface charge densities are observed compared to tests in atmospheric air, the consistency of which is adequate but not satisfactory for quantitative conclusions on characterizing the charging of the tested materials. Additional conditions such as relative humidity, design of test steps and most importantly the preparation and preservation of sample surfaces [1] need to be controlled toward the goal of establishing a quantitative triboelectric series. Improvements in sample fabrication may also facilitate consideration of more material combinations since silicone (PDMS) has been fixed as the reference for all tests so far. It has also been attempted to introduce a rubbing mechanism using an additional stepper motor in the test apparatus to enhance the charging between surfaces with less elasticity than silicone.

The same set of tests also reports potential surface alternations observed in PTFE samples due to high-energy breakdown discharge in vacuum, while it remains unclear how this is related to the decrease of saturated charge density in following tests, whether due to a reduced effective contact area or a change of local chemical structure which further requires clarification of the original charging mechanism. Although similar decreases in saturated

charge density have not been observed in other tested polymers which are presumably more stable than PTFE under strikes of electron or cation beams, further investigations can be done by repeatedly discharging these samples under low air pressure to seek evidence for any accumulation of surface damage. A parallel approach can be pursued by monitoring the spectrum of photon emissions (triboluminescence) during breakdown discharge under various air pressures to reflect electron excitations in both the plasma and the surfaces struck by accelerated electrons / cations [83], [84]. However, it can after all be argued whether repeated contact electrification tests with surface charge reset by breakdown of the gas medium in between should necessarily behave consistently even with perfect sample conditions, since the breakdown discharge clearly does not reverse the charging process. The surface charge neutralization by arrivals of electrons and cations is theoretically a global and macroscopic phenomenon, i.e., it is not guaranteed that the incident electrons precisely fill in sites on the (dielectric) anode where electrons were deprived during contact electrification, or that the cations capture exactly the electrons previously deposited onto the (dielectric) cathode. The complicated dynamics in such process of charge neutralization will inevitably alter the surface states, which can be either transient so as to affect repeated contact electrification tests immediately after the discharge or permanent like the damage observed on post-discharge PTFE samples.

The application of the experimental results are illustrated in the introduction of surface charge reset and dissipation via breakdown into models of vibro-impact triboelectric energy harvesters, which shows promising potentials not only in more realistic predictions of their performance but also in revealing the feasibility of exploiting breakdown discharge to enhance the output. Test apparatuses are to be implemented based on a prototype shown in Figure A.4 to realize vibrational excitations in a vacuum chamber or refined control of dielectric layer thicknesses for tests in atmospheric air, challenges in which also include matching the selected parameters with proper choice of the external load/resistor. Further improvements of the dynamical model require the inclusion of non-electrostatic (intermolecular) adhesions (Figure 3.1b) which should significantly reshape the mechanical responses if dielectric surfaces such as silicone are employed in the contact pair.

REFERENCES

[1] W. R. Harper, *Contact and frictional electrification*. Clarendon P., 1967.

[2] J. Lowell and A. Rose-Innes, "Contact electrification," *Advances in Physics*, vol. 29, no. 6, pp. 947–1023, 1980.

[3] C. X. Lu, C. B. Han, G. Q. Gu, *et al.*, "Temperature effect on performance of triboelectric nanogenerator," *Advanced Engineering Materials*, vol. 19, no. 12, p. 1 700 275, 2017.

[4] V. Nguyen and R. Yang, "Effect of humidity and pressure on the triboelectric nanogenerator," *Nano Energy*, vol. 2, no. 5, pp. 604–608, 2013.

[5] V. Nguyen, R. Zhu, and R. Yang, "Environmental effects on nanogenerators," *Nano Energy*, vol. 14, pp. 49–61, 2015.

[6] F. Paschen, *Ueber die zum funkenübergang in luft: wasserstoff und kohlensäure bei verschiedenen drucken erforderliche potentialdifferenz...* JA Barth, 1889.

[7] C. Wadhwa, *High voltage engineering*. New Age International, 2006.

[8] H. B. Garrett, "The charging of spacecraft surfaces," *Reviews of Geophysics*, vol. 19, no. 4, pp. 577–616, 1981.

[9] H. Koons, J. Mazur, R. Selesnick, J. Blake, and J. Fennell, "The impact of the space environment on space systems," AEROSPACE CORP EL SEGUNDO CA EL SEGUNDO TECHNICAL OPERATIONS, Tech. Rep., 1999.

[10] J. Townsend, *The theory of ionization of gases by collision*. Constable, Limited, 1910.

[11] J. S. Townsend, *Electricity in gases*. 1915.

[12] R. Elsdon and F. Mitchell, "Contact electrification of polymers," *Journal of Physics D: Applied Physics*, vol. 9, no. 10, p. 1445, 1976.

[13] T. Matsuyama and H. Yamamoto, "Charge relaxation process dominates contact charging of a particle in atmospheric conditions," *Journal of Physics D: Applied Physics*, vol. 28, no. 12, p. 2418, 1995.

[14] R. G. Horn and D. T. Smith, "Contact electrification and adhesion between dissimilar materials," *Science*, vol. 256, no. 5055, pp. 362–364, 1992.

[15] D. J. Lacks and R. M. Sankaran, "Contact electrification of insulating materials," *Journal of Physics D: Applied Physics*, vol. 44, no. 45, p. 453 001, 2011.

[16] Z. Yi, D. Liu, L. Zhou, *et al.*, "Enhancing output performance of direct-current triboelectric nanogenerator under controlled atmosphere," *Nano Energy*, vol. 84, p. 105 864, 2021.

[17] Y. Liu, W. Liu, Z. Wang, *et al.*, "Quantifying contact status and the air-breakdown model of charge-excitation triboelectric nanogenerators to maximize charge density," *Nature communications*, vol. 11, no. 1, pp. 1–8, 2020.

[18] B. Kwetkus, K. Sattler, and H.-C. Siegmann, "Gas breakdown in contact electrification," *Journal of Physics D: Applied Physics*, vol. 25, no. 2, p. 139, 1992.

[19] J. Fu, G. Xu, C. Li, *et al.*, "Achieving ultrahigh output energy density of triboelectric nanogenerators in high-pressure gas environment," *Advanced Science*, vol. 7, no. 24, p. 2 001 757, 2020.

[20] J. Wang, C. Wu, Y. Dai, *et al.*, "Achieving ultrahigh triboelectric charge density for efficient energy harvesting," *Nature communications*, vol. 8, no. 1, pp. 1–8, 2017.

[21] M. Hogue, C. Buhler, C. Calle, T. Matsuyama, W. Luo, and E. Groop, "Insulator–insulator contact charging and its relationship to atmospheric pressure," *Journal of electrostatics*, vol. 61, no. 3-4, pp. 259–268, 2004.

[22] F.-R. Fan, L. Lin, G. Zhu, W. Wu, R. Zhang, and Z. L. Wang, "Transparent triboelectric nanogenerators and self-powered pressure sensors based on micropatterned plastic films," *Nano letters*, vol. 12, no. 6, pp. 3109–3114, 2012.

[23] H. Baytekin, A. Patashinski, M. Branicki, B. Baytekin, S. Soh, and B. A. Grzybowski, "The mosaic of surface charge in contact electrification," *Science*, vol. 333, no. 6040, pp. 308–312, 2011.

[24] A. E. Wang, P. S. Gil, M. Holonga, *et al.*, "Dependence of triboelectric charging behavior on material microstructure," *Physical Review Materials*, vol. 1, no. 3, p. 035 605, 2017.

[25] J. H. Lee, R. Hinchet, S. K. Kim, S. Kim, and S.-W. Kim, "Shape memory polymer-based self-healing triboelectric nanogenerator," *Energy & Environmental Science*, vol. 8, no. 12, pp. 3605–3613, 2015.

[26] S. Liu, W. Zheng, B. Yang, and X. Tao, "Triboelectric charge density of porous and deformable fabrics made from polymer fibers," *Nano energy*, vol. 53, pp. 383–390, 2018.

[27] C. Xu, Y. Zi, A. C. Wang, *et al.*, "On the electron-transfer mechanism in the contact-electrification effect," *Advanced Materials*, vol. 30, no. 15, p. 1 706 790, 2018.

[28] H. Zou, Y. Zhang, L. Guo, *et al.*, "Quantifying the triboelectric series," *Nature communications*, vol. 10, no. 1, pp. 1–9, 2019.

[29] A. Ghaffarinejad and J. Y. Hasani, "Modeling of triboelectric charge accumulation dynamics at the metal–insulator interface for variable capacitive structures: Application to triboelectric nanogenerators," *Applied Physics A*, vol. 125, no. 4, p. 259, 2019.

[30] Y. Zhang and T. Shao, "A method of charge measurement for contact electrification," *Journal of Electrostatics*, vol. 71, no. 4, pp. 712–716, 2013.

[31] H. Tao, G. Batt, and J. Gibert, "Modeling contact electrification in triboelectric impact oscillators as energy harvesters," in *Sensors and Smart Structures Technologies for Civil, Mechanical, and Aerospace Systems 2019*, vol. 10970, 2019, 109700U.

[32] B. Terris, J. Stern, D. Rugar, and H. Mamin, "Contact electrification using force microscopy," *Physical Review Letters*, vol. 63, no. 24, p. 2669, 1989.

[33] C. Schönenberger and S. Alvarado, "Observation of single charge carriers by force microscopy," *Physical review letters*, vol. 65, no. 25, p. 3162, 1990.

[34] S. Lin, L. Xu, A. C. Wang, and Z. L. Wang, "Quantifying electron-transfer in liquid-solid contact electrification and the formation of electric double-layer," *Nature communications*, vol. 11, no. 1, pp. 1–8, 2020.

[35] B. Gady, R. Reifenberger, and D. Rimai, "Contact electrification studies using atomic force microscope techniques," *Journal of applied physics*, vol. 84, no. 1, pp. 319–322, 1998.

[36] A. Roberts, "Surface charge contribution in rubber adhesion and friction," *Journal of Physics D: Applied Physics*, vol. 10, no. 13, p. 1801, 1977.

[37] E. Husain and R. Nema, "Analysis of paschen curves for air, n2 and sf6 using the townsend breakdown equation," *IEEE transactions on electrical insulation*, no. 4, pp. 350–353, 1982.

[38] M. Seol, S. Kim, Y. Cho, *et al.*, "Triboelectric series of 2d layered materials," *Advanced Materials*, vol. 30, no. 39, p. 1 801 210, 2018.

[39] D. J. Lacks and T. Shinbrot, "Long-standing and unresolved issues in triboelectric charging," *Nature Reviews Chemistry*, vol. 3, no. 8, pp. 465–476, 2019.

[40] A. Diaz and R. Felix-Navarro, "A semi-quantitative tribo-electric series for polymeric materials: The influence of chemical structure and properties," *Journal of Electrostatics*, vol. 62, no. 4, pp. 277–290, 2004.

[41] L. S. McCarty and G. M. Whitesides, "Electrostatic charging due to separation of ions at interfaces: Contact electrification of ionic electrets," *Angewandte Chemie International Edition*, vol. 47, no. 12, pp. 2188–2207, 2008.

[42] X. Zhang, L. Chen, Y. Jiang, W. Lim, and S. Soh, "Rationalizing the triboelectric series of polymers," *Chemistry of Materials*, vol. 31, no. 5, pp. 1473–1478, 2019.

[43] H. Mizes, E. Conwell, and D. Salamida, "Direct observation of ion transfer in contact charging between a metal and a polymer," *Applied physics letters*, vol. 56, no. 16, pp. 1597–1599, 1990.

[44] R. K. Pandey, H. Kakehashi, H. Nakanishi, and S. Soh, "Correlating material transfer and charge transfer in contact electrification," *The Journal of Physical Chemistry C*, vol. 122, no. 28, pp. 16 154–16 160, 2018.

[45] M. M. Apodaca, P. J. Wesson, K. J. Bishop, M. A. Ratner, and B. A. Grzybowski, "Contact electrification between identical materials," *Angewandte Chemie International Edition*, vol. 49, no. 5, pp. 946–949, 2010.

[46] M. F. Daqaq, R. Masana, A. Erturk, and D. Dane Quinn, "On the role of nonlinearities in vibratory energy harvesting: A critical review and discussion," *Applied Mechanics Reviews*, vol. 66, no. 4, 2014.

[47] L. Cveticanin, M. KalamiYazdi, H. Askari, and Z. Saadatnia, "Vibration of a two-mass system with non-integer order nonlinear connection," *Mechanics Research Communications*, vol. 43, pp. 22–28, 2012.

[48] S. W. Shaw and P. Holmes, "A periodically forced piecewise linear oscillator," *Journal of sound and vibration*, vol. 90, no. 1, pp. 129–155, 1983.

[49] H. Tao and J. Gibert, "Periodic orbits of a conservative 2-dof vibro-impact system by piecewise continuation: Bifurcations and fractals," *Nonlinear Dynamics*, vol. 95, no. 4, pp. 2963–2993, 2019.

[50] V. Gueorguiev, A. Rau, and J. Draayer, "Confined one-dimensional harmonic oscillator as a two-mode system," *American journal of physics*, vol. 74, no. 5, pp. 394–403, 2006.

[51] V. Pilipchuk, "The calculation of strongly non-linear systems close to vibration impact systems," *Journal of Applied Mathematics and Mechanics*, vol. 49, no. 5, pp. 572–578, 1985.

[52] V. N. Pilipchuk, *Nonlinear dynamics: between linear and impact limits*. Springer Science & Business Media, 2010, vol. 52.

[53] B. Blazejczyk-Okolewska, K. Czolczynski, and T. Kapitaniak, "Dynamics of a two-degree-of-freedom cantilever beam with impacts," *Chaos, Solitons & Fractals*, vol. 40, no. 4, pp. 1991–2006, 2009.

[54] Y. Yue, "Bifurcations of the symmetric quasi-periodic motion and lyapunov dimension of a vibro-impact system," *Nonlinear Dynamics*, vol. 84, no. 3, pp. 1697–1713, 2016.

[55] A. Banerjee, R. Das, and E. P. Calius, "Vibration transmission through an impacting mass-in-mass unit, an analytical investigation," *International Journal of Non-Linear Mechanics*, vol. 90, pp. 137–146, 2017.

[56] S. Shaw, "Forced vibrations of a beam with one-sided amplitude constraint: Theory and experiment," *Journal of Sound and Vibration*, vol. 99, no. 2, pp. 199–212, 1985.

[57] E. H. Moussi, S. Bellizzi, B. Cochelin, and I. Nistor, "Nonlinear normal modes of a two degrees-of-freedom piecewise linear system," *Mechanical Systems and Signal Processing*, vol. 64, pp. 266–281, 2015.

[58] M. Pascal, "Dynamics and stability of a two degree of freedom oscillator with an elastic stop," 2006.

[59] S. Foale and S. Bishop, "Bifurcations in impact oscillations," *Nonlinear dynamics*, vol. 6, no. 3, pp. 285–299, 1994.

[60] E. Van de Vorst, D. Van Campen, A. De Kraker, and R. Fey, "Periodic solutions of a multi-dof beam system with impact," *Journal of Sound and Vibration*, vol. 192, no. 5, pp. 913–925, 1996.

[61] C. Wu, A. C. Wang, W. Ding, H. Guo, and Z. L. Wang, "Triboelectric nanogenerator: A foundation of the energy for the new era," *Advanced Energy Materials*, vol. 9, no. 1, p. 1 802 906, 2019.

[62] G. Zhu, B. Peng, J. Chen, Q. Jing, and Z. L. Wang, "Triboelectric nanogenerators as a new energy technology: From fundamentals, devices, to applications," *Nano Energy*, vol. 14, pp. 126–138, 2015.

[63] S. Wang, L. Lin, Y. Xie, Q. Jing, S. Niu, and Z. L. Wang, "Sliding-triboelectric nanogenerators based on in-plane charge-separation mechanism," *Nano letters*, vol. 13, no. 5, pp. 2226–2233, 2013.

[64] D. Liu, X. Yin, H. Guo, *et al.*, "A constant current triboelectric nanogenerator arising from electrostatic breakdown," *Science advances*, vol. 5, no. 4, eaav6437, 2019.

[65] Y. Wang, Y. Yang, and Z. L. Wang, "Triboelectric nanogenerators as flexible power sources," *npj Flexible Electronics*, vol. 1, no. 1, pp. 1–10, 2017.

[66] S. Chen, Y. Pang, H. Yuan, X. Tan, and C. Cao, "Smart soft actuators and grippers enabled by self-powered tribo-skins," *Advanced Materials Technologies*, vol. 5, no. 4, p. 1 901 075, 2020.

[67] G. Kerschen, M. Peeters, J.-C. Golinval, and A. F. Vakakis, "Nonlinear normal modes, part i: A useful framework for the structural dynamicist," *Mechanical systems and signal processing*, vol. 23, no. 1, pp. 170–194, 2009.

[68] M. Peeters, R. Viguié, G. Sérandour, G. Kerschen, and J.-C. Golinval, "Nonlinear normal modes, part ii: Toward a practical computation using numerical continuation techniques," *Mechanical systems and signal processing*, vol. 23, no. 1, pp. 195–216, 2009.

[69] H. Tao and J. Gibert, "Multifunctional mechanical metamaterials with embedded triboelectric nanogenerators," *Advanced Functional Materials*, vol. 30, no. 23, p. 2 001 720, 2020.

[70] Y. Jiang and Q. Wang, "Highly-stretchable 3d-architected mechanical metamaterials," *Scientific reports*, vol. 6, no. 1, pp. 1–11, 2016.

[71] K. Bertoldi, V. Vitelli, J. Christensen, and M. Van Hecke, "Flexible mechanical metamaterials," *Nature Reviews Materials*, vol. 2, no. 11, pp. 1–11, 2017.

[72] D. Z. Rocklin, S. Zhou, K. Sun, and X. Mao, "Transformable topological mechanical metamaterials," *Nature communications*, vol. 8, no. 1, pp. 1–9, 2017.

[73] J. N. Grima, R. Caruana-Gauci, M. R. Dudek, K. W. Wojciechowski, and R. Gatt, "Smart metamaterials with tunable auxetic and other properties," *Smart Materials and Structures*, vol. 22, no. 8, p. 084 016, 2013.

[74] C. Lv, D. Krishnaraju, G. Konjevod, H. Yu, and H. Jiang, "Origami based mechanical metamaterials," *Scientific reports*, vol. 4, no. 1, pp. 1–6, 2014.

[75] T. Mullin, S. Deschanel, K. Bertoldi, and M. C. Boyce, "Pattern transformation triggered by deformation," *Physical review letters*, vol. 99, no. 8, p. 084 301, 2007.

[76] L. R. Meza, S. Das, and J. R. Greer, "Strong, lightweight, and recoverable three-dimensional ceramic nanolattices," *Science*, vol. 345, no. 6202, pp. 1322–1326, 2014.

[77] A. Rafsanjani, A. Akbarzadeh, and D. Pasini, "Snapping mechanical metamaterials under tension," *Advanced Materials*, vol. 27, no. 39, pp. 5931–5935, 2015.

[78] P. Vuyk, S. Cui, and R. L. Harne, "Illuminating origins of impact energy dissipation in mechanical metamaterials," *Advanced Engineering Materials*, vol. 20, no. 5, p. 1 700 828, 2018.

[79] B. Florijn, C. Coulais, and M. van Hecke, "Programmable mechanical metamaterials," *Physical review letters*, vol. 113, no. 17, p. 175 503, 2014.

[80] K. Y. Lee, J. Chun, J.-H. Lee, *et al.*, "Hydrophobic sponge structure-based triboelectric nanogenerator," *Advanced materials*, vol. 26, no. 29, pp. 5037–5042, 2014.

[81] S. L. Zhang, Y.-C. Lai, X. He, R. Liu, Y. Zi, and Z. L. Wang, "Auxetic foam-based contact-mode triboelectric nanogenerator with highly sensitive self-powered strain sensing capabilities to monitor human body movement," *Advanced functional materials*, vol. 27, no. 25, p. 1 606 695, 2017.

[82] S. Niu and Z. L. Wang, "Theoretical systems of triboelectric nanogenerators," *Nano Energy*, vol. 14, pp. 161–192, 2015.

[83] C. G. Camara, J. V. Escobar, J. R. Hird, and S. J. Putterman, "Correlation between nanosecond x-ray flashes and stick-slip friction in peeling tape," *nature*, vol. 455, no. 7216, pp. 1089–1092, 2008.

[84] J. Hird, C. Camara, and S. Putterman, "A triboelectric x-ray source," *Applied Physics Letters*, vol. 98, no. 13, p. 133 501, 2011.

A. APPENDICES

A.1 Inductive Measurement of Dielectric Surface Charge Accumulation

A solenoid-based test apparatus designed in the early stage [31] of the present work is demonstrated in Figure A.1. The charge accumulation on dielectric surfaces are measured using the envelope of the charge flow between planar electrodes on their back which shows indirectly the increment in dielectric surface charge density each time the surfaces are separated to a fixed maximum gap distance.

A.2 Observations of Polymer Degradation in SEM

The damage process for multiple polymer sample surfaces under SEM examination are depicted in Figure A.2. Degradation patterns of original and carbon-coated PTFE surfaces indicate similarities to the surface damage after breakdown discharge, while that of Au-Pd-coated PTFE excludes the possibility that the observed post-discharge surface alternations are due to the SEM. Stability of PDMS samples under SEM explains why alternations are not observed on their surfaces which undergo similar high-energy particle strikes during breakdown discharge.

A.3 Subharmonic Fractal Bifurcations of Periodic Orbits of a Conservative Vibro-Impact Oscillator

The subharmonic fractals corresponding to cascades of period multiplying bifurcations in the periodic orbits of the conservative vibro-impact oscillator studied in Section 4.2.2 are shown in Figure A.3.

A.4 Implementation of a Vibro-Impact Triboelectric Energy Harvester

A prototype test apparatus for verifying models of triboelectric energy harvesters is shown in Figure A.4 which allows the variation of multiple physical parameters considered in Section 4.4.

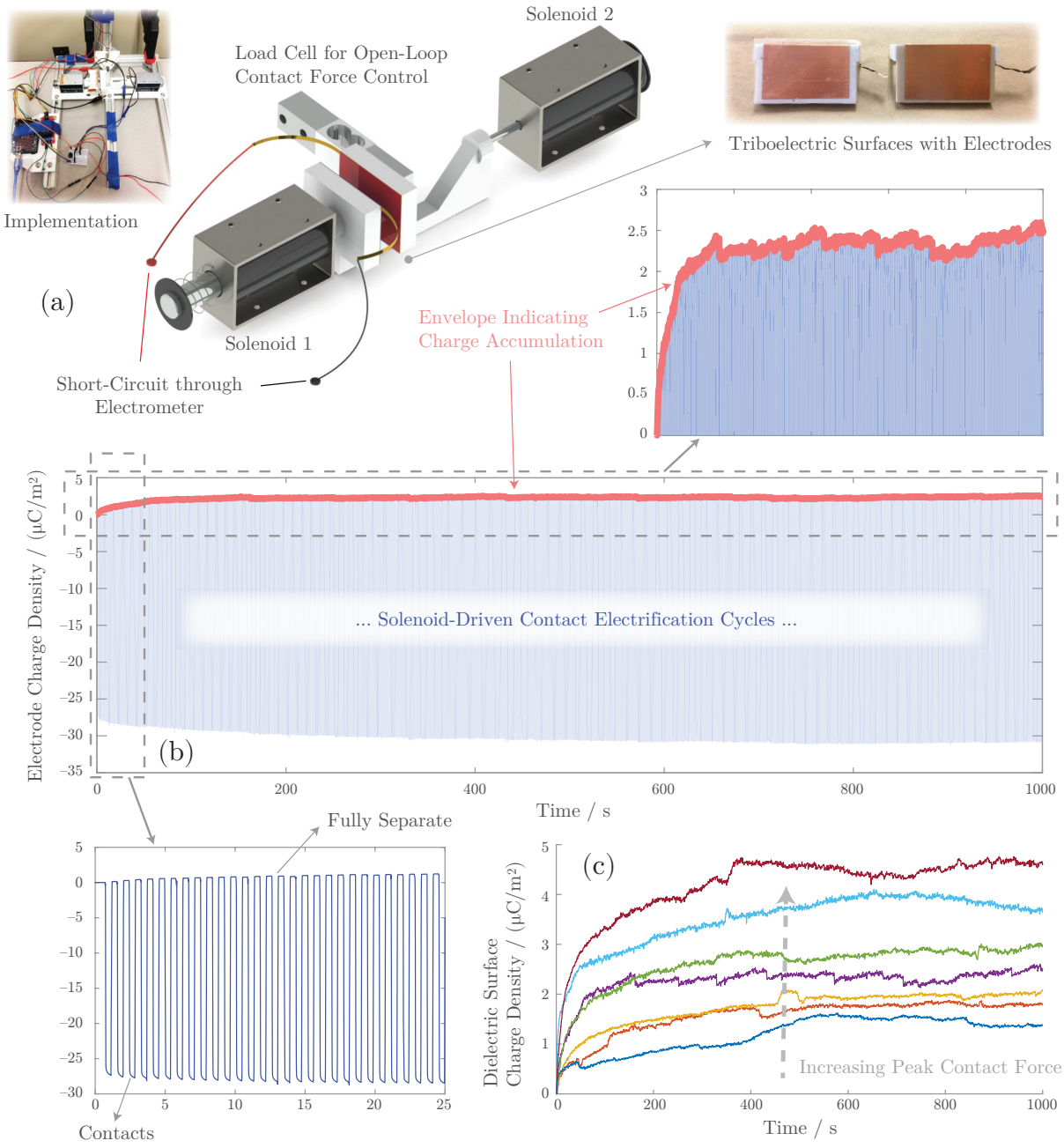

Figure A.1. Indirect measurement of dielectric surface charge accumulation in contact electrification cycles: a) The solenoid-based test apparatus. b) Time histories of charge flow in electrodes. c) Derived dielectric surface charge accumulation under various peak contact forces.

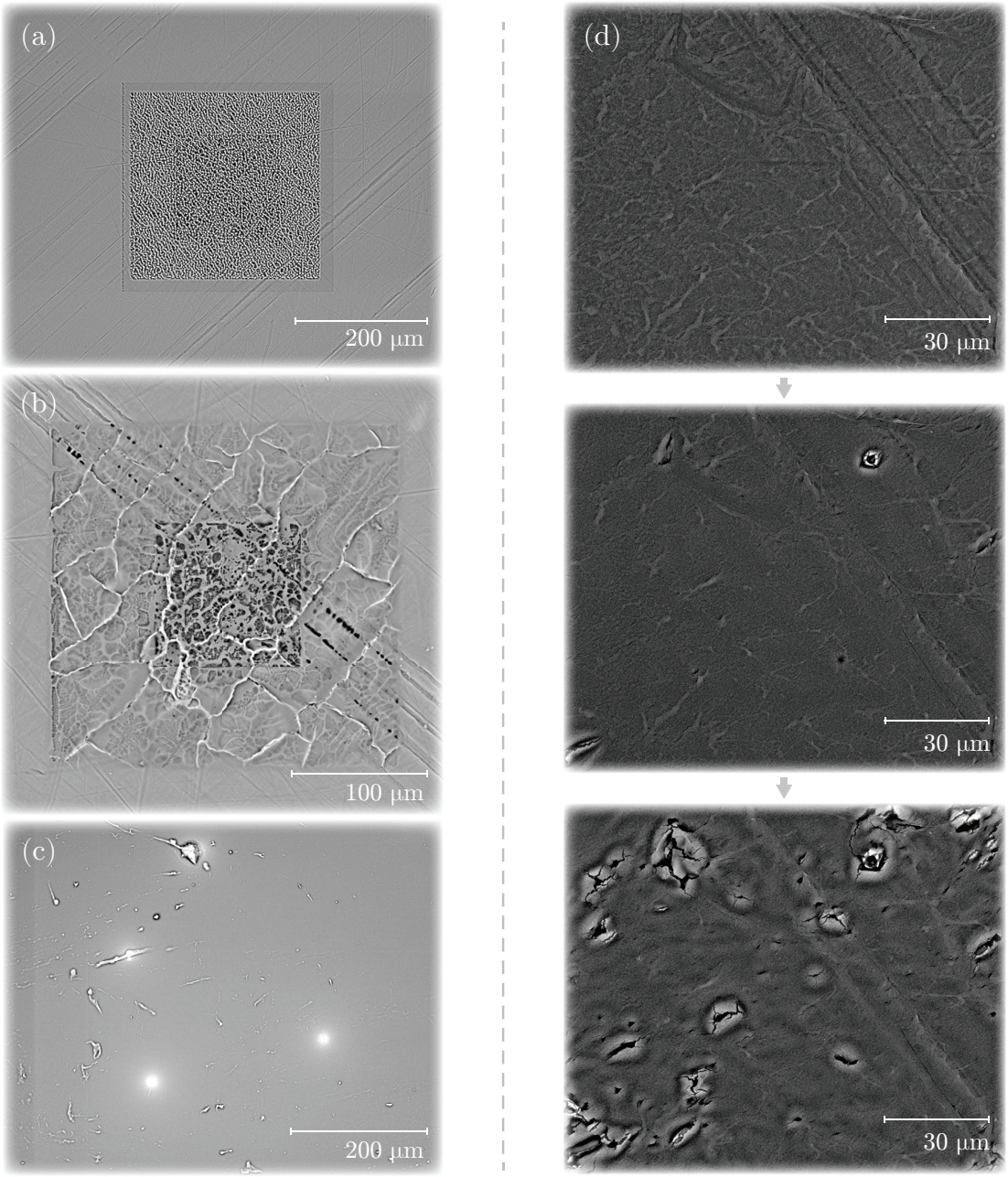

Figure A.2. Polymer surface degradation under SEM: a) Uncoated PTFE. b) Carbon-coated PTFE. c) PDMS with charged spots under high-intensity electron beams after an EDS examination. d) Progressive damage of Au-Pd-coated PTFE.

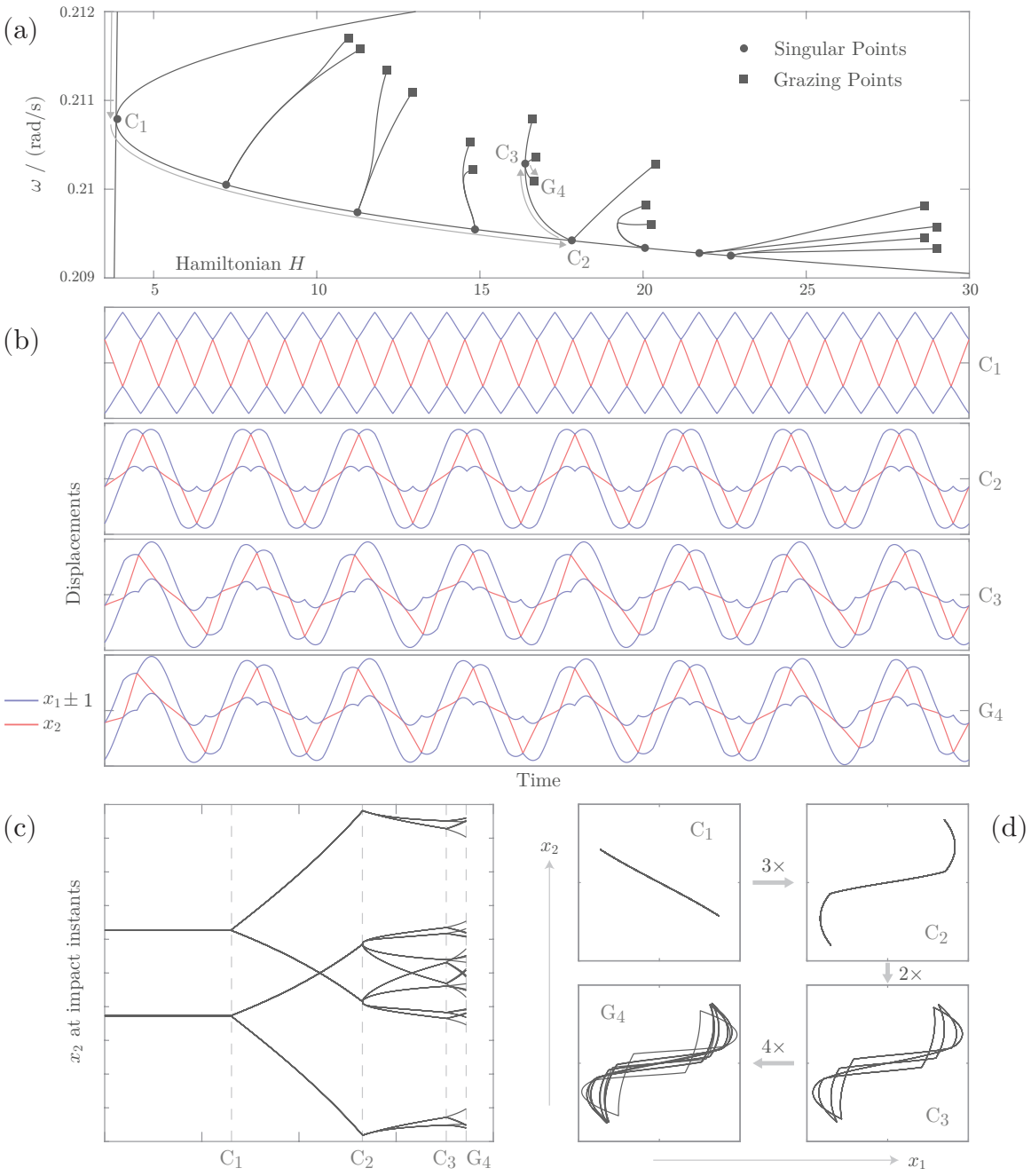

Figure A.3. Subharmonic fractal bifurcations of periodic orbits of a 2-degree-of-freedom vibro-impact oscillator: a) Frequency-energy plot. b) Time histories of selected solution points. c) Bifurcation diagram and d) phase portraits showing the cascade of period multiplying along a selected connection of branches.

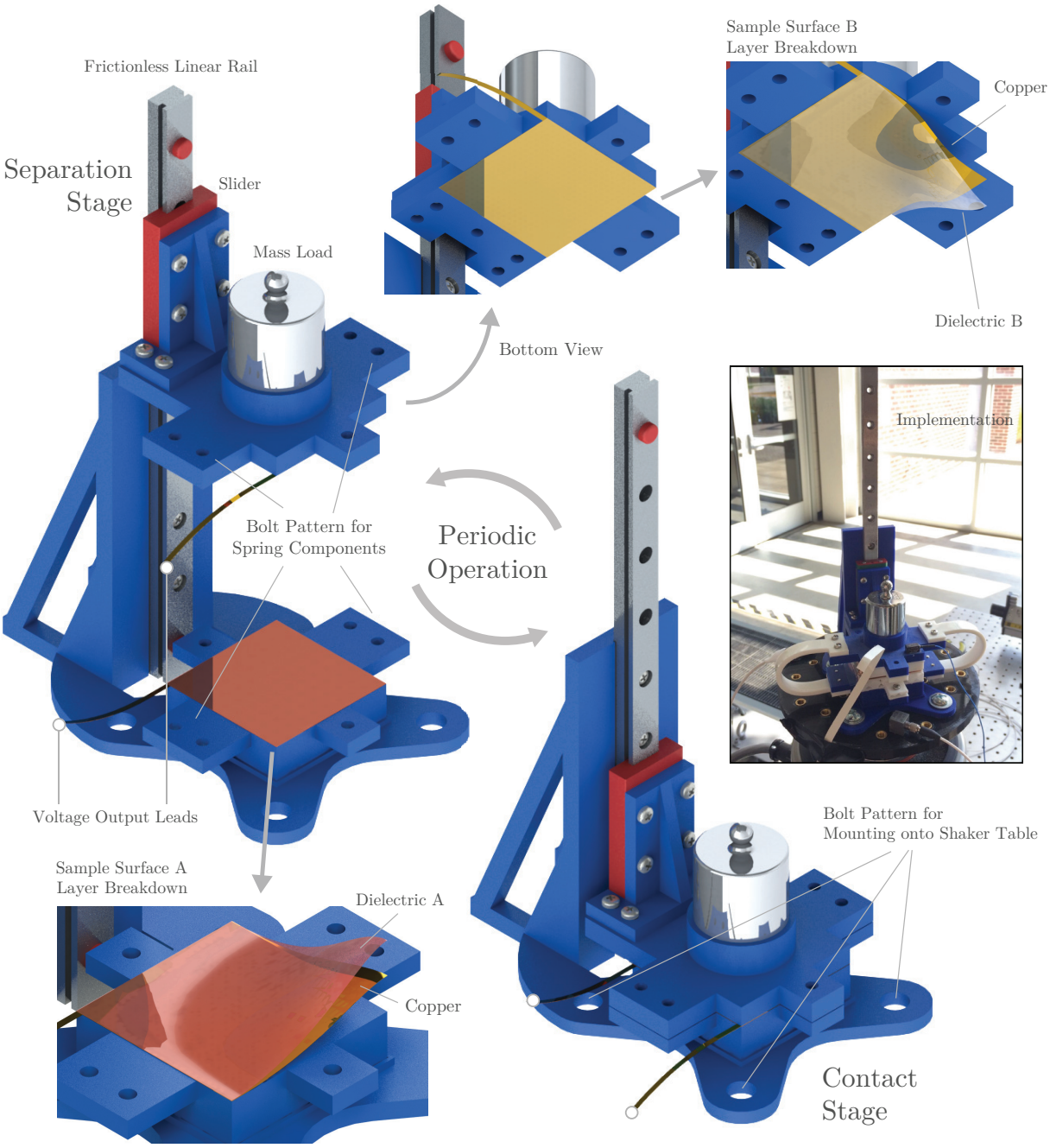

Figure A.4. Prototype implementation of a vibro-impact triboelectric energy harvester.

VITA

Hongcheng Tao taoh@purdue.edu

Education

2017-	Ph.D., Mechanical Engineering	Purdue University
2016-2017	M.S.M.E., Mechanical Engineering	Purdue University
2012-2016	B.Sc., Mechanical Engineering	Shanghai Jiao Tong University

Publications

[1] Hongcheng Tao and James Gibert. Multifunctional mechanical metamaterials with embedded triboelectric nanogenerators. *Advanced Functional Materials*, 30(23):2001720, 2020.

[2] Hongcheng Tao and James Gibert. Periodic orbits of a conservative 2-dof vibro-impact system by piecewise continuation: bifurcations and fractals. *Nonlinear Dynamics*, 95(4):2963-2993, 2019.

[3] Francesco Danzi, Hongcheng Tao, and James Gibert. The role of topology on the response of a v-shaped resonator. *Nonlinear Dynamics*, 101(4):2027-2053, 2020.

[4] Christian E Silva, Amin Maghareh, Hongcheng Tao, Shirley J Dyke, and James Gibert. Evaluation of energy and power flow in a nonlinear energy sink attached to a linear primary oscillator. *Journal of Vibration and Acoustics*, 141(6), 2019.

[5] Hongcheng Tao, Gregory Batt, and James Gibert. Modeling contact electrification in triboelectric impact oscillators as energy harvesters. In *Sensors and Smart Structures Technologies for Civil, Mechanical, and Aerospace Systems 2019*, volume 10970, page 109700U. International Society for Optics and Photonics, 2019.

[6] Hongcheng Tao, Francesco Danzi, Christian E Silva, and James Gibert. Heterogeneous Digital Stiffness Programming. *Extreme Mechanics Letters*. (under review)